CRANFIELD UNIVERSITY

Martin McCarthy

CONTRA-ROTATING OPEN ROTOR REVERSE THRUST AERODYNAMICS

SCHOOL OF ENGINEERING

MSc by Research
Academic Year: 2010 - 2011

Supervisor: Dr D.G.MacManus
June 2011

CRANFIELD UNIVERSITY

SCHOOL OF ENGINEERING

MSc by Research

Academic Year 2010 - 2011

MARTIN MCCARTHY

CONTRA-ROTATING OPEN ROTOR REVERSE THRUST AERODYNAMICS

Supervisor: Dr D.G.MacManus

June 2011

ABSTRACT

Reverse thrust operations of a model scale Contra-Rotating Open Rotor design were numerically modelled to produce individual rotor thrust and torque results comparable to experimental measurements. The aims of this research were to develop an understanding of the performance and aerodynamics of open rotors during thrust reversal operations and to establish whether numerical modelling with a CFD code can be used as a prediction tool given the highly complex flowfield.

A methodology was developed from single rotor simulations initially before building a 3D'frozen rotor' steady-state approach to model contra-rotating blade rows in reverse thrust settings. Two different blade pitch combinations were investigated ($\beta_{1,2}$ =+30˚,-10˚ and $\beta_{1,2}$ =-10˚,-20˚). Thrust and torque results compared well to the experimental data and the effects of varying operating parameters, such as rpm and Mach number, were reproduced and in good agreement with the observed experimental behaviour. The main flow feature seen in all the reverse thrust cases modelled, both single rotor and CROR, is a large area of recirculation immediately downstream of the negative pitch rotor(s).This is a result of a large relative pressure drop region generated by the suction surfaces of the negative pitch blades.

An initial 3D unsteady sliding-mesh calculation was performed for one CROR reverse thrust case. The thrust and torque values were in poor agreement with experimental values and the disadvantages relating to time costs and required computational resources for this technique were illustrated. However, the results did yield a nominal unsteady variation of thrust and torque due to rotor phase position.

Overall the work shows that it may be possible to develop a CROR reverse thrust prediction tool of beneficial quality using CFD models. The research also shows that the frozen rotor approach can be adopted without undermining the fidelity of the results.

Keywords:

CFD, propfan, negative pitch, dual propeller, counter-rotating

ACKNOWLEDGEMENTS

I would like to thank Dr David MacManus for his invaluable guidance throughout this rewarding project. He is one of the best educators I have had and his generosity with his time and advice has been greatly appreciated. Although I never expected that my command of the English language would be honed by a Galway man.

I wish to thank Rolls Royce for providing experimental data on the topic of this research.

Final thanks go to Gill for her love and encouragement as well as my family for their never-ending support, and to all my friends both inside and outside of the Cranfield bubble.

TABLE OF CONTENTS

ABSTRACT iii
ACKNOWLEDGEMENTS iv
LIST OF FIGURES vii
LIST OF TABLES ix
NOMENCLATURE x
GREEK SYMBOLS xi
ACRONYMS xi
1 Introduction 1
1.1 Project motivation 2
1.2 Project description 3
1.3 Aim and objectives 4
2 Literature Review 5
2.1 Propeller theory 5
2.2 Effect of blade angle on propeller performance 8
2.3 Propeller performance prediction 11
2.4 Contra-rotating propellers 15
2.5 Advanced propeller backround 20
2.5.1 Allison 501-M78 22
2.5.2 GE-36 UDF 23
2.5.3 PW-Allison 578DX 24
2.5.4 Ivchenko Progress D-27 25
2.5.5 NK-93 26
2.6 Propeller reverse thrust 27
3 CFD Methodology 33
3.1 Investigative approach 33
3.2 Grid strategy 35
3.3 Single rotor simulation 36
3.3.1 Domain & grid generation 39
3.3.2 Solver settings & turbulence model 42
3.3.3 Boundary & zone conditions 43
3.3.4 Iterative convergence 44
3.3.5 Grid convergence 45
3.4 Contra-rotation modelling: ‘Frozen Rotor’ approach 46
3.4.1 Domain & grid generation 47
3.4.2 Solver settings & turbulence model 48
3.4.3 Boundary & zone conditions 49
3.4.4 Iterative convergence 50
3.4.5 Grid convergence 50
4 Post-processing Methodology 52
4.1 Rotor performance 52
4.2 Blade distribution of thrust and torque 52
4.3 CFD contours and streamlines 53
5 Results 55
5.1 Single rotor CFD results 55
5.1.1 Performance analysis 55

5.1.2 Flowfield assessment 60
5.1.3 Summary of findings 62
5.2 CROR frozen rotor CFD and experimental results 63
5.2.1 Initial analysis of $\beta_{1,2}$ = +30˚, -10˚ 63
5.2.2 Rotor interaction for $\beta_{1,2}$ = +30˚, -10˚ 69
5.2.3 Mach number variation for β1,2 = +30˚, -10˚ 71
5.2.4 Front rotor rpm variation for $\beta_{1,2}$ = +30˚, -10˚ 76
5.2.5 Aft rotor rpm variation for $\beta_{1,2}$ = +30˚, -10˚ 82
5.2.6 Summary of findings (CROR at $\beta_{1,2}$ =+30˚,-10˚) 87
5.2.7 Initial analysis for $\beta_{1,2}$ = -10˚, -20˚ 88
5.2.8 Mach number variation for $\beta_{1,2}$ = -10˚, -20˚ 91
5.2.9 Rotor interaction for $\beta_{1,2}$ = -10˚, -20˚ 95
5.2.10 Aft rpm variation for $\beta_{1,2}$ = -10˚, -20˚ 97
5.2.11 Summary of findings (CROR at $\beta_{1,2}$ =-10˚,-20˚) 103
5.3 CROR unsteady full rotor CFD results 104
5.3.1 Performance analysis 104
5.3.2 Flowfield assessment 107
5.3.3 Unsteady interaction effects due to rotor phase position 108
5.3.4 Summary of findings 110
6 Conclusions and future work 111
6.1 CFD prediction of rotor performance 111
6.2 Origin and impact of flowfield recirculation 111
6.3 Negative torque and overspeed 113
6.4 CFD unsteady sliding-mesh calculation 114
6.5 Future work 114
7 References 116
Appendix A 119

LIST OF FIGURES

Figure 1-1 Contra-Rotating Open Rotor concept [1]. 1
Figure 1-2 Price History of Crude Oil and Jet Fuel [3]. 3
Figure 2-1 Geometric and Effective Pitch [5]. 5
Figure 2-2 Airfoil element from a propeller blade [6]. 7
Figure 2-3 Effect of pitch on performance [7]. 9
Figure 2-4 Efficiency curves for a small and large pitch [7]. 10
Figure 2-5 Efficiency curves for increasing pitch angle of a constant rpm propeller [7]. 10
Figure 2-6 Vectors and forces for a positive pitch blade element [6]. 12
Figure 2-7 Vectors and forces for a negative pitch blade element [6]. 13
Figure 2-8 Vectors and forces for a negative pitch blade element with large wind velocity. 14
Figure 2-9 Velocity diagram of 2D elements from contra-rotating propellers 15
Figure 2-10 Effect of contra-rotation on thrust coefficient for 4-bladed propellers at constant power [8]. 16
Figure 2-11 Effect of contra-rotation on efficiency for 4-bladed propellers at constant power [8]. 17
Figure 2-12 Douglas A2D Skyshark [9]. 18
Figure 2-13 Avro Shackleton with Rolls Royce Griffon engines on display in S.A.A.F Museum [10]. 18
Figure 2-14 Tupolev Tu-95 Strategic Bomber with NK-12 engines [12]. 19
Figure 2-15 Allison 501-M78 Advanced Turboprop on display at NASA PSL [19]. 23
Figure 2-16 GE-36 UDF mounted on MD-80. 24
Figure 2-17 PW-Allison 578DX contra-rotating propfan 25
Figure 2-18 Ivchenko Progress D-27 contra-rotating propfan on Antonov AN-70 [25]. 26
Figure 2-19 NK-93 Ducted Contra-rotating Propfan [29]. 27
Figure 2-20 Effect of Mach no. on reverse thrust performance of F7/A7 8/8 propeller [35]. 29
Figure 2-21 Velocity magnitude Cases 1 & 2 given in (a) and (b) respectively [36]. .. 30
Figure 2-22 Comparison of averaged axial, radial and tangential velocities for the 2 cases [36]. 32
Figure 3-1 Progression of grid construction and test matrices used for single rotor simulations. 38
Figure 3-2 Multi-block domain geometry of single front rotor simulation. 40
Figure 3-3 Meridional diagram of reduction in domain extent after initial single rotor simulations. 41
Figure 3-4 Multi-block layout for structured C-type mesh wrap around blade. 42
Figure 3-5 Single rotor simulation domain boundary conditions. 43
Figure 3-6 Residual, force and moment convergence for single rotor grid. 45
Figure 3-7 Progression of grid construction and test matrices used for 'Frozen Rotor' contra-rotation simulations. 47
Figure 3-8 Meridional diagram of domain extent for contra-rotation modelling. 48
Figure 3-9 Contra-rotation simulation domain boundary conditions. 49
Figure 3-10 Residual convergence for contra-rotation grid. 50

Figure 4-1 Example of 3D flow visualisation from CFD results. 53
Figure 4-2 Examples of meridional and circumferential contours from CFD results. . 54
Figure 5-1 Single front rotor CFD T & Q values for β_1 = +30˚. 55
Figure 5-2 Force Diagrams for positive and negative angle of attack. 57
Figure 5-3 Single front rotor CFD T & Q values for β_1 = -10˚. 58
Figure 5-4 Force Diagram for negative pitch angle. 58
Figure 5-5 Single aft rotor CFD T & Q values for β_2 = -10˚ and β_2 = -20˚. 59
Figure 5-6 Force Diagram showing effect of increased negative pitch angle. 60
Figure 5-7 Singe front rotor contours and streamtraces for β= -10˚ and M = 0.05. ... 61
Figure 5-8 Singe front rotor contours and streamtraces for β= -10˚ and M = 0.2. 61
Figure 5-9 Experimental and CFD rotor thrust values for $\beta_{1,2}$ = +30˚, -10˚. 64
Figure 5-10 Experimental and CFD rotor torque values for $\beta_{1,2}$ = +30˚, -10˚. 65
Figure 5-11 CROR contours and streamtraces for $\beta_{1,2}$ = +30˚, -10˚, rpm = N1:N2 and M = 0.1. 67
Figure 5-12 Single rotor and contra-rotating T and Q results for $\beta_{1,2}$ = +30˚, -10˚ and rpm N1:N2. 69
Figure 5-13 C_P contours of CROR at $\beta_{1,2}$ = +30˚, -10˚ and rpm N1:N2. 70
Figure 5-14 C_P contours of SR aft rotor at β_2 = -10˚ and rpm N2. 71
Figure 5-15 Normalised axial velocity contours for CROR at $\beta_{1,2}$ =+30˚,-10˚ and rpm= N1:N2. 73
Figure 5-16 C_p contours for CROR at $\beta_{1,2}$ =+30˚,-10˚ and rpm= N1:N2. 74
Figure 5-17 Average blade distribution from pressure forces for CROR at $\beta_{1,2}$ =+30˚,-10˚, rpm = N1:N2. 75
Figure 5-18 Experimental rotor T and Q values for $\beta_{1,2}$ = +30˚, -10˚ with constant aft rotor rpm N2. 76
Figure 5-19 CROR contours and streamtraces for $\beta_{1,2}$ = +30˚, -10˚, rpm = 2(N1):N2 and M = 0.1. 78
Figure 5-20 Normalised axial velocity contours for CROR at $\beta_{1,2}$ =+30˚,-10˚, rpm = 2(N1):N2 79
Figure 5-21 C_p contours for CROR at $\beta_{1,2}$ =+30˚,-10˚, rpm = 2(N1):N2. 81
Figure 5-22 Average blade distribution from pressure forces for CROR at $\beta_{1,2}$ =+30˚,-10˚, rpm = 2(N1):N2. 82
Figure 5-23 Experimental rotor T and Q values for $\beta_{1,2}$ = +30˚, -10˚ with constant front rotor rpm N1. 83
Figure 5-24 Normalised axial velocity contours for CROR at $\beta_{1,2}$ =+30˚,-10˚, M=0.1. 84
Figure 5-25 C_p contours for CROR at $\beta_{1,2}$ =+30˚,-10˚ and M = 0.1 85
Figure 5-26 Average blade distribution from pressure forces for CROR at $\beta_{1,2}$ =+30˚,-10˚, rpm = N1:N2. 86
Figure 5-27 Average blade distribution from pressure forces for CROR at $\beta_{1,2}$ =+30˚,-10˚, rpm = N1:2(N2). 86
Figure 5-28 Experimental and CFD rotor thrust values for $\beta_{1,2}$ = -10˚, -20˚. 88
Figure 5-29 Experimental and CFD rotor torque values for $\beta_{1,2}$ = -10˚, -20˚. 89
Figure 5-30 CROR contours and streamtraces for $\beta_{1,2}$ = -10˚, -20˚, rpm = N1:N2 and M = 0.05. 90
Figure 5-31 Normalised axial velocity contours for CROR at $\beta_{1,2}$ =-10˚,-20˚ and rpm= N1:N2. 93
Figure 5-32 C_p contours for CROR at $\beta_{1,2}$ =-10˚,-20˚ and rpm= N1:N2. 94

Figure 5-33 Average blade distribution from pressure forces for CROR at $\beta_{1,2}$ =-10˚,-20˚, rpm = N1:N2. 95
Figure 5-34 Single rotor and contra-rotating T and Q results for $\beta_{1,2}$ = -10˚, -20˚ and rpm N1:N2. 96
Figure 5-35 Circumferential C_p contours at 70% front rotor bladespan. 96
Figure 5-36 Experimental rotor T and Q values for $\beta_{1,2}$ = -10˚, -20˚ with constant front rotor rpm N1. 98
Figure 5-37 CROR contours and streamlines for $\beta_{1,2}$ = -10˚, -20˚, rpm = N1:2(N2) and M = 0.05. 99
Figure 5-38 Normalised axial velocity contours for CROR at $\beta_{1,2}$ =-10˚,-20˚ M=0.05. 100
Figure 5-39 C_p contours for CROR at $\beta_{1,2}$ = -10˚,-20˚ M = 0.05. 101
Figure 5-40 Average blade distribution from pressure forces for CROR at $\beta_{1,2}$ =-10˚,-20˚, rpm = N1:2(N2). 102
Figure 5-41 Unsteady front and aft blade thrust variation with timestep for $\beta_{1,2}$ = -10˚, -20˚, rpm = N1:N2 and M = 0.05. 105
Figure 5-42 Unsteady front and aft blade torque variation with timestep for $\beta_{1,2}$ = -10˚, -20˚, rpm = N1:N2 and M = 0.05 106
Figure 5-43 Unsteady C_p contours for $\beta_{1,2}$ = -10˚, -20˚, rpm = N1:N2 and M = 0.05. 107
Figure 5-44 Unsteady meridional normalised axial velocity contours for $\beta_{1,2}$ = -10˚, -20˚, rpm = N1:N2 and M = 0.05. 108
Figure 5-45 Circumferential contours of Cp at 70% front rotor bladespan taken at 5 varying phase positions. 109

LIST OF TABLES

Table 1 Under-relaxation values for single rotor calculations. 45
Table 6-1 Downstream extent of reverse flow measured by Vaxial=0m/s on hub surface. 112

NOMENCLATURE

c	Chord length
C_l	Sectional lift coefficient
C_L	Lift coefficient
C_d	Sectional drag coefficient
C_D	Drag coefficient
C_p	Pressure coefficient
C_P	Power coefficient
C_T	Thrust coefficient
C_Q	Torque coefficient
d	Propeller diameter
D	Propeller diameter
D	Drag
J	Advance ratio
L	Lift
L_1	Front rotor blade length
L_2	Aft rotor blade length
M	Mach number
N_1	Front rotor rpm
N_2	Aft rotor rpm
P	Geometric pitch
P_e	Effective pitch
P	Power
Q	Torque
Q_1	Front rotor torque
Q_2	Aft rotor torque
r	radius
Re	Reynolds number
T	Thrust
T_1	Front rotor thrust
T_2	Aft rotor thrust
U_1	Front blade row speed
U_2	Aft blade row speed

V	Wind velocity
V_R	Relative velocity
V_∞	Freestream velocity
V_i	Induced velocity
V_1	Wind velocity at station 1
V_2	Wind velocity at station 2
V_3	Wind velocity at station 3
V_4	Wind velocity at station 4
x_s	Axial rotor spacing

GREEK SYMBOLS

α	Angle of attack
β	Pitch angle
β_1	Front rotor pitch angle
β_2	Aft rotor pitch angle
$\beta_{0.7R}$	Overall blade pitch angle (taken at 70% span)
Ω	angular velocity
η	Propeller efficiency
ρ	Density
θ	Induced velocity angle
φ	Helix angle
μ	Kinematic viscosity

ACRONYMS

ACARE	Advisory council for aeronautics research in Europe
CROR	Contra-rotating open rotor
DREAM	Validation of radical engine architecture system
FOD	Foreign object damage
IPCC	Intergovernmental panel on climate change
PIV	Particle image velocimetry
PTA	Propfan test assessment
RANS	Reynolds averaged Navier Stokes equations

SR	Single rotor
UDF	Unducted fan
UHB	Ultra-high bypass

1 Introduction

In recent years there has been an increased focus on advancing current technologies of aviation propulsion as well as introducing viable alternatives. This focus has concentrated particularly on an engine layout aimed at the commercial aviation sector to rival the dominant turbofan range. The Contra-Rotating Open Rotor (CROR) engine originated from research conducted 3 decades ago, with a current concept design shown in *Figure 1-1*. This type of engine is essentially the core of a turbofan with two rows of contra-rotating fan blades placed on the outside of the nacelle. It aims to combine the advantages of turbofan and turboprop engines by providing large thrust capabilities and higher cruise flight speeds with increased fuel efficiency and reduced weight respectively. Recent environmental and economic factors, described in the following section, have led the industry to return to the open rotor engine and address certain technical issues that contributed to halting its development and eventual introduction to commercial operation.

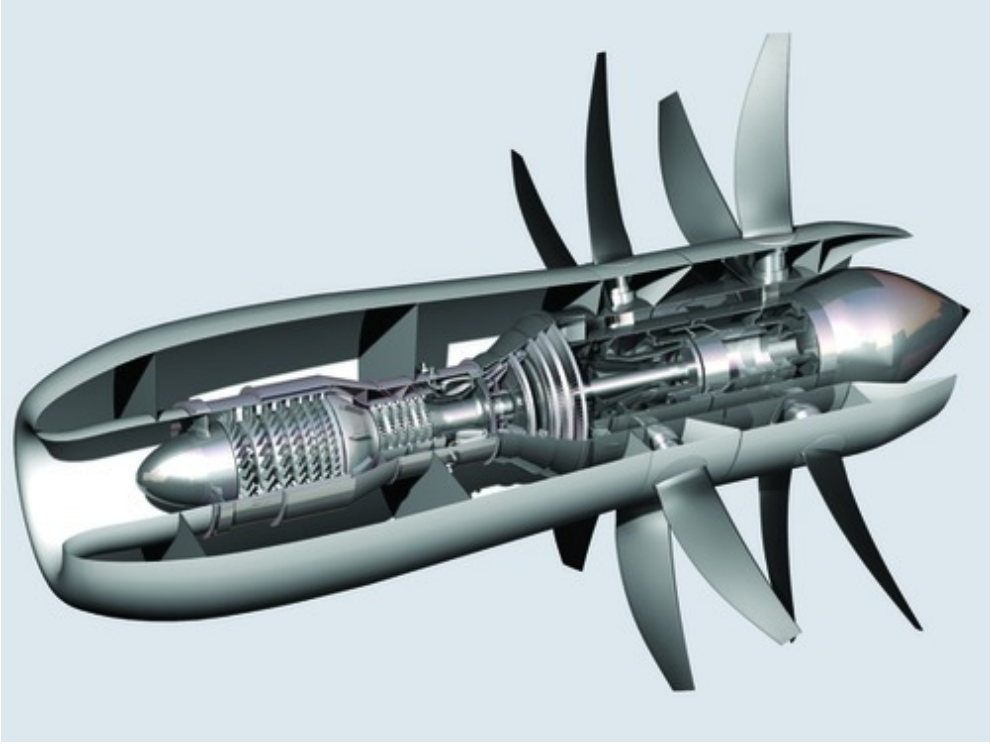

Figure 1-1 Contra-Rotating Open Rotor concept [1].

1.1 Project motivation

Aircraft engines emit carbon dioxide in the take-off and climb phase of flight and nitrogen oxides at high altitudes during the cruise phase of flight. Climate change investigations have highlighted these particular emissions relating to the aviation sector as being a significant contributor of the pollutant gases causing global warming [2]. The Intergovernmental Panel on Climate Change (IPCC) has estimated that aviation is responsible for roughly 3.5% of anthropogenic climate change. The IPCC central case estimate is that aviation's contribution could grow to 5% of the total contribution by 2050 if action is not taken to tackle these emissions. In response to increased focus on climate change in 2000, the Advisory Council for Aeronautics Research in Europe (ACARE), in agreement with engine manufacturers, published goals for the aviation industry to meet by 2020.

- To reduce fuel consumption and CO_2 emissions by 50% (20% for the engine alone).
- To reduce perceived external noise by 50%.
- To reduce NO_x emissions by 80%.

These ACARE goals have prioritized the environmental reason and further increased the motivation of engine manufacturers for advancing technologies.

The commercial motivation has been heightened in recent years due to the global economic crisis and the resulting jump in the price of fuel, which hit an all-time high in 2008. Prices reached a record $140/barrel of crude oil (Figure 1-2) and the knock-on effect for airlines already operating a low-cost business model has been enormous. Even though the cost of fuel has oscillated greatly since that record high, the trend has been widely accepted to be upwards in the coming years.

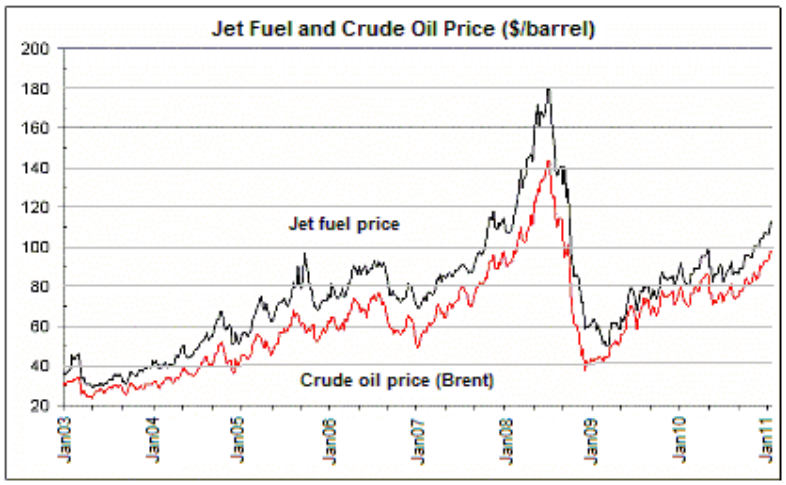

Figure 1-2 Price History of Crude Oil and Jet Fuel [3].

1.2 Project description

The research conducted in this thesis is part of a large international project called DREAM (vali**D**ation of **R**adical **E**ngine **A**rchitecture syste**M**) which is aimed at directly addressing the ACARE goals. The project is conducted by a consortium of 44 partners, from Europe and Russia, which is led by Rolls Royce and includes Cranfield University. One of the objectives of DREAM is the design, testing and performance analysis of Contra-Rotating Open Rotor engines for the commercial aviation sector.

A common requirement of commercial transport aircraft is the ability to produce reverse thrust as a braking effect to reduce the landing distance. This requirement for extra braking effect was born out of the historical need of long runways for large aircraft, although today it is mainly to reduce aircraft turn-around time and airport charges. Since DREAM focuses on CROR engine designs as an economically and environmentally viable alternative to turbofans, the production of reverse thrust is required in the engine designs capabilities. This is achieved by changing the blade pitch setting (β) of one or both rotors from a positive to negative value.

While there are theoretical models available for the positive thrust prediction of open rotors [4], currently there exists no theoretical model for reverse thrust prediction.

Numerical modelling has been extensively used in aerodynamic and aeroacoustic investigations of positive-thrust open-rotor performance however there is no evidence in the public domain that it can be used for single or contra-rotation reverse thrust investigations. Historically, for conventional propellers, empirical testing has been common practice to attain reverse thrust performance and identify potential conditions that lead to overspeed of the engine, from minimal or negative blade torque. Those same investigative objectives exist today for reverse thrust testing of contra-rotating open rotors, however their importance and relevance to future engine designs is increased due to the added aerodynamic complexity of flow through contra-rotating blades. Since there are no performance prediction methods and no understanding of the associated flowfield, this complicated operating condition for open rotor engines is the subject of present research undertaken at Cranfield University.

Reverse thrust operations were experimentally investigated on a model scale CROR design where thrust (T) and torque (Q) measurements for individual rotors were obtained. These T and Q results, along with the corresponding test conditions, have been provided to Cranfield University for the purpose of research.

1.3 Aim and objectives

The aims of this research are to develop an understanding of the performance and aerodynamics of contra-rotating open rotors during thrust reversal operations and establish whether numerical modelling with a CFD code can be used as a prediction tool.

To achieve these aims, the following objectives were outlined.

- Interpret experimental data from initial reverse thrust testing.
- Investigate relationships between various rotor operating parameters and rotor performance characteristics.
- Investigate flow behaviour and phenomena associated with rotors operating in reverse thrust.

2 Literature Review

The following chapter aims to provide the reader with some basic definitions, terminology and performance concepts of propeller theory. A base of knowledge in the normal operation of propellers must be established before the contra-rotation and reverse thrust are investigated. To this end, 2D representations of the flow are illustrated in the following sections to show the effects of certain parameters on rotor performance terms. The effect of contra-rotation is also explained and a brief history of its use is given. This chapter also contains a summary of the extensive research from the 70's and 80's into advanced propellers and contra-rotating open rotors that led to the construction of demonstrator engines. Limited research of propeller reverse thrust is summarised along with a more relevant and recent flowfield investigation.

2.1 Propeller theory

If we consider a propeller (of diameter *d*) turning one full revolution through a medium, then *Figure* ***2-1*** shows the path of a blade tip from that propeller as it moves through a medium. It traces a helix around an imaginary cylinder. If we take this imaginary cylinder to be a rectangular piece of paper rolled up, then after the helix has been carved into it by the blade tip, the paper would look like the triangular section in *Figure* ***2-1*** if it were unrolled. The helical path is now represented by a diagonal line. This can help visualize a few common propeller terms given below.

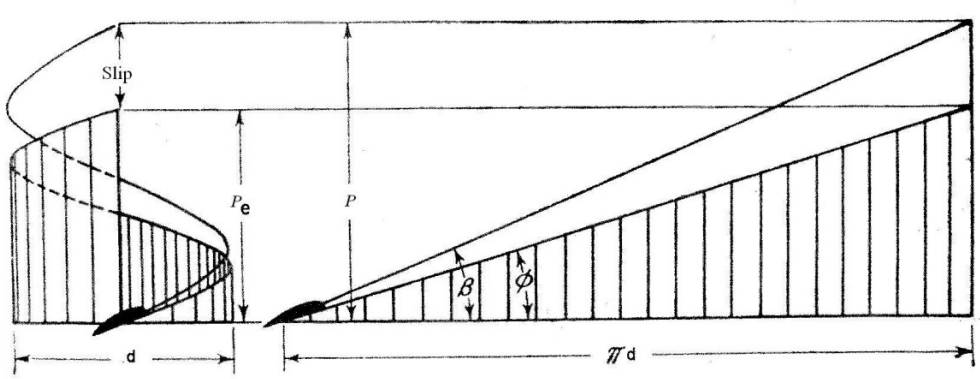

Figure 2-1 Geometric and Effective Pitch [5].

Geometric pitch (P) is the theoretical distance a propeller travels in the forward direction from one revolution. In reality the distance travelled is less due to the fact that the medium the propeller is travelling through is air and not a solid. This affect is called slip and therefore another term, effective pitch (P_e), is used to describe the actual distance travelled (see *Figure 2-1*).

For aircraft propellers each blade acts like a rotating wing and needs to be set in a certain position so as to create an angle of incidence with the incoming air. A slice taken from a blade, of thickness *dr* and chord length *c*, is illustrated in

***Figure** 2-2*. Blade angle (also known as pitch angle) is denoted by β and is shown as the angle the airfoil chord-line makes with the plane of rotation. It should be noted that β is also commonly defined using an airfoils zero-lift line. V denotes the velocity vector of the approaching air with V_R being the relative air velocity to the blade. Also shown in

***Figure** 2-2* is the helix angle (φ) which relates to the effective pitch and is the angle V_R makes with the rotational plane. The angle of attack (α) is that which V_R makes with the blade. The forces acting on the 2D blade element are depicted to illustrate how lift (L) and drag (D) resolve into thrust (T) and torque (Q) and their corresponding directions.

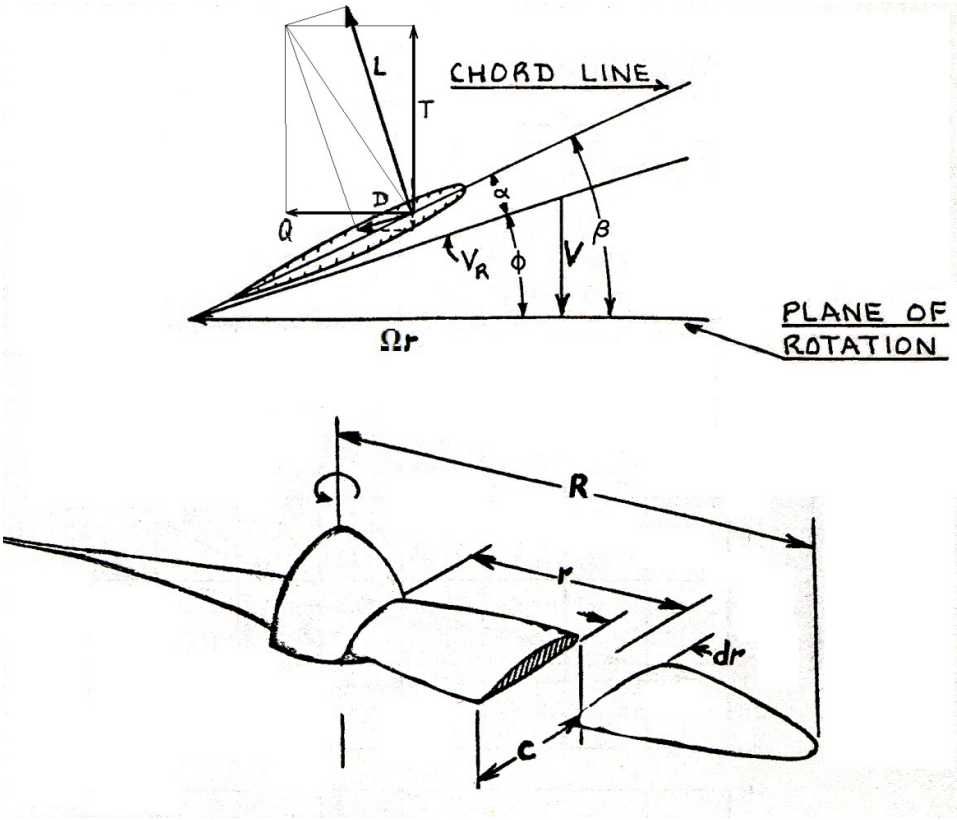

Figure 2-2 Airfoil element from a propeller blade [6].

Similar to airfoils and wings, the propeller performance can be described in non-dimensional coefficients. While an airfoil can be characterized by relationships between angle of attack, lift coefficient and drag coefficient, a propeller can be described in terms of thrust, power and torque coefficients (C_T, C_P, C_Q) which are typically plotted against advance ratio (J). The standard non-dimensional coefficients are given below [7]:

Thrust Coefficient $$C_T = \frac{T}{\rho n^2 D^4} \quad \text{.....(1)}$$

Power Coefficient $$C_P = \frac{P}{\rho n^3 D^5} \quad \text{.....(2)}$$

Torque Coefficient $$C_Q = \frac{Q}{\rho n^2 D^5} \quad \text{.....(3)}$$

Advance Ratio $$J = \frac{V}{nD} \quad \text{.....(4)}$$

where n is the rotational speed, D is the propeller diameter and P is the power used by the propeller.

Propeller Efficiency (η) can be described as the ratio of the work given out by the propeller to the work put in by the engine. The work input by the engine is the power supplied to the propeller and can be expressed as:

$$P_{in} = 2\pi nQ$$

The work output from the propeller can be expressed as:

$$P_{out} = TV$$

Efficiency $$\eta_{prop} = \frac{TV}{2\pi nQ} = \frac{1}{2\pi}\frac{C_T}{C_Q}J = \frac{C_T}{C_P}J \quad \text{.....(5)}$$

2.2 Effect of blade angle on propeller performance

Propeller blades can have a degree of twist in it which helps improve performance by keeping the local α to appropriate thrust-producing values. Due to each 2D blade element having a different β, the overall 3D blade angle ($\beta_{0.7R}$) is taken as the value of β at 70% radius of the blade [6], although it should be highlighted that other sources use the angle at 75% span [7]. *Figure 2-3* (a) and (b) shows a pair 2D blade elements of a conventional propeller, the first with a small β or fine pitch, and the second with a large β or coarse pitch.

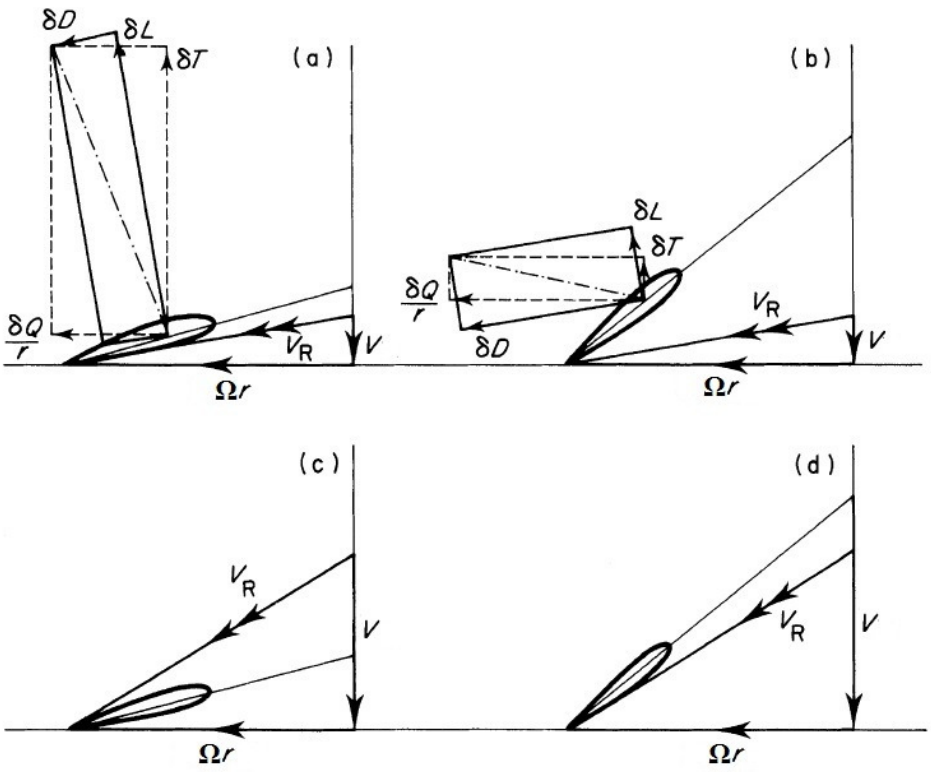

Figure 2-3 Effect of pitch on performance [7].

If the inflow velocity V is small, during take-off, the fine pitch blade sees a reasonable angle of attack from V_R which results in large thrust (*Figure 2-3* (a)). The coarse pitch blade however experiences a very large angle of attack and is stalled, resulting in little thrust (*Figure 2-3* (b)). At high flight speeds however the situation is changed dramatically. When V is large the coarse pitch blade experiences a suitable angle of attack and is working efficiently (*Figure 2-3* (d)) but the fine pitch blade is now producing negative thrust due to the resulting angle of attack becoming negative (*Figure 2-3* (c)). A propeller that has a value of β suited for low speed during take-off and climb will have poor performance at high speeds and the opposite is also true. This was one issue that limited aircraft performance in the early days of powered flight.

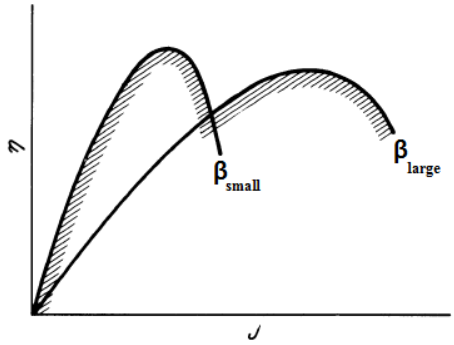

Figure 2-4 Efficiency curves for a small and large pitch [7].

An initial solution to this performance issue was the creation of a two-pitch propeller incorporating a fine and coarse pitch setting, where β small large could be changed to either value depending on the flight conditions. *Figure 2-4* shows how the η varies with increasing advance ratio for a small and large β value. The hatched area shows how the combination of two pitch settings could affect the overall performance and demonstrates the advantage over a propeller operating with just one β value.

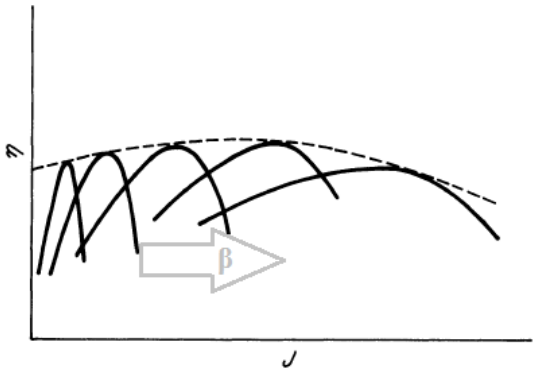

Figure 2-5 Efficiency curves for increasing pitch angle of a constant rpm propeller [7].

Subsequent advancements led to the development of a constant speed propeller in which β is capable of being set to any angle in a very large degree range. This variable pitch propeller has a mechanism in the hub that changes the pitch to keep the engine speed constant at varying flight speeds. It also enables the propeller to work close to its maximum efficiency at all times. *Figure 2-5* shows how the operating curves change

with increasing β value. The dashed line represents the envelope of all the curves and highlights the most desired area to operate the propeller for maintaining optimum efficiency over increasing J. Variable pitch has led to the incorporation of feathering for a dead or inoperable engine in aircraft, where the pitch is set to give a zero value of α, so that the propeller is prevented from turning the engine (known as wind-milling). Wind-milling is undesirable as it leads to drag. Variable pitch has also allowed aircraft to produce significant amounts of reverse thrust. This is when β is set to certain values that enable the propeller to produce thrust in the opposite direction of flight. Reverse thrust is used to reduce the aircraft landing distance as well as for manoeuvring on the ground. It is worth noting that the β value required for reverse thrust can be positive or negative as long as the resulting local angle of incidence for the blade sections (α) is negative. Reverse thrust operating condition is the topic under investigation in this research and will be focused on in an upcoming section.

2.3 Propeller performance prediction

There is a very simple theory for describing the ideal overall propeller performance called 'Momentum Theory'. It does not provide enough information for propeller design purposes since it ignores the blade planform and sectional characteristics, however it does take into account the induced velocity of the ideal propeller. A description of this theory is given in Appendix A. 'Blade-Element Theory' is a simple method of predicting propeller performance by splitting the propeller blade into an infinite number of sections and investigating the forces acting on each section. It therefore requires sectional characteristics data like local lift and drag coefficients (C_l and C_d) to be known prior to use. It does not take into account the induced velocity from thrust production. A description of this theory is given in Appendix A. Also included in Appendix A is the combined Blade Element Momentum Theory which gives propeller performance by obtaining the blade loading which includes the induced velocity. While it is simplified and ignores 3D flow effects it is still a useful tool for first order predictions of thrust, torque and efficiency. Other theories such as vortex theory combine with blade-element methods to produce much more accurate calculations of

induced effects [7] however they are all inapplicable to reverse thrust settings for the following reasons:

1) *Figure 2-6* taken from [6] shows the vector notation as in *Figure 2-2* but includes the induced velocity vector (V_i) and the angle (θ) between the old and new relative velocity vectors respectively (V_R and V_{R0}). θ is assumed to be small to aid in simplification and calculation of a new angle of incidence α_0 that V_{R0} makes with the airfoil section.

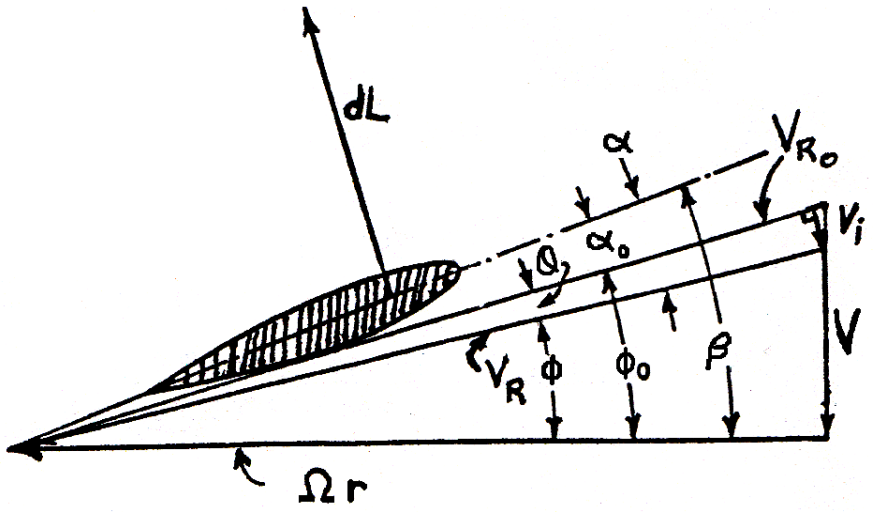

Figure 2-6 Vectors and forces for a positive pitch blade element [6].

This assumption cannot be made for reverse thrust settings since the induced velocity is anticipated to be larger given the action of the propeller is to oppose the flow through it. This is illustrated in *Figure 2-7* for an airfoil in negative pitch, again taken from [6]. It is the only diagram found in the public domain by the author that attempts to illustrate the vectors and forces acting on a reverse thrust producing airfoil. The angle θ associated with induced velocity V_i is much larger than in the positive thrust case (*Figure 2-6*) and is therefore less appropriate to be considered small for simplification during theory calculations.

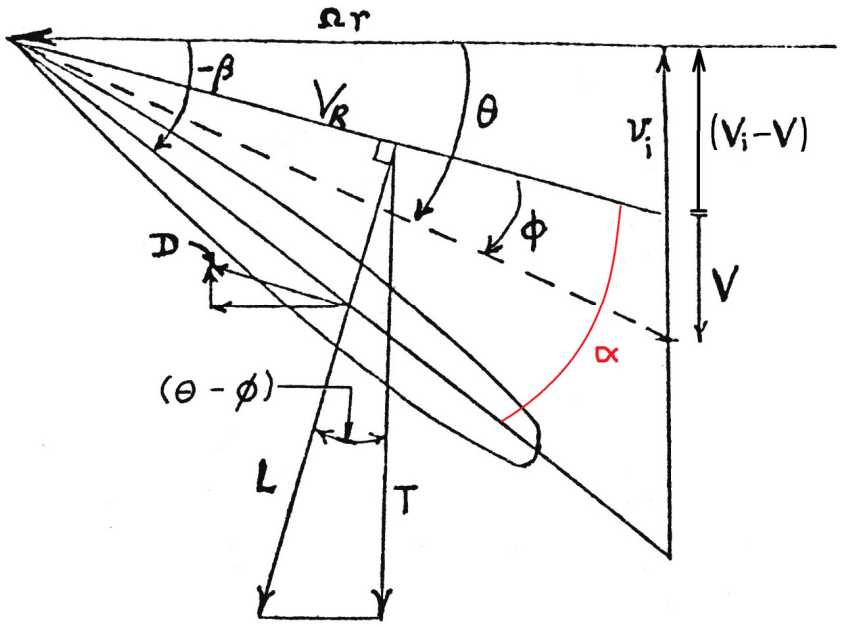

Figure 2-7 Vectors and forces for a negative pitch blade element [6].

2) To use blade-element prediction theories the sectional performance characteristics (C_l and C_d) are taken from available airfoil data, using each sectional incidence angle that has been altered to account for induced velocity. However reverse thrust settings are generally going to result in very large negative angles of incidence for the relative velocity approaching the blade element. These α values are anticipated to be beyond the negative stall point of an airfoil C_l-α curve. It is not common for airfoil characteristics to be included in available airfoil data for incidence angles significantly beyond the positive and negative stall values. Therefore sectional characteristics would be unavailable for blade-element based theories.

It is worth noting that *Figure 2-7* represents a specific scenario in reverse thrust where the induced velocity is larger in magnitude than the wind velocity. This depicts a reverse in flow direction through the propeller because the approaching wind velocity (or aircraft velocity) is very small. [6] chose to illustrate this as it results in an incidence angle that may still be within stall limits for obtaining sectional data (C_l and C_d) and proposed a method for predicting reverse thrust performance. In the authors opinion, the more common scenario to be expected during reverse thrust operation is a large wind velocity that is opposed, and reduced, by a smaller induced velocity from the blades as

the flow progresses through the propeller in the conventional direction. This is depicted in *Figure 2-8* using the same diagram style from [6] for consistency.

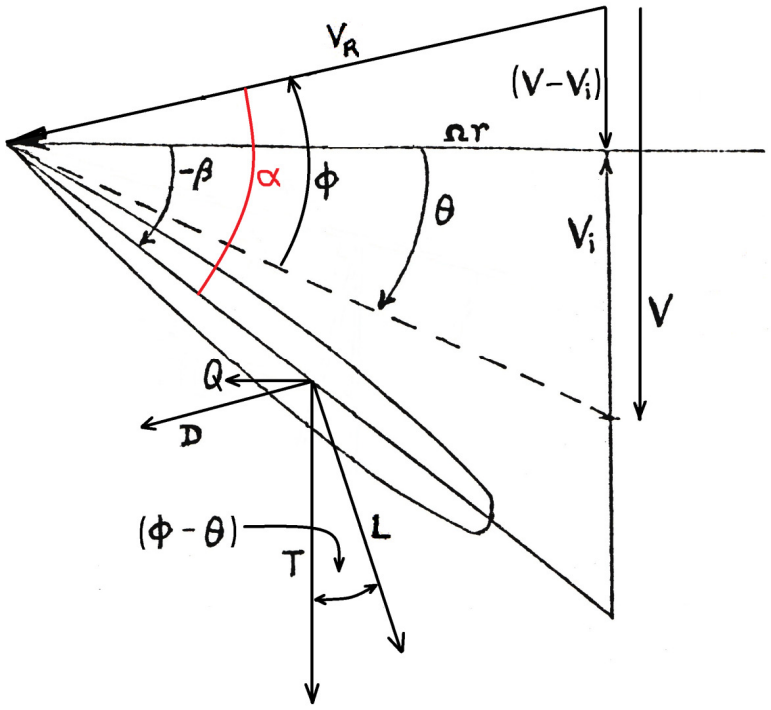

Figure 2-8 Vectors and forces for a negative pitch blade element with large wind velocity.

The amended magnitudes and directions of the vectors and forces are presented in *Figure 2-8*. The main point of *Figure 2-8* is to illustrate the large negative angle of incidence V_R makes with the airfoil. As a result of such a large negative α (assumed beyond the stall point), sectional data would not be available. The stall of flow over the airfoil means a heavily separated flow can be expected and therefore a large drag component is depicted in *Figure 2-8*. This is very significant when resolving the forces into thrust and torque. In positive thrust cases the drag terms were assumed negligible and omitted from calculations in combined blade-element momentum theory [6 & 7]. This was due to large L/D ratios from the resulting α values. For reverse thrust operation however, prediction of the drag forces may be crucial to accuracy of overall performance calculations.

2.4 Contra-rotating propellers

Since the early days of powered flight there was the realisation that a loss of useful energy occurred in the wake of a propeller. The motion imparted to the air by the propeller can be split into axial, radial and tangential velocity increments of which only the axial is useful. The introduction of a second propeller, behind the first and rotating in the opposite direction can further increase the axial velocity of the air while also converting the first propellers tangential velocity increments into axial increases. *Figure 2-9* shows a pair of 2D elements from contra-rotating propellers and the velocity diagrams depicting the flow. The flow exiting rotor-1 is the inflow for rotor-2 (V_2 = V_3). The diagram depicts the axial component of V_2 to highlight the velocity increase provided by rotor-1, with blade speed U_1, as well as showing that the exiting flow includes a tangential component. The action of rotor-2, with blade speed U_2, is to increase the axial velocity further while also converting the tangential velocity component into a useful axial velocity increase. The exit flow V_4 from the rotor-2 depicts a mostly axial velocity vector that is much larger in magnitude than V_1.

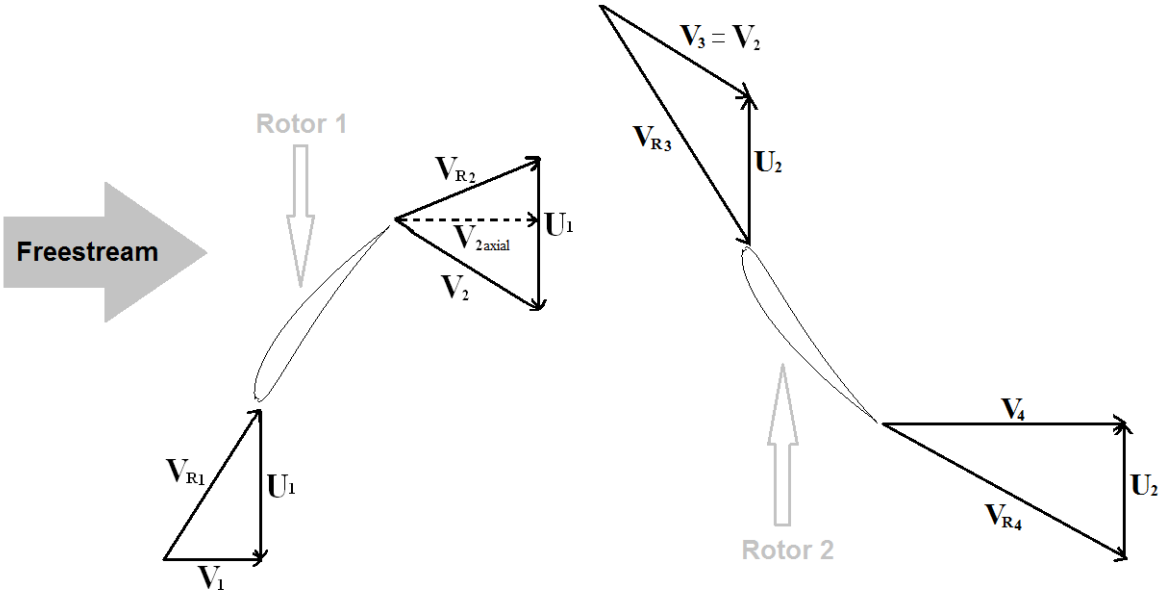

Figure 2-9 Velocity diagram of 2D elements from contra-rotating propellers

With the engine power available from the success of the gas turbine as a method of aircraft propulsion, in the form of turbojet and turboprop engines, subsequent propeller designs were investigated in 1940's and 50's to improve their ability to turn this power into thrust without reaching supersonic tip speeds and their associated losses. The practical advantages of contra-rotation were also being explored. One such investigation [8] consisted of wind tunnel testing of single and contra-rotation propellers, at low Mach numbers, with varying blade numbers. Measurements of thrust and power were obtained and the research produced plots showing variation of thrust coefficient (C_T) and propeller efficiency (η) with advance ratio (J). Two of the original plots (of low quality) have been reproduced from the same experimental data on 4-bladed single and contra-rotation propellers (*Figure 2-10* and *Figure 2-11*). Comparisons of C_T and η for both propeller types are done on the basis of equal power since contra-rotation uses more power than a single rotation - <u>at the same values of β</u>. Therefore the contra-rotation propellers were operated at low values of β. On examining the lines of constant power coefficient (C_P), a slight increase in C_T is provided by contra-rotation over single rotation, which becomes much more substantial at lower values of J. The effect of increasing power is also much more pronounced at these lower values of J.

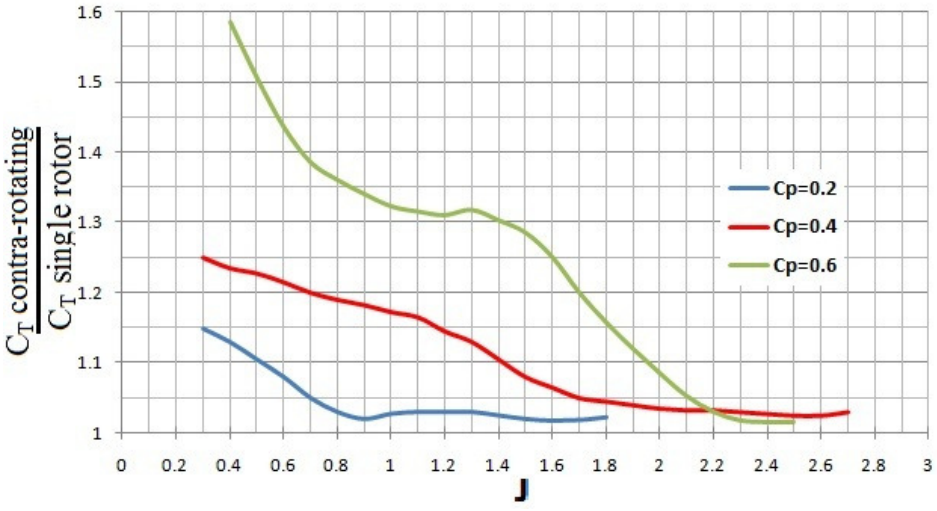

Figure 2-10 Effect of contra-rotation on thrust coefficient for 4-bladed propellers at constant power [8].

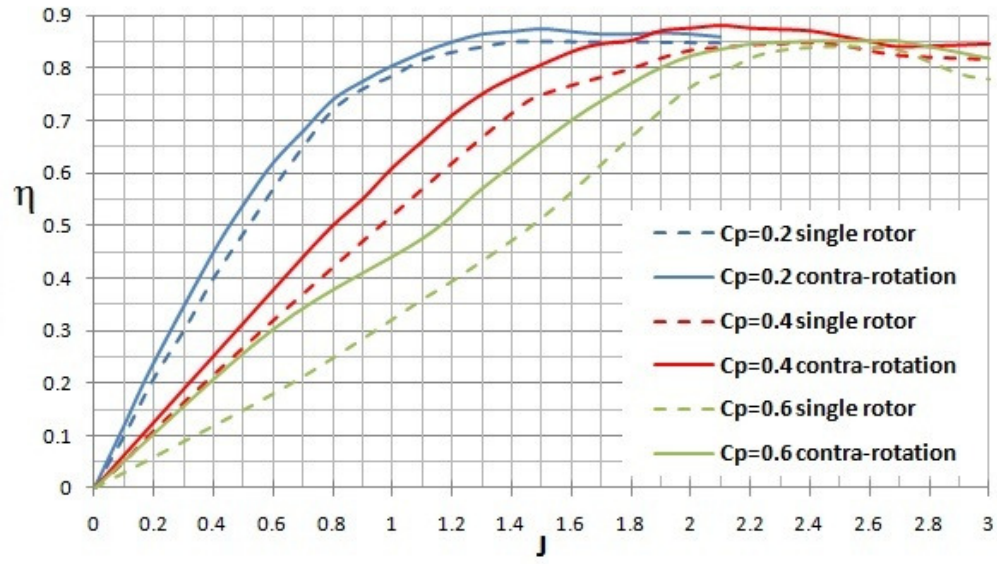

Figure 2-11 Effect of contra-rotation on efficiency for 4-bladed propellers at constant power [8].

The effect of contra rotation on η can also be seen (*Figure 2-11*) in lines of constant C_P for the same propellers. Similarly to the previous plot of C_T, contra-rotation provides slight gains in η at large J which become more significant at lower values. These efficiency gains are positively affected by increased C_P for the lower J range. Since contra-rotation can absorb more engine power than a single propeller, at similar values of β, more thrust can be provided by the contra-rotation propellers.

Investigations during the 1940's into contra-rotation, as well as other parameters in propeller design, saw a number of engines enter into service. The Allison T40 engine powered a number of aircraft; including US Navy craft like the Convair R3Y Tradewind, North American XA2J Super Savage and Douglas A2D Skyshark (see ***Figure 2-12***).

Figure 2-12 Douglas A2D Skyshark [9].

Figure 2-13 Avro Shackleton with Rolls Royce Griffon engines on display in S.A.A.F Museum [10].

A contra-rotating propeller variant of the well-known Lancaster bomber was developed in Britain in the early 1950's. The Avro Shackleton, see *Figure 2-13*, used 4 Rolls Royce Griffon, 6-bladed contra-rotating, piston prop engines. This same contra-rotating engine even powered a version of the Spitfire.

It was research like this in former U.S.S.R. that led to turboprop engines like the NK-12 being designed and built in the 1950's. This engine is the most powerful turboprop in

the world and with its 8-bladed contra-rotating propellers it powers the Tupolev Tu-95 strategic bomber. First flown in 1952, this bomber is still in service today and is shown in *Figure 2-14*. A variant of the Tu-95 is the Tu-114 airliner, which first flew in 1957, and is the world's fastest propeller driven aircraft [11].

Figure 2-14 Tupolev Tu-95 Strategic Bomber with NK-12 engines [12].

Despite the benefits of contra-rotating propellers being known for decades, the amount of production aircraft utilizing this propulsive design is small. Prior to the renewed interest in 1970's due to oil crisis, which is the subject of the following section, these propeller engines had generally not proven viable because of higher cost and lower reliability which greatly offset the benefits. A paper published in 1982 [13] states that in cited historical aircraft, the use of contra-rotation propeller systems often involved radical departures from previous design practices. In some cases the introduction of a contra-rotation system design added considerable complexity and weight which in turn increased cost and maintenance requirements. Insufficient hardware development in critical areas like oil seals, pumps, hydraulic motors, gear trains, bearings etc led to extensive operational problems from internal or external leakages to actual gear train failures. The author of the paper [13] notes this, more than increased cost, as discouraging the further use of contra-rotation in the past. As well as this lack of

refinement in the appropriate technologies was a lack of stringent design conditions (e.g. propeller disk loading, blade Mach number) that hampered the full potential of contra-rotating propellers. None of these issues raised were flaws of the concept and they were all workable if given the appropriate research and development. However strong post-WWII moves towards jet propulsion reduced propeller development and the majority of funding for propeller research went to single-rotation turboprops.

An issue that was fundamental to the concept did come to light however in the late 70's during the renewed period of interest. In 1977 the International Civil Aviation Organisation (ICAO) introduced noise certification standards in Chapter 3 of Annex 16 – Environmental Protection Volume 1. Consequently certain noise restrictions were imposed on aircraft that were designed prior to 1977, and all subsequent aircraft certifications after 1977 would have to meet 'Chapter 3' requirements. This posed a particularly big dilemma for contra-rotating propellers due to: a) acoustic interference between the individual noise fields produced by the two propellers and b) aerodynamic interference due to the unsteady loading of one propeller as it operates in the wake of the other propeller [14]. Turbofans have the advantage of the nacelle and cowling absorbing some amount of engine noise. Despite some engines at that time meeting the 'Chapter 3' noise restrictions after considerable effort at the design stage, the ICAO in 2001 published 'Chapter 4' noise restrictions which came into effect in 2006. This lower level of acceptable noise for all newly certified aircraft, combined with the current ACARE noise reduction targets for future engines, poses a considerable challenge for engine manufacturers developing contra-rotation designs today.

2.5 Advanced propeller backround

The fuel crisis of the early 1970's sparked a wave of research into increasing engine efficiency and reducing specific fuel consumption. In 1975 the NASA Lewis Research Centre, in conjunction with industry partners, initiated a research program addressing advanced high speed propeller technology. The goal of this program was to extend the high propulsive efficiency realisable by propellers to the 0.6 - 0.8 Mach number range which is of interest for commercial transport aircraft. Preliminary studies and

subsequent flight testing [15] indicated potential fuel savings of 30% compared to turbofan engines at that time.

The high efficiency of propellers is from the concept of imparting a small increase in velocity to a large mass of air, as opposed to a turbojet which imparts a very high velocity increase to a small mass of air. Conventional 2, 3 and 4 bladed propeller engines were limited to lower speeds due to blade tip Mach numbers. The blade design typically had a large thickness, large diameter and small blade loading. Wind tunnel experiments on model propellers with 8-10 thin, highly loaded, swept blades gave promising results [16] which led to NASA and their partners studying and testing 3 design configurations extensively during the 1970's and 1980's, which were single rotation advanced high speed propeller, gearless contra-rotation and geared contra-rotation. These advanced propellers were smaller in diameter than conventional propellers made up of a large number of thin, highly swept blades. The designs became known as 'propfans' as they intended to offer the speed and performance of a turbofan, with the fuel economy of a turboprop. A 'propfan' can be described as a modified turbofan engine with the fan placed outside the engine nacelle. They can be designed in either a pusher-style configuration (where the blade rows are at the aft of the engine - *Figure 2-16*) or a puller-style (where the blade rows are at the front of the engine - *Figure 2-18*) also known as a tractor configuration. Although the terms 'propfan' and 'open rotor' are widely used it should be noted that these types of engines are also called 'unducted fan' or UDF® and 'ultrahigh bypass' or UHB.

NASA's research in collaboration with industry partners came to fruition in 1986 and 1987 when three distinct designs were flight tested after more than 10 years of component design, wind tunnel experiments and ground testing. These three engines are the Allison 501-78M, PW-Allison 578DX and the GE36 UDF. A brief description of each engine is given in the following sections.

In the late 1980's however, the motivation for propfan development diminished as the price of oil dropped and stabilised. While these engines demonstrated the proposed benefits, there were penalties discovered in the form of installation difficulties, increased complexity of maintenance and the most significant of increased noise compared to turbofans. Cost analyses led industry to shelve the concepts in favour of

advanced turbofans. Since most of the research was aimed at turbofans only a small portion of available research was dedicated to propellers. The single-rotation advanced turboprop received most of the attention from engine manufacturers and contra-rotation development was left mostly idle until recent times. Russian and Ukrainian efforts kept alive the interest in propfan development during the late 1980's continuing into the 1990's and has yielded two engines, NK-93 ducted propfan and Progress D-27 which are described briefly in the following sections.

2.5.1 Allison 501-M78

This engine is a single rotation puller-style propfan - *Figure 2-15*. This model uses a version of the T701 turboshaft engine originally tested on the left wing of a modified Gulfstream II aircraft and first flew with the propfan blades installed and operating on 29th April 1987 [17]. The engines 8 blades, designated SR-7L, were built by Hamilton Standard as a result of aerodynamic and acoustic research under part of the NASA/Lockheed Georgia Propfan Test Assessment (PTA) [18]. The SR-7L blades are part of the blade series SR-XX, all the designs of which were the subject of extensive wind tunnel testing from 1976 to 1986. Because of funding limitations, and also to simplify the analysis, the preliminary work of the PTA was directed towards single rotation design. Performance predictions based on early results from these blade tests encouraged funding for contra-rotation research. During the Allison 501-M78's 73 flights, the engine flew at a Mach number of 0.89 at 29000ft [17].

Figure 2-15 Allison 501-M78 Advanced Turboprop on display at NASA PSL [19].

2.5.2 GE-36 UDF

This engine is a gearless contra-rotation pusher style propfan (*Figure 2-16*). It has a direct-drive arrangement where the gearbox is replaced by a low speed 7-stage turbine. The turbine rotors drive the forward propeller while the disconnected, or 'unearthed', stators drive the aft propeller in the opposite direction. The blades of the propfan are designated F7-A7 and were developed by NASA and GE as a result of wind tunnel testing of contra-rotation models which started in November 1984. The aerodynamic, aeroelastic and acoustic design codes developed for single rotation propfans formed the basis of the codes used for contra-rotation analyses. The F7-A7 design, part of the blade series FX-AX, was chosen because of its demonstrated high efficiency during rig testing at NASA Lewis. Even though the design point for the blades was cruise at Mach 0.72, their efficiency of 77.5% at Mach 0.8 was deemed suitable to demonstrate the 'proof-of-concept' objectives at a substantially lower cost than that of a new blade design with cruise at Mach 0.8 [20]. Each blade is made of advanced composite material showing flutter free, stable behaviour employing directional stiffness and strength with a good resistance to Foreign Object Damage (FOD). The blades were part of aerodynamic and acoustic research conducted as part of the PTA [21]. Using a F404 gas generator as the core of the engine, the UDF began ground testing with the blades installed and

operating in August 1985. After static testing, the UDF was flight tested on a Boeing 727 between August 1986 and Feb 1987. The flight test program showed the UDF to have a Specific Fuel Consumption (SFC) of around 30% less than the JT8D engine companion on the other side of the aircraft. The UDF was then flight tested on an MD-80 from May to August 1987 [18]. The MD-80 flew with the UDF to the Farnborough Airshow in 1988 demonstrating to the world the fuel savings achievable with the technology.

Figure 2-16 GE-36 UDF mounted on MD-80.

2.5.3 PW-Allison 578DX

In February 1986 Pratt & Whitney and Allison formed a joint venture company called PW-Allison Engines in an effort to build a propfan demonstrator engine, to power the MD-80 aircraft. The demonstrator engine is called the PW-Allison 578DX (***Figure 2-17***). This engine is a geared contra-rotation pusher style propfan, with 2 fans each made up of 6 Hamilton Standard blades designated CRP-X1. The tail cone rotates with the aft fan. During the same period that NASA and GE were developing the blades for what was going to be the UDF, NASA and Hamilton Standard were collaborating on their own version of a contra-rotation design, the CRP-X1 model. This research was also part of the PTA. Results for the blade design showed a high efficiency for Mach

numbers in the range of 0.7-0.8 [21]. The efficiency was also shown to remain high over a wide range of power loadings. The 578DX uses a differential planetary gearbox to appropriately match the speeds of the turbine and fans. Details of the gearbox specifically designed for this engine can be found in [22]. The 578DX flew its first of 14 test flights with the MD-80 on 13th April 1989 [17]. During the tests the engine flew at Mach 0.78 at 30000ft. It achieved a maximum thrust delivery of roughly 20,000 lbf.

Figure 2-17 PW-Allison 578DX contra-rotating propfan

2.5.4 Ivchenko Progress D-27

This engine is a contra-rotation, puller or tractor style, propfan called the Progress D-27 (*Figure 2-18*). Made by Ukrainian engine manufacturer Ivchenko-Progress and developed in the late 80's to early 90's, it is the first propfan to go into production and currently powers the Antonov AN-70 airlifter which uses four of the engines and cruises at Mach 0.7. It offers a 25%-30% reduction in fuel burn compared to todays turbofans [23]. The D-27 uses a propeller design called SV-27, made by Russian company SPE Aerosila, which has wide-chord scimitar shaped blades made of polymeric composites

that give a cruising efficiency of 90% [24]. The SV-27 design has 8 blades in the forward fan and 6 in the aft fan.

Figure 2-18 Ivchenko Progress D-27 contra-rotating propfan on Antonov AN-70 [25].

2.5.5 NK-93

This engine is a contra-rotation, puller or tractor style, ducted fan made by Russian engine manufacturer NK Engines (Nikolai Kuznetsov). It is labelled by some as potentially the most fuel-efficient aircraft jet engine ever to be tested [26]. It has 8 blades in each fan that notably uses variable pitch even though the fans are shrouded or ducted. Conceptual development began in 1986 with the first complete engine run in 1991. From 1992-95 it's reported that over 10000 hours run time has been executed on 5 engines and in 2001 the company announced an even larger test program that would eventually utilise a planned total of 15 prototype NK-93 engines. It is rated at 40,000 lb thrust and can be seen in *Figure 2-19* [27]. It has also demonstrated reverse thrust capabilities of up to 8,300 lb through blade pitch angles despite being ducted [28].

Figure 2-19 NK-93 Ducted Contra-rotating Propfan [29].

2.6 Propeller reverse thrust

Previous work on investigating negative or reverse thrust of propellers started in 1930's as its potential benefits have been long known. Some of the earliest negative thrust research [30] was conducted in 1934 on a 2-bladed propeller that was tested in a wind tunnel through a β range of +22° to -23° in front of a cowled radial engine nacelle. The negative thrust and torque results, obtained for various values of advance ratio (J), showed that the maximum negative thrust increases with decrease in β. By conducting additional tests with the propeller and nacelle mounted on a test monoplane wing and a bi-plane wing the research showed that negative thrust is considerably affected by the shape and size of the body behind the propeller. The benefits of negative thrust at the time of research stated were a reduction in dive speed, not just for accuracy of dive bombing, but to also maintain control of aircraft and lessen the stresses due to subsequent pull-out.

In 1938 it was stated that even though the advantages of reverse thrust were long realised there was still only a meagre supply of experimental data on the subject [31]. In an effort to add to this data a series of experiments was conducted on 2, 3 and 4 bladed, Clark Y and RAF-6 airfoil designed propellers [31]. The results obtained were for a β range of 0° to +90° while varying J. Conclusions were made that negative thrust could

provide a braking effect for reducing dive speeds and that it could greatly reduce the landing distance of aircraft – which today is the main motivation for thrust reversal. Landing distance was an issue during the time of research because large aircraft were extremely limited to a small number of airfields having the necessary length of runway. Today however, another major driver for lower required landing distance is a reduction in airport charges and aircraft turn-around time. In 1944 NACA experimented on 2 and 4 bladed propellers in single and contra-rotation configurations as aerodynamic brakes [32]. The negative thrust values from these constant rpm tests were compared to the deceleration from a dive flap. They showed that for a given β value with $J > 2$, thrust varies proportionally with the number of blades. When $J < 2$, the negative thrust from the 4-bladed contra-rotation configuration is not proportionally greater.

In 1945 NACA performed tests on 3 and 4 bladed, single and contra-rotation propellers in the negative thrust operation β range of -45° to +145° for a range of J values [33]. Results showed that adequate negative thrusts could be obtained from extremely large positive as well as negative blade angles. This was explored due to negative angles necessitating passing through a minimum torque region with the danger of overspeeding the engine. The research stated that during the contra-rotation tests, the front and aft negative blade angles were equal for all the tests but recognised the possibility that maximum total negative thrust might be obtained from differing angles for front and aft propellers. Conclusions were made from the results that single rotation, at low values of J, produced higher negative thrust coefficients than contra-rotation, but at $J > 1.5$ the opposite is true.

In 1957 it was stated that there was a lack of research effort on high-solidity contra-rotation propellers operating at high values of J, despite the known advantages of greater efficiency, absence of reaction torque and smaller diameter propellers over single rotation propellers capable of absorbing the same engine power [34]. In an effort to improve this, an investigation of single and contra-rotation propellers was conducted at positive and negative thrust at high subsonic Mach numbers [34]. The investigation consisted of tests on 3 and 4 bladed single and contra-rotation propellers in combination with various spinner designs, β values and inlet velocities. One of the conclusions for the negative thrust tests, which were also conducted at large inlet velocities, highlighted

that no significant effect of compressibility was felt on reverse thrust performance up to Mach 0.6.

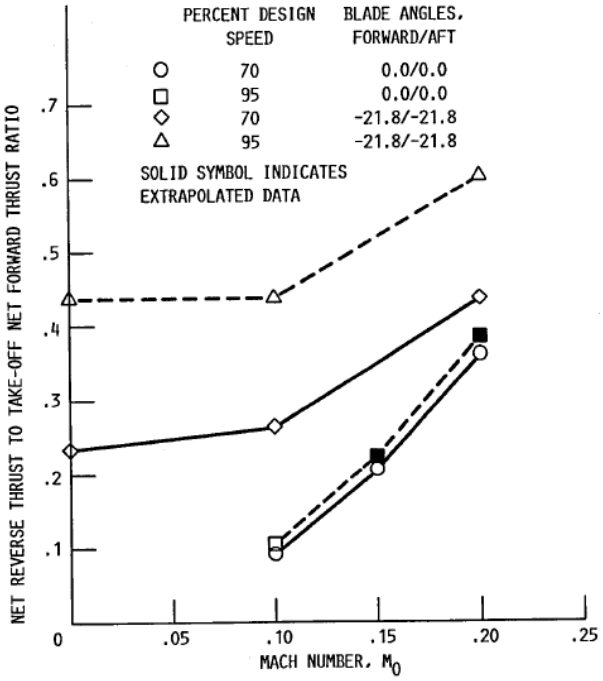

Figure 2-20 Effect of Mach no. on reverse thrust performance of F7/A7 8/8 propeller [35].

In 1988 NASA investigated the low-speed aerodynamic performance characteristics of several advanced contra-rotation pusher propeller configurations with design cruise at Mach numbers 0.72 and 0.8. The blades are from the FX-AX series that was designed and tested by NASA and GE. Various FX-AX blades were tested [35] however only the F7-A7 8-bladed designs were exposed to reverse thrust conditions as they were chosen by GE to be incorporated into their unducted fan engine prior to the research. The experiments were conducted at Mach number range of 0.0 - 0.2 with $\beta = 0°$ (flat pitch) and +21.8°, and run at 70% and 95% of the design rpm. The results (***Figure 2-20***) showed that at Mach 0.2 with 95% design speed, the +21.8° configuration produced a reverse thrust equivalent to 60.4% of the take-off point net forward thrust with static conditions resulting in a reverse thrust equivalent to 43.5% of take-off net thrust. The results also showed the flat pitch configuration did produce practical values of negative

thrust at Mach 0.2 however those values significantly decreased with decreasing Mach number.

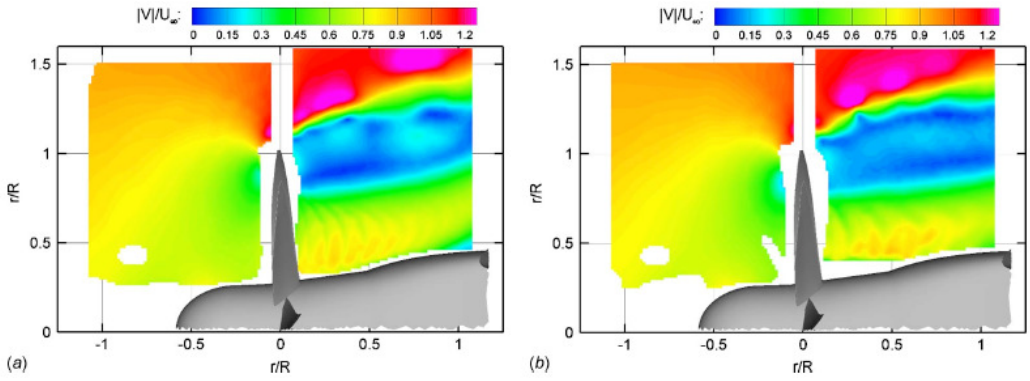

Figure 2-21 Velocity magnitude Cases 1 & 2 given in (a) and (b) respectively [36].

Of the extremely limited research conducted on propeller thrust reverse, only one research case was found by the author on flowfield investigation of propeller thrust reverse [36]. Using double stereoscopic particle image velocimetry (PIV), flow properties like velocity components and vorticity were obtained in scanned sections of the axial symmetry plane, upstream and downstream, of an 8-bladed single propeller engine. These measurements were obtained in a phase-locked sense to investigate the unsteady flow behaviour. It was stated that in uniformly decreasing the blade pitch angles, to produce thrust reverse, the propeller rotational speed peaked at zero thrust [36]. This condition of overspeed is undesirable and can lead to engine damage. In an effort to decrease this peak value, it was proposed to reduce the blade pitch angles in 2 phases. During the initial phase the first set of 4 blades had their pitch angles reduced to a negative thrust setting while the other set of 4 blades are still producing minimal positive thrust. In the subsequent phase the remaining set of 4 blades have their pitch angles changed to a negative thrust producing angle.

Based on this concept, the wind tunnel investigation consisted of 2 test cases of blade pitch. Case 1 had all 8 blades of the propeller at an equal reverse thrust pitch angle, β_1 while case 2 had alternating blade pitch angles. These values of pitch alternated from a base value of β_2, to β_3 for every 2nd blade. It should be highlighted that while the pitch angle values are not given in the publication, it stated that all 3 angles produced

negative thrust and that the following relationship exists between the alternating angles: $\beta_1 = \frac{1}{2}(\beta_2 + \beta_3)$. This results in a similar mean angle of attack for both cases and therefore roughly the same amount of reverse thrust produced [36]. The phase-locked measurements for case 2 were performed with a phase angle increment of approximately 9 degrees so that distinctions can be made between periodic and aperiodic events in the velocity fields. All the experiments were conducted with the same approaching freestream velocity (48m/s) and propeller rotational speed.

The results of velocity magnitude (V) normalised with freestream velocity (U_∞) are shown at the same phase angle and conditions in *Figure 2-21*. Both pitch settings exhibit very similar decelerating behaviour of the flow upstream of the propeller. Both also show and upstream area where the flow velocity reduces to zero, located just below the propeller tip. Downstream of the propeller, it is remarked that the individual blade passages are extremely identifiable just above the nacelle for the case 1 where all the blades have pitch β_1 [36]. In contrast to this there appears to be a merging of every 2 blade passages for case 2 which is assumed to be a consequence of the difference in pitch angle for every 2nd blade.

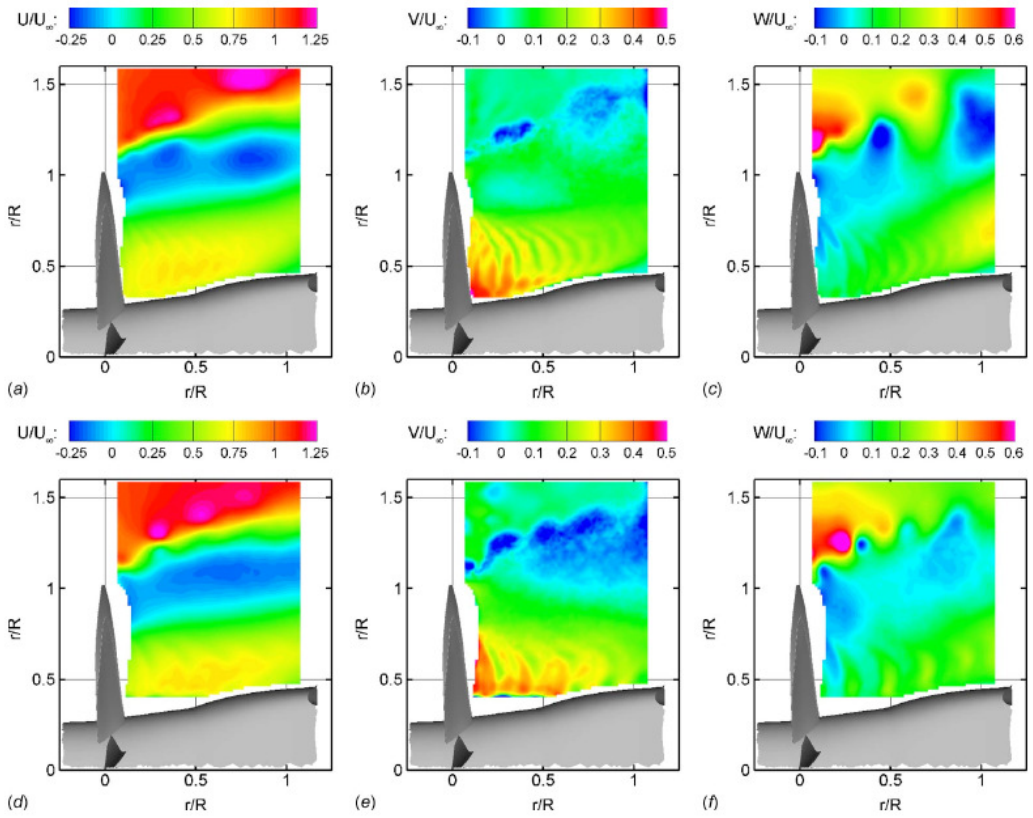

Figure 2-22 Comparison of averaged axial, radial and tangential velocities for the 2 cases [36].

Images of averaged velocity components are presented for comparison to show the differences in the flow of the propeller wake for both pitch settings (*Figure 2-22*). Attention is drawn to the U velocities for both settings. Case 1 results in two distinct areas of reverse flow with the shear layer thickness growing after the first area of reverse flow. Case 2 produces a more uniform area of reverse flow with lower values overall and a mostly unchanged shear layer thickness.

It should be noted that the plots in *Figure 2-21* (and also *Figure 2-22*) represent the only flow visualisations of propeller reverse thrust available in public domain. While flow descriptions in the rest of this section can only be related to the specific propeller design and experimental conditions in [36], further reverse thrust investigations may yield common flow features associated with reverse thrust operation. At the very least, visualisations from [36] show just how complicated the resulting flow is.

3 CFD Methodology

The following chapter describes the overall investigative approach, as well as its subdivisions, into reverse thrust CFD calculations. The methodology for each subdivision is fully detailed and aims to inform the reader of the logical progression of work, the configurations modelled, grid construction details and simulation test matrices.

3.1 Investigative approach

The operating condition of reverse thrust for conventional and advanced propeller engines has received little research effort and the author is unaware of any numerical modelling campaigns prior to this work. As a result there is a complete absence of previous investigative strategies to draw from or validated CFD simulations that show it is even achievable, when considering the highly separated and complex flow expected from this off-design operating condition. A conservative approach has therefore been adopted for this work with the purpose of establishing an initial working knowledge of propeller reverse thrust aerodynamics and simulation. Single rotor operations are used as the starting point for building a knowledge base of computational grid designs for this propeller type and to provide guidance on subsequent improvements. With a lack of experimental data for single rotor reverse thrust operation, the results are scrutinised using previously deduced basic concepts of flow behaviour and the assumed effects of varying the primary parameters. This allowed an initial level of confidence to be established in the single rotor methodology and supported its use for contra-rotation modelling.

As well as a starting point for this work, single rotor calculations can also be used for illustrating the effects of one rotor on the performance of the other, following completion of contra-rotation simulations. For this objective, the same operating parameters and conditions have been used in both the contra-rotation and single rotor simulations.

Three common numerical modelling approaches for turbomachinery multi-stage analysis were considered for contra-rotation.

- Steady-state mixing–plane
- Frozen rotor
- Unsteady rotor-stator sliding mesh

Steady mixing plane approach uses circumferentially averaged flow properties at the interface between the rotor and stator blades. This means the interface cannot simulate large circumferential variations in flow properties associated with significant reverse flow since they are averaged. The mixing-plane technique was unsuitable for the current research as a level of reverse flow across the boundary was expected in all the cases investigated.

Frozen rotor simulations use both rotors in a fixed relative position along with the associated rotation effects for each rotor included through the frame of reference. This produces a steady flow that is dependent on how the rotors are positioned in relation to each other. Despite this gross simplification of the flow, the frozen rotor approach can yield useful information [37] was used for this research since it is a possible method for capturing the basic flow physics of propeller reverse thrust aerodynamics. It is also significantly less computationally expensive than the final method of unsteady sliding mesh simulations.

A sliding mesh model is the most complete type of multi-stage simulation with the ability to obtain time dependant solutions for features like wakes and secondary flows. This technique however has much larger time penalties and computational costs. After building the CFD methodology through initial single rotor calculations this work focused on ‘Frozen Rotor’ approach for contra-rotation cases. However, an initial unsteady investigation using the sliding mesh technique has also been conducted.

3.2 Grid strategy

A decision in meshing strategy was made early in the work to concentrate efforts on unstructured meshing instead of structured arrangements. The rotor geometries are complex with each blade incorporating amounts of twist and sweep along with spanwise variations in blade chord thickness. A structured mesh is clearly possible for this type of geometry, although it is more complex than a hybrid or unstructured mesh. There are grid design codes aimed at multi-stage turbomachinery modelling that can produce fully structured meshes in the entire blade passage flow domain. This approach has been used for contra-rotating open rotors previously [38] [39] [40] where the fully structured mesh of the blade passage, from hub to tip, was united with another separate structured mesh representing the external flow, from blade tip to domain boundary.

However, one of the biggest challenges with the current research is that there is very little information available a priori on the nature of the rotor flow fields. Due to the reverse thrust settings and the expected strong interactions between the blade rows it is difficult to even estimate which direction the local flow will follow. There are expected to be larger regions of separated flows which begin to substantially undermine the potential benefits of following a structured gridding philosophy. A conservatively large domain extent adopted for this work would also result in impractical cell counts using fully structured gridding. Given these considerations unstructured meshing was chosen for the simulation cases of this research with the inclusion of subsequent design improvements that took the following form.

- Domain re-sizing to eliminate non-essential flow modelling
- Re-concentration of cell density in identified areas of interest
- Hybrid meshing with use of hexahedral cells in certain blade wall boundary areas
- Grid adaption based on numerical solution data

3.3 Single rotor simulation

The front rotor of the contra-rotating pair was chosen for initial numerical modelling to start the investigation into propeller reverse thrust. This provided the basic methodology for contra-rotation modelling. It was recognised that single rotor CFD results could not be validated in this case due to lack of experimental data and therefore do not provide an adequate method of reverse thrust investigation on their own. However successful completion of contra-rotation cases would provide a certain level of confidence a posteriori to the single rotor results. These could also be used in identifying the interaction effects of one rotor on the other. For this benefit, operating parameter values have been taken from the contra-rotation test cases for all single rotor simulations. To start building preliminary knowledge of rotor modelling, a positive thrust case was taken first before focusing on reverse thrust. As a consequence the only appropriate front rotor pitch setting used from the experimental dataset is for a front rotor pitch setting of $\beta_1 = +30^\circ$. The blade speed was set to the lower of the 2 speeds for the single rotor cases. For positive thrust production this β value is quite low and will only produce positive thrust at low Mach numbers. It was noted that basic ideal velocity triangles at 70% blade span show that the M=0.05 and M=0.1 cases are expected to result in a positive and marginally positive α respectively. Following on from this, higher M values would produce negative thrust values. Therefore the freestream was set to M=0.05 initially to produce positive thrust.

Figure 3-1 (grid-(a)) shows the full test matrix used with $\beta_1 = +30^\circ$ single front rotor grid. A grid was designed for the front rotor in reverse thrust setting ($\beta_1 = -10^\circ$) based on the previous ($\beta_1 = +30^\circ$) domain and nodal distributions (

Figure 3-1 grid-(b)). This reverse thrust mesh was then used to obtain rotor performance results (summarised in the following chapter). Based on those results, improvements to the grid design were made by reducing the domain extents from original conservative values. Also cell density was reduced in areas of little change in flow behaviour, and increased in areas of interest (identified from initial flow visualisations). With this modified grid for the single front rotor ($\beta_1 = -10^\circ$) the same

previous test matrix was used to obtain thrust and torque readings for comparison with the prior grid design (

Figure 3-1 grid-(c)). These results are given in the following chapter. At this point a grid convergence study was carried out using the modified grid as a base grid. Details of this study are presented in a following section.

The possibility of attached flow on the front rotor blades was identified through resulting incidence angles from $\beta_1 = +30^\circ$ (as previously stated from basic ideal velocity triangles). This was taken into consideration for the contra-rotation modelling. The concept of a hybrid grid was used with a structured mesh wrapped around the blade surfaces of the front rotor. A hybrid grid was built for the single front rotor at $\beta_1 = +30^\circ$ and used with the previous test matrix (

Figure 3-1 grid-(d)). Due to the aft rotor operating with negative pitch settings in the front rotor wake, it was concluded that the aft rotor of the contra-rotating pair would not experience attached flow and therefore would not benefit from structured meshing around the blade surfaces.

Up to this point all the single rotor modelling was conducted using the front rotor at differing pitch settings ($\beta_1 = +30^\circ$ or -10°). With the methodology developed, it was decided to model the aft rotor on its own, before progressing onto contra-rotating simulations. This would allow further performance comparisons and estimation of interaction affects. The hybrid mesh design previously developed for the front rotor was applied to the aft rotor at two differing pitch settings ($\beta_2 = -10^\circ$ and -20°) and thrust and torque results were attained from the test matrix given in

Figure 3-1 grid-(e) & (f).

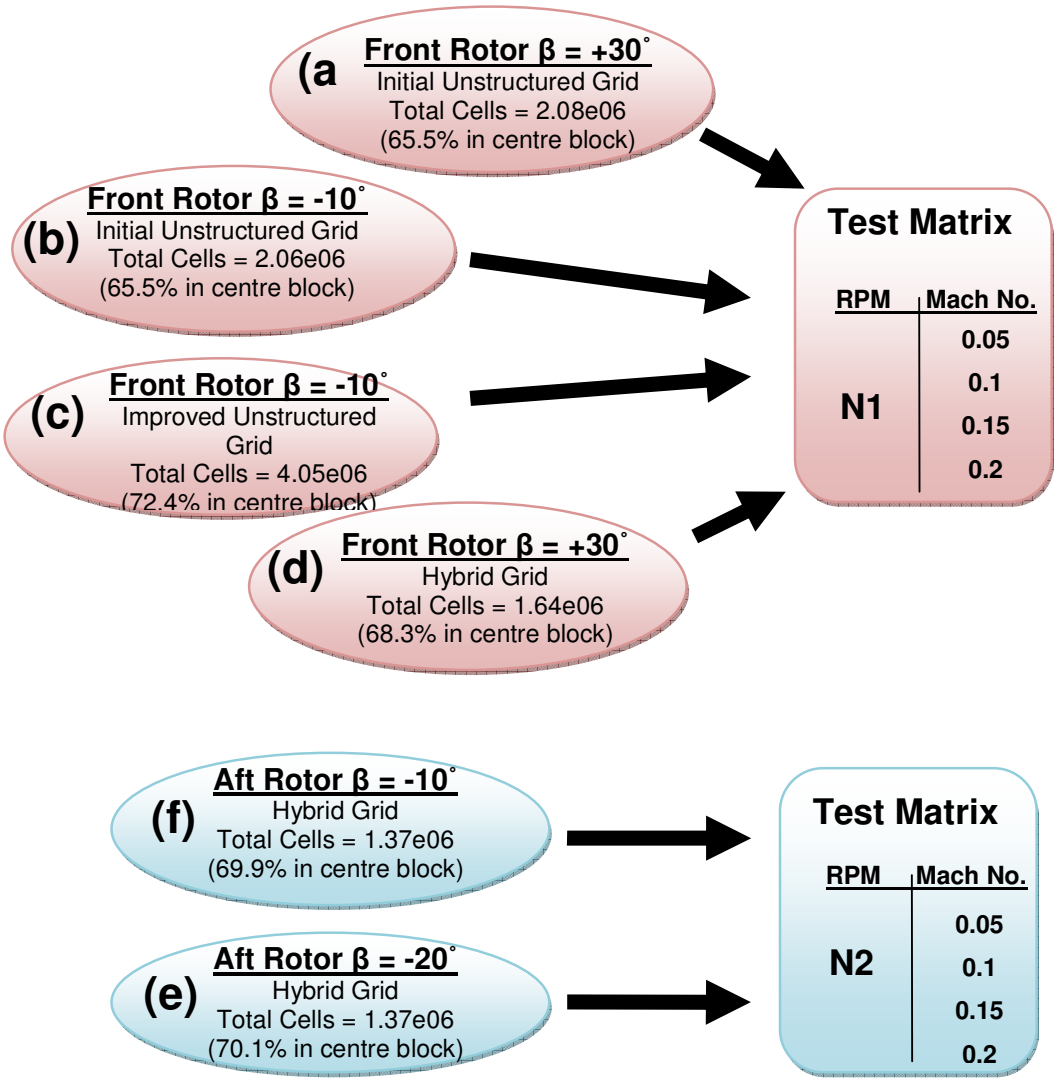

Figure 3-1 Progression of grid construction and test matrices used for single rotor simulations.

3.3.1 Domain & grid generation

For all single rotor modelling, the geometric periodicity enabled construction of only one blade (for either front or aft rotor simulations). The sector-angle of the external flow through the engine was determined from the blade number of the modelled rotor. Geometric relationships for the front and aft rotor blades were provided and used to produce blade geometries consisting of the upper and lower surface blade-forms only (no platforms or root attachment detail). These blades were modelled on a hub of infinite axial length to concentrate on the aerodynamics of the isolated rotors (no modelling of an engine nacelle). An example of this can be seen in ***Figure 3-2***. This decision was influenced by a lack of geometric information on the test rig used for the wind tunnel experiments. While nacelle shape upstream and spinner (or exhaust) downstream of the rotors may have an influence on the overall flowfield, they were omitted from the scope of this research.

To simplify the process of grid generation the blade-forms of the front and aft rotors were united directly to the hub without tapering or rounding-off. While this would have an impact on high fidelity simulations of positive thrust operations, its effect has been assumed to be negligible on this initial numerical investigation into propeller reverse thrust. The blade lengths of the front and aft rotors are defined as L_1 and L_2 respectively.

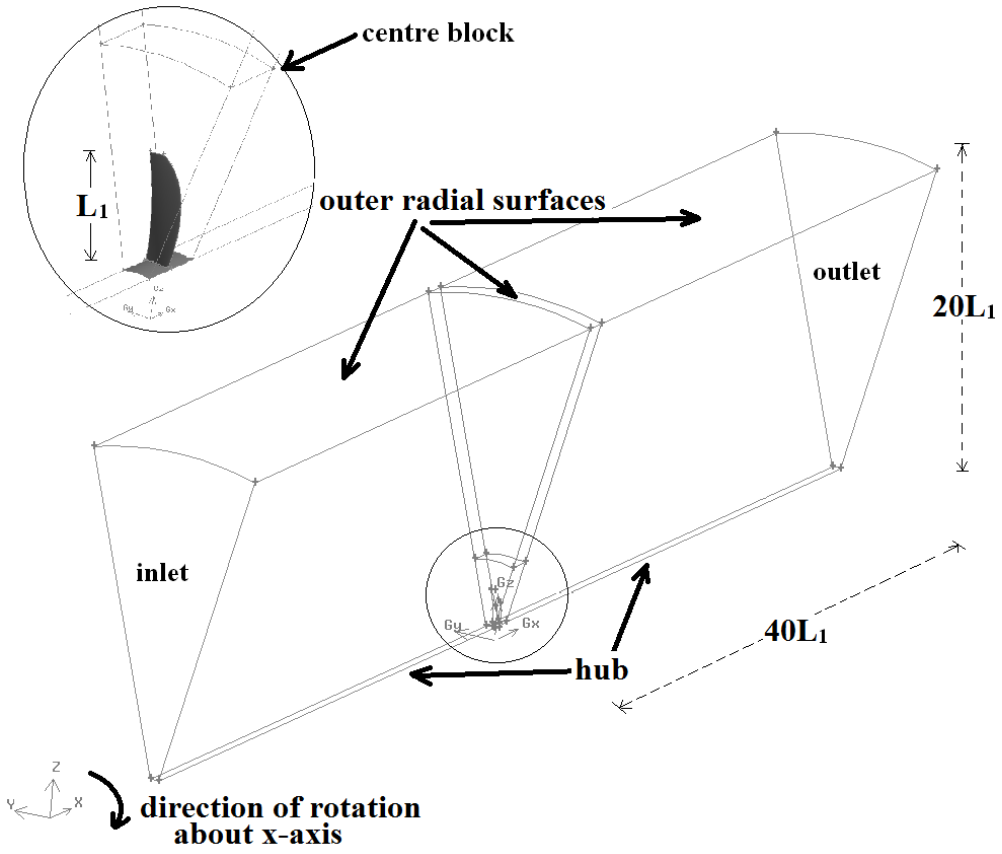

Figure 3-2 Multi-block domain geometry of single front rotor simulation.

For the initial single rotor simulations conservative values of the computational domain extent were chosen in terms of L_1 (since the front rotor was taken as a starting point). Upstream and downstream lengths of $40L_1$ from the blade pitch axis of the front rotor were combined with a radial distance of $20L_1$ from the hub to form the domain (*Figure 3-2*). In an effort to gain more control over nodal distribution, the domain was split into 4 blocks allowing easier concentration of the cell density in the blade areas. The layout of the blocks also facilitated changes in blade pitch as well as the addition of the 2nd rotor in the contra-rotating cases. The central block containing the front blade has an axial length equal to the rotor spacing (x_s) of the contra-rotating design and a radial extent of $2L_1$ from the hub surface (*Figure 3-2*).

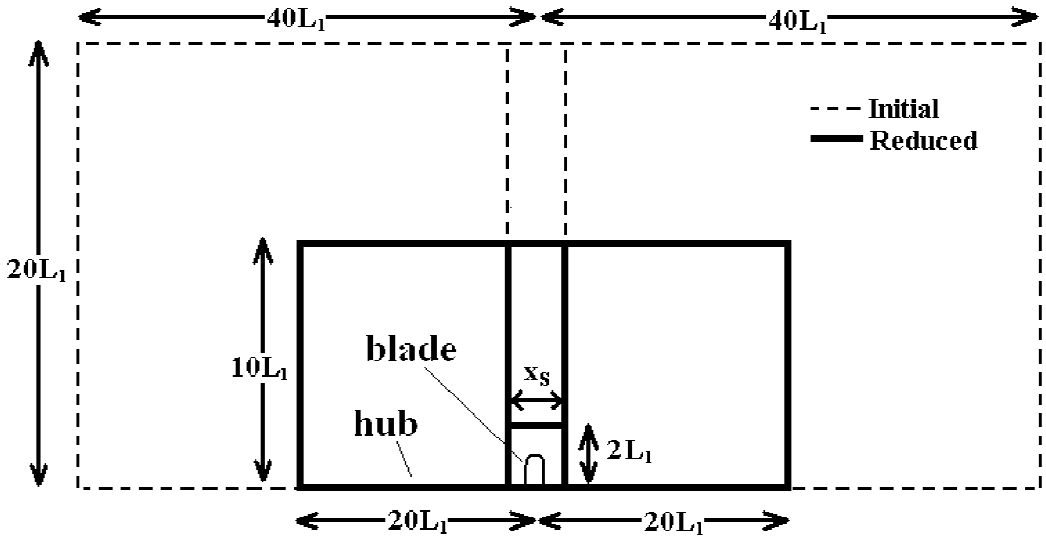

Figure 3-3 Meridional diagram of reduction in domain extent after initial single rotor simulations.

As mentioned in the previous section, results from initial single rotor reverse thrust calculations promoted the reduction in domain extent. Based on contours of static pressure and velocity components, radial domain extent was decreased by 50% to remove modelled freestream flow that was unaffected by the rotor flowfield. Upstream and downstream domain extents were reduced through the same procedure. After CFD results were calculated using the reduced domain, static pressure and velocity contours were examined to see if the boundaries were still outside of the rotor induced flowfield. ***Figure 3-3*** shows a meridional diagram of the originally conservative computational domain (dashed lines) and the amended domain with the blade located in the central block. These new dimensions were used for the remainder of this CFD work with both single rotor and contra-rotating calculations.

For the hybrid grids, structured C-type mesh wrapping was performed around the blade surface with the use of another multi-block structure to overcome difficulties with blade twist, sweep and taper (see *Figure 3-4*). The structured layer was 12 cells deep for all the hybrid grids with a total hexagonal cell count of ~ 33,000 per blade (for single rotor and contra-rotating calculations). The total cell number for each single rotor grid is provided in

Figure 3-1, along with the percentage of total in the domain central block, to illustrate cell density level in the surrounding blade area.

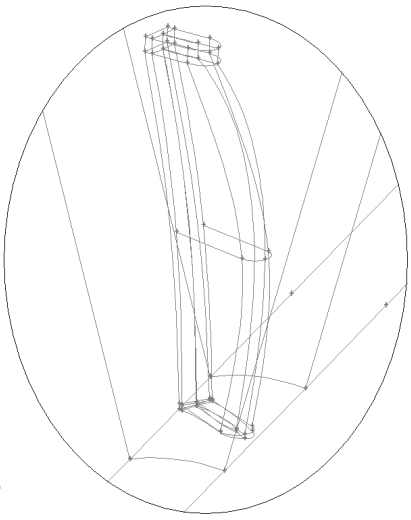

Figure 3-4 Multi-block layout for structured C-type mesh wrap around blade.

3.3.2 Solver settings & turbulence model

The flow was expected to be largely separated due to the negative pitch settings. The viscous flow simulations were conducted using the commercial code FLUENT 6.3 by solving the Reynolds Averaged Navier Stokes equations (RANS). Categorisation of the flow was difficult as the rotors experienced ideal blade tip Mach numbers in the range of 0.2 - 0.5 and all the cases used typical low-speed landing Mach-numbers in the range of 0.05 - 0.2. Compressibility effects were taken into account with the ideal-gas law used to calculate density and Sutherlands law to provide the changes in viscosity due to temperature. A pressure-based solver however was used for the governing equations because it is better suited to low Mach-number range than a density-based solver [41].

$$\mathrm{Re} = \frac{\rho V_R c_{0.7}}{\mu} \qquad \text{.....(6)}$$

The rig scale Reynolds number is defined in eqn 6 where V_R is the ideal relative velocity, $C_{0.7}$ is the chord length taken at 70% blade radius of the front rotor. With the variation in operating conditions, the resulting Reynolds number range of 2.4 – 5.4 ($x10^5$) indicates a non-laminar flow. High levels of expected flow separation due to

large negative incidence combined with this transitional Reynolds number indicated turbulence modelling was required in the current CFD simulations.

The two equation k-epsilon turbulence model was chosen for its robustness, stability and wide applicability [42]. More specifically the RNG k-epsilon model (ReNormalisation Group) was chosen because the turbulent dissipation equation contains an extra term that more accurately accounts for rotation effects on turbulence than the standard k-epsilon model. The SIMPLE algorithm (Semi Implicit Method for Pressure-Linked Equations) was used for the pressure-velocity coupling with the segregated solver. The PRESTO pressure-interpolation scheme was used and the discretisation schemes for all the convection terms were set as 2nd order-upwind for the entirety of each simulation.

3.3.3 Boundary & zone conditions

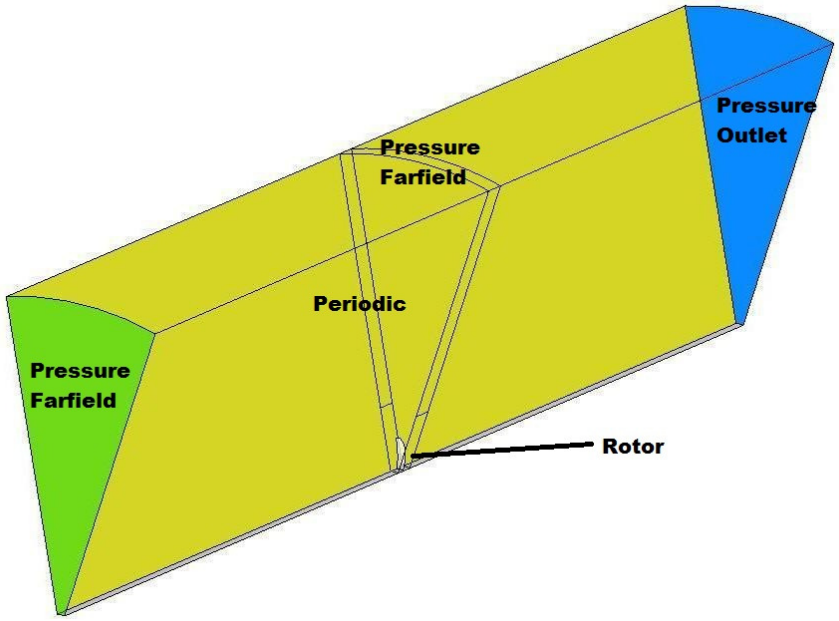

Figure 3-5 Single rotor simulation domain boundary conditions.

Pressure far-field boundary conditions were used for the inlet surface and outer radial surfaces to simulate the free-stream condition (

Figure 3-5). These require an input of inlet static pressure (P), static temperature (T) and Mach number (M) from the experimental work. The outlet surface was chosen as a pressure outlet boundary with the same input of P and T values. The turbulence specification for the boundary conditions used inputs of turbulence intensity and length scale. A conservative estimate of 10% was used for the intensity as it was assumed reverse thrust production does not guarantee ideal external freestream conditions. Turbulence length scale was taken as an estimate of front rotor maximum chord length in the blade mid-section.

Rotation was applied to the domain through moving reference frame, with the angular speed of the domain fluid zones set to the required rotor rpm (N1 and N2 for front and aft respectively). The blade surfaces were set as rotating wall boundaries with a no-slip condition to include viscous effects. The hub was made up of separate surfaces corresponding to the upstream, rotor and downstream sections of the domain. All hub surfaces were set as rotating wall boundaries with the upstream and downstream surfaces having zero shear to avoid boundary layer growth. The rotor hub surfaces used a no-slip condition. The remaining side surfaces extending from the hub to the radial extent of the domain were set as periodic boundaries (*Figure 3-5*)

3.3.4 Iterative convergence

Under-relaxation factors for all cases had to be lowered prior to starting the simulations in an effort to avoid early divergence. The reduced values are present in ***Table 1*** along with the original default values. Residual convergence for the initial grid design has proved to be difficult to achieve in this work. It was evident from initial modelling that continuity residuals were the most difficult to converge. After a reduction in domain extent was implemented for grids (b)-(f), mass imbalance in the outer radial parts of the domain proved to be a contributing factor to early divergence. This was due to mesh coarseness and required grid adaption in the form of refinement using mass imbalance iso-values to highlight cells.

Under-Relaxation Factors	Default	New

Pressure	0.3	0.2
Density	1	0.5
Body Forces	1	0.5
Momentum	0.7	0.5
Turbulent Kinetic Energy	0.8	0.5
Turbulent Dissipation Rate	0.8	0.5
Turbulent Viscosity	1	1
Energy	1	1

Table 1 Under-relaxation values for single rotor calculations.

These issues meant sufficient solution of the flow could not be based on residual convergence alone. Integrated pressure and viscous forces and moments on the blade surface, and their convergence around a constant value, were monitored as an additional criterion. Convergence levels of 10^{-4} for continuity, 10^{-6} for energy and 10^{-5} for the remaining momentum and turbulence residuals were reached in all the single rotor cases. An example of these convergence criteria are given in *Figure 3-6*.

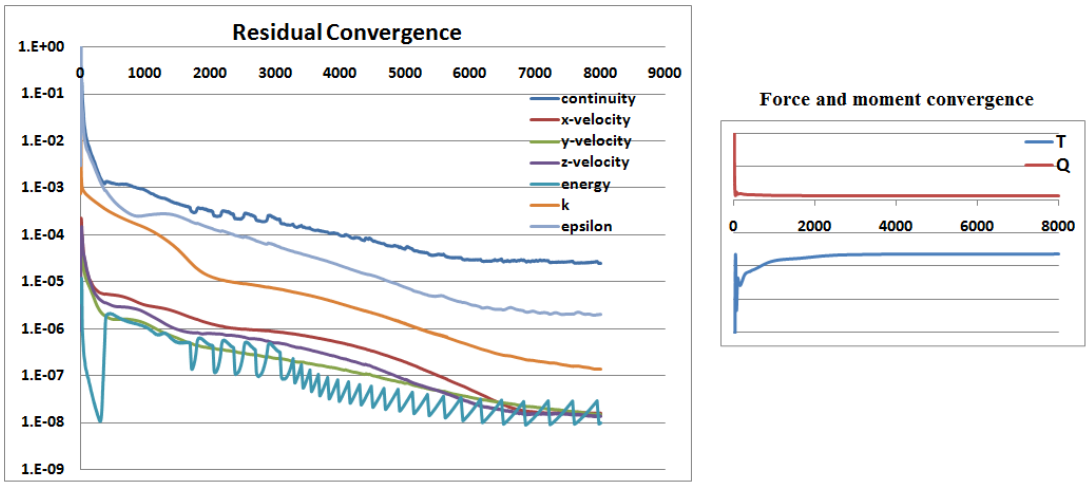

Figure 3-6 Residual, force and moment convergence for single rotor grid.

3.3.5 Grid convergence

A grid convergence study was completed for the improved design single front rotor grid at $\beta = -10^{\circ}$ (

Figure 3-1 grid (b)). The full details and results of this study are given in Appendix A.5 with a summary of the actions and findings given in this section. Thrust (T) and torque (Q) were used as the criteria for judging how dependant the results are on grid design. Ideally for grid convergence studies it is desirable to have structured refinement when varying cell count, even if the base grid is unstructured [43]. In an effort to achieve this, a constant refinement factor of 1.257 was used with cell counts of the base grid domain blocks to produce target cell refinement numbers for each zone. The same factor was applied to produce target coarsened zone cell numbers. These desired cell numbers for each zone were approached through a trial and error process of nodal distribution on edges within that zone. Efforts were made to try and keep the same relative cell density in the previously targeted areas of interest highlighted from the initial grid design. A datum case of rpm = N1 and Mach number (M) = 0.1 was chosen for the coarse, base and fine grids. Due to non-monotonic T and Q values, Grid Convergence Index theory taken from [43] could not be used however T & Q differences of ~14% from the base to coarse grids, and ~13% from base to fine grids were found (see Appendix A.5).

3.4 Contra-rotation modelling: 'Frozen Rotor' approach

With a suitable CFD knowledge base built from single blade row modelling, efforts were then concentrated on modelling contra-rotation. Two different combinations of pitch setting (β_1=+30˚, β_2=-10˚ and β_1=-10˚, β_2=-20˚) for front and aft rotors were used for all the 'Frozen Rotor' simulations, each requiring an individual grid. Geometric periodicity eliminated the need to model the full blade number of each rotor. As mentioned in the previous section, a hybrid grid design was applied to both pitch combinations with structured meshing around the front rotor blades and unstructured meshing of the remainder. A grid for the pitch setting of (β_1=+30˚, β_2=-10˚) was built initially and subject to a grid convergence study which is summarised in Appendix A.5. This grid was then used with the test matrix in *Figure 3-7*. As stated in previous sections, all operating cases in each test matrix used for the current CFD work correspond to the experimental data. Individual rotor performance characteristics like thrust (T) and torque (Q) were calculated for comparison with experimental measurements and the resulting flowfields were investigated. This hybrid grid design was then applied to the remaining pitch setting (β_1=-10˚, β_2=-20˚) and used with a test

matrix taken from experimental data (*Figure 3-7*) to generate sets of performance and flowfield results.

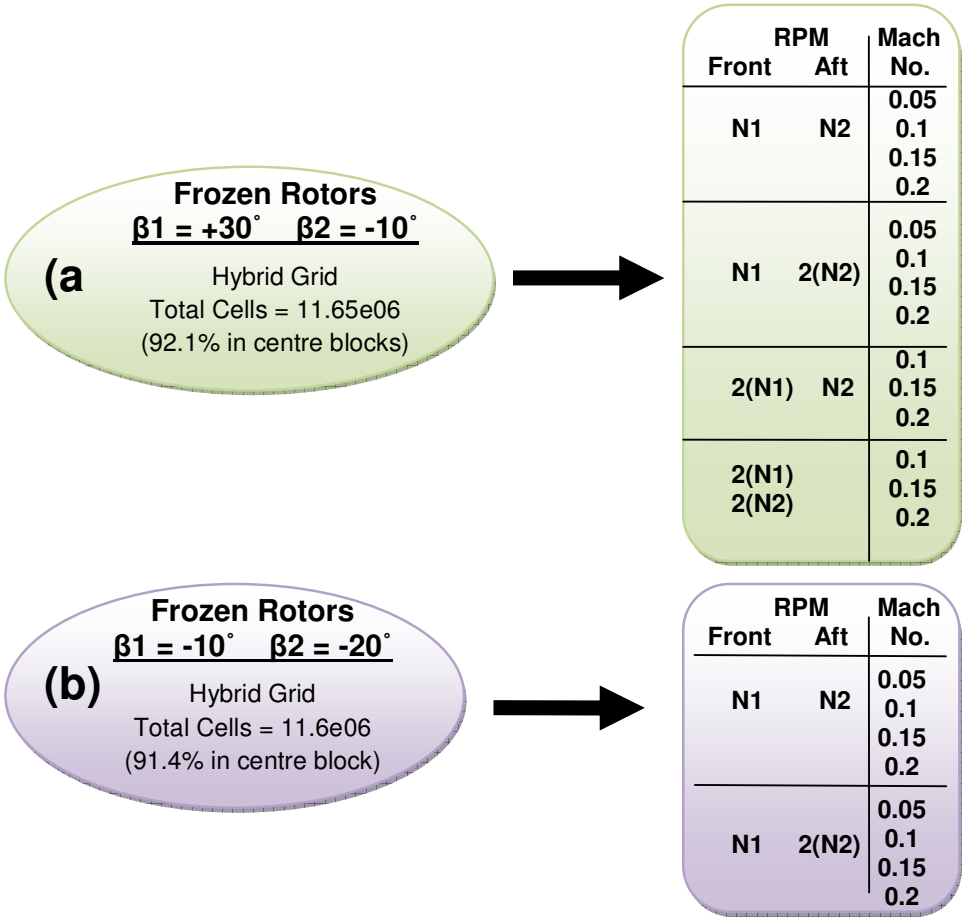

Figure 3-7 Progression of grid construction and test matrices used for 'Frozen Rotor' contra-rotation simulations.

3.4.1 Domain & grid generation

The multi-block approach used for the single rotor modelling facilitated the addition of 2 new blocks for the aft rotor and its outer radial domain (see *Figure 3-8*). Due to different blade numbers on the front and aft rotors, it was necessary to construct more than one blade per rotor and the sector-angle of the external flow through the rotors corresponds to the geometric periodicity of the contra-rotating pair. This can be seen in *Figure 3-9*. The blade rows were (rotationally) positioned relative to each other such that the azimuthal midpoint of the front rotor blade passage is rotationally aligned with

that of the aft rotor. This produced a number of different phase positions for the blade of one rotor relative to the other, which allowed an initial indication of relative phase effect.

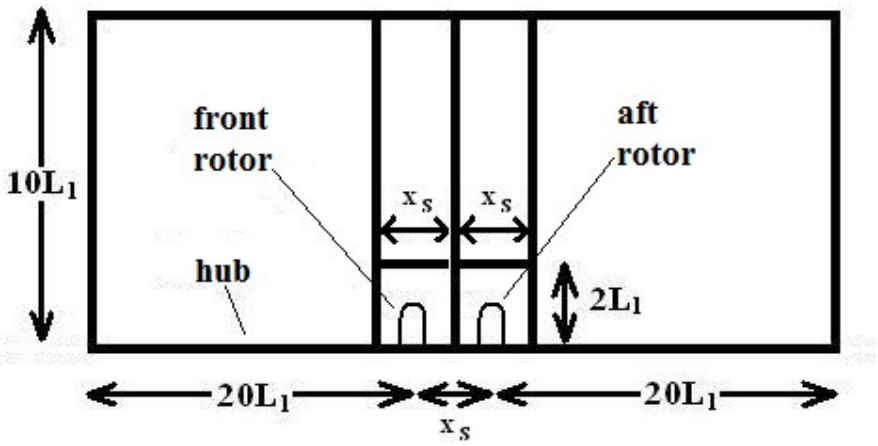

Figure 3-8 Meridional diagram of domain extent for contra-rotation modelling.

The nodal distribution in the various contra-rotation domain blocks is taken as that from the single rotor grids and, where appropriate, repeated to correspond with the desired blade number. As stated in the previous sections, a hybrid mesh design was chosen for 'Frozen Rotor' modelling, and it used the same structured C-type mesh wrap around the blades of the front rotor (for both frozen rotor grids). This structured mesh area was generated using the same method outlined in the single rotor section.

3.4.2 Solver settings & turbulence model

The solver settings used for the contra-rotation calculations were taken as those used in the single rotor simulations. A summary is given below.

- Pressure-based solver
- Ideal gas and Sutherlands law to calculate density and viscosity
- RNG k-epsilon turbulence model
- SIMPLE algorithm for the pressure-velocity coupling with the segregated solver.

- PRESTO pressure-interpolation scheme with 2nd order-upwind discretisation schemes.

3.4.3 Boundary & zone conditions

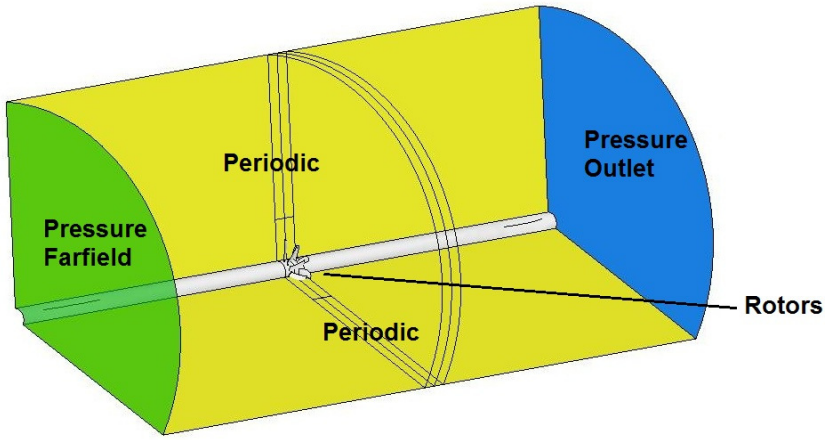

Figure 3-9 Contra-rotation simulation domain boundary conditions.

Boundary conditions for the frozen rotor calculations were chosen as those used in single rotor modelling and are depicted in ***Figure 3-9***, and summarised below.

- Inlet and outer radial surfaces set to pressure farfield
- Outlet surface set to pressure outlet
- Hub surface (upstream and downstream) set to wall with slip condition
- Rotor blade and hub surfaces set to wall with no-slip condition
- Remaining side surfaces set to periodic

Rotation was applied to the domain through multiple moving reference frames, with fluid zones of the upstream block and front rotor domain blocks (inner and outer) set to the desired front rotor rpm. Subsequently the downstream block and aft rotor blocks (inner and outer) were set to the required aft rpm.

3.4.4 Iterative convergence

Under-relaxation factors for all cases were set to those values already established in single rotor calculations and are given in *Table 1*. Integrated pressure and viscous forces on the blade surface, and their convergence on a constant value, were monitored as an additional criterion. Convergence levels of 10^{-4} for continuity, 10^{-6} for energy and 10^{-5} for the remaining momentum and turbulence residuals were reached in all the single rotor cases (see *Figure 3-10*).

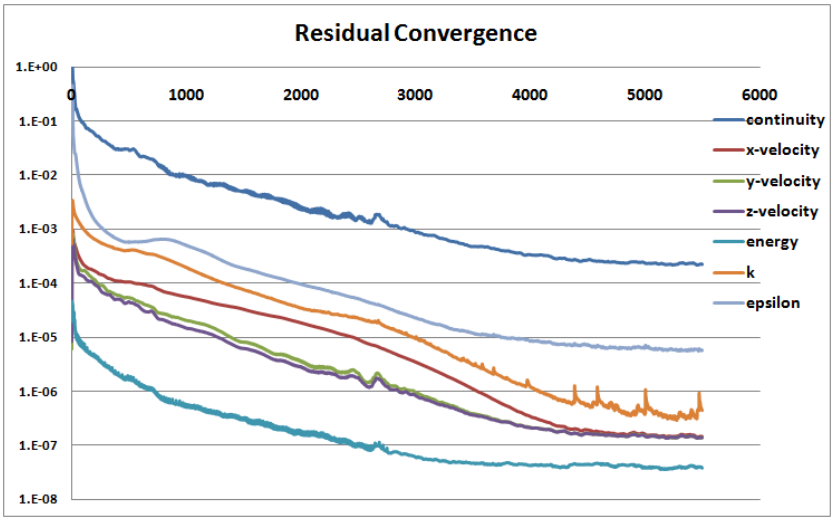

Figure 3-10 Residual convergence for contra-rotation grid.

3.4.5 Grid convergence

A grid convergence study was completed for the frozen rotor mesh at β_1=+30˚ and β_2=-10˚ (*Figure 3-7* grid (a)). The full details and results of this study are given in Appendix A.5 with a summary of the actions and findings given in this section. Thrust (T) and torque (Q) were used as the study criteria for judging how dependant the results are on grid design. Ideally for grid convergence studies it is desirable to have structured refinement when varying cell count, even if the base grid is unstructured. In an effort to achieve this, a constant refinement factor of 1.063 was used with cell counts of the domain blocks to produce target cell refinement numbers for each zone. The same factor was applied to produce target coarsened zone cell numbers. These desired cell numbers for each zone were approached through a trial and error process of nodal distribution on

edges within that zone. Efforts were made to try and keep the same relative cell density. A datum case of rpm = N1 and N2 with Mach number (M) = 0.1 was chosen for the coarse, base and fine grids. Due to non-monotonic T and Q values, Grid Convergence Index theory taken from [42] could not be used however front rotor T & Q differences of ~7% from the base to coarse grids, and ~4.5% from base to fine grids were illustrated. For aft rotor T & Q, differences of ~2.5% from base to fine grids and ~1.5% from base to coarse grids were calculated (see Appendix A.5).

4 Post-processing Methodology

This chapter briefly describes the methodology for post-processing of CFD results. Information is provided on how the rotor and blade performance was extracted. It also details presentation of flowfield properties and illustrates how the 2D and 3D visualisations were obtained.

4.1 Rotor performance

All thrust and torque values from both experimental (dual rotors) and numerical calculations (single rotor and dual rotors) are model scale results, normalised with a constant value of T and Q. The CFD T and Q results are obtained for each blade by summing pressure and viscous forces over the entire surface in the required directions. This was performed automatically using the CFD software. For single rotor results the individual blade values are multiplied by the rotor blade number. For contra-rotating simulations where more than one blade from each rotor is modelled, the blade average is used with blade number to produce rotor performance results for the front and aft blade row.

4.2 Blade distribution of thrust and torque

The blade distribution of thrust and torque was obtained (from frozen rotor simulations) by calculating the pressure force at various spanwise sections of each rotor blade. The viscous forces were deemed negligible for these blade force and moment distribution results because for the majority of cases in this CFD work, the magnitude of the viscous force was less than 1% of the total thrust force. Airfoil slices were taken at 18 spanwise positions, around which the C_p distribution was attained. This permitted the calculation of forces for each of the 18 spanwise sections based on the method described in [44] which is given in Appendix A.6. Once the individual blade force and moment distributions were attained for each modelled blade, the averaged blade distribution for each rotor was then calculated for inclusion in Chapter 5. All blade T and Q distribution results have been normalised with a constant blade T and Q value.

4.3 CFD contours and streamlines

An example of each type of CFD flowfield plot is given below in *Figure 4-1* and *Figure 4-2* with an explanation of how they were obtained. For all the plots however the freestream flow (V) is approaching the blade row(s) from left to right. This is highlighted in *Figure 4-1* along with front and aft rotational directions (N1 and N2 respectively) which are also consistent throughout all the CFD plots. For multiple flowfield property visualisations like *Figure 4-1* contours are taken from a constant angular plane passing through the blade passage mid-point of both rotors. This view is angled slightly so as to better show the 3D nature of the flow which is represented by the streamlines.

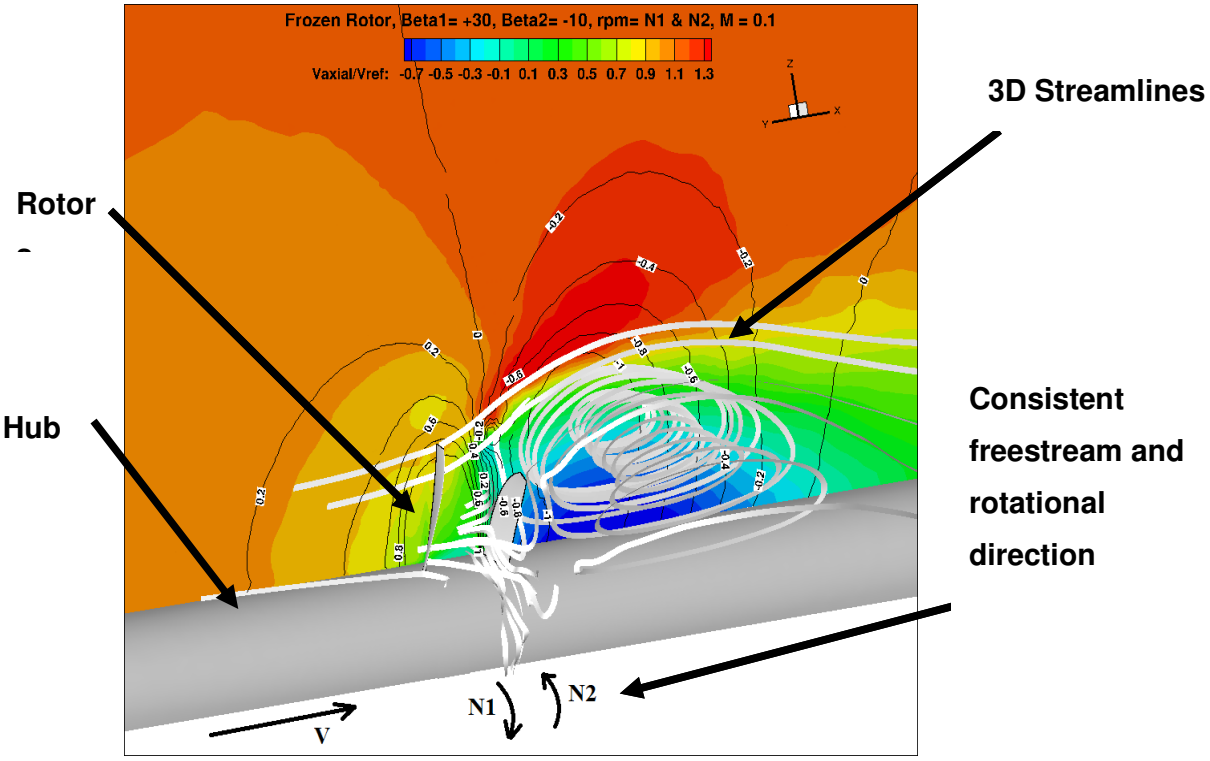

Figure 4-1 Example of 3D flow visualisation from CFD results.

Figure 4-2(a) shows C_p contours taken from a meridional plane passing through the mid-point of the front rotor blade passage but not the aft rotor blade passage midpoint. The relative phase angles of the contra-rotating blade rows are constant for all this type of contour plot.

Figure 4-2 gives an example of circumferential C_p contours taken at 70% front rotor bladespan. All circumferential contour plots, obtained at various spanwise distances, have been unwrapped to a 2D surface and all show the same relative phase positions of the rotors.

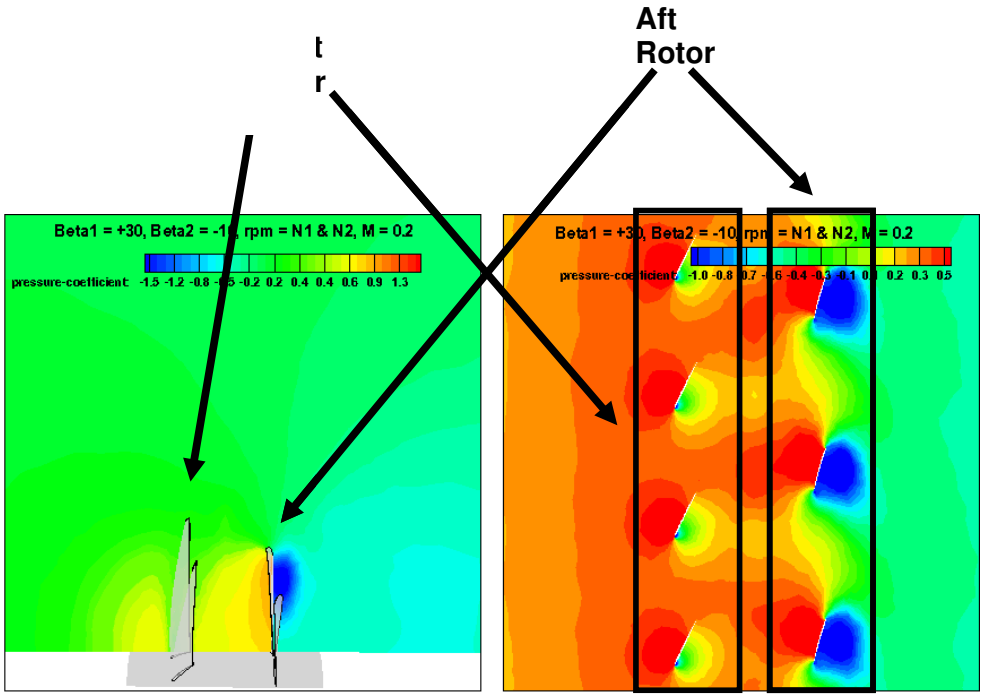

(a) meridional contours (b) circumferential contours

Figure 4-2 Examples of meridional and circumferential contours from CFD results.

5 Results

This chapter contains the results obtained from post-processing of the CFD calculations. For the single rotor simulations, rotor thrust and torque values are given along with some flow visualisation examples. For the contra-rotating rotors, the experimental rotor performance results are analysed and presented with comparable CFD results. The analysis aims to show the effects of varying the primary operating parameters on performance and flowfield properties.

5.1 Single rotor CFD results

This section discusses the singe front rotor thrust and torque results for positive and negative pitch settings before progressing on to single aft rotor results. It also contains an initial assessment of the reverse thrust flowfield from a single front rotor at negative pitch.

5.1.1 Performance analysis

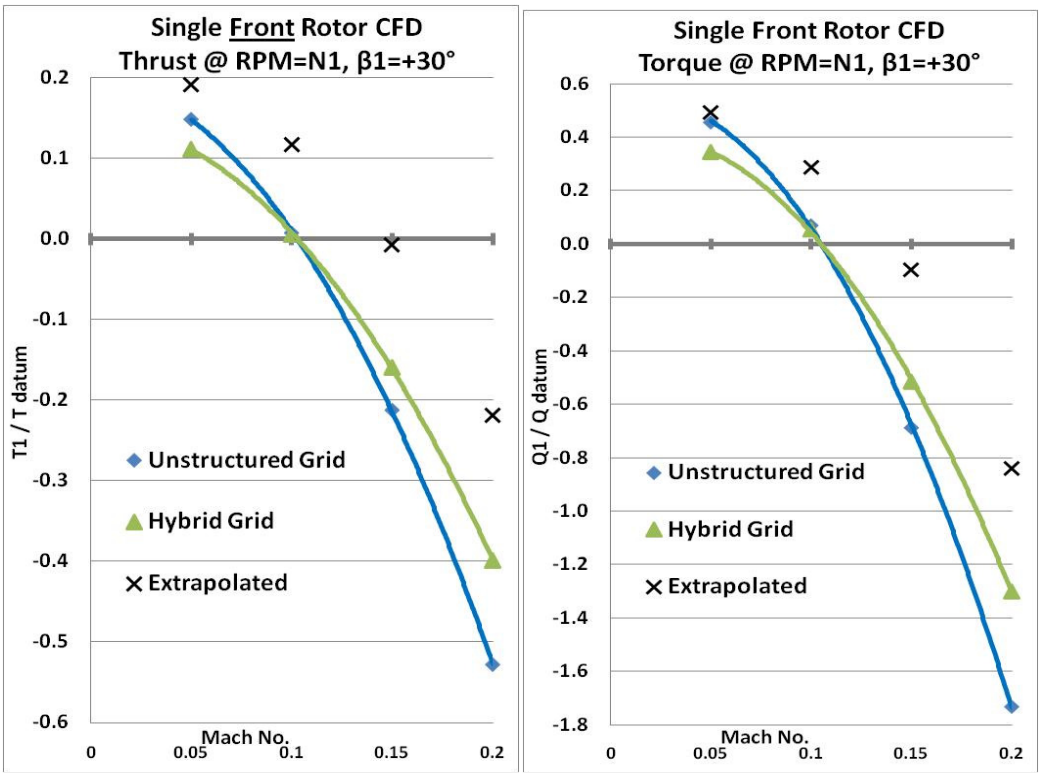

Figure 5-1 Single front rotor CFD T & Q values for β_1 = +30˚.

The CFD calculated thrust (T_1) and torque (Q_1) values for the single front rotor with β_1 = +30˚ and rpm = N1 are presented in *Figure 5-1*, non-dimensionalised with T and Q values. The plots contain results from two grid designs (unstructured and hybrid). As already stated in Chapter 3, no experimental data was available for validation of these CFD results. A method was needed of assessing whether these results have 'sensible' or realistic values. An assumption was made that single front rotor performance was equal to contra-rotating front rotor performance when aft rpm = 0. Based on the experimental data for contra-rotating rotors, extrapolated T_1 and Q_1 values were obtained for front rpm = N1 and aft rpm = 0, from assuming linear relationships between T_1 & Q_1 and the aft rotor rpm. There were also however certain characteristics anticipated for singe front rotor at this pitch and rpm setting.

For positive thrust production, a value of β_1 = +30˚ is quite low and will only produce positive thrust at low Mach numbers. Basic idealised velocity triangles at 70% blade span, where the local blade angle and blade speed are known, show only M = 0.05 and M = 0.1 result in a positive and marginally positive local angle of incidence respectively. Therefore a positive and marginally positive value of thrust is expected at these respective operating conditions. Higher Mach number flow results in an increasingly negative angle of incidence and therefore a reverse thrust of growing magnitude.

This is illustrated in Figure 5-2 (a) showing a positive angle of attack (α) and Figure 5-2 (b) where the airspeed (V) is increased and the resulting relative velocity (V_R) creates a negative angle of attack (-α) with the 2D airfoil. Resolution of the lift (L) and drag (D) forces show that T switches its direction of action. The CFD thrust results in *Figure 5-1* (a) show very good agreement with this anticipated behaviour. The torque results for β_1 = +30˚ are in concurrence with the thrust values. When positive T is generated, a positive Q is experienced. However, a positive pitch blade that operates with a negative angle of incidence will result in a negative torque. Negative torque is traditionally avoided in single-shaft designs since it leads to overspeed of the engine. This is illustrated in Figure 5-2(b) where resolution of the forces from a negative α value produces Q acting in the same direction as the blade speed (U) or shaft rotation.

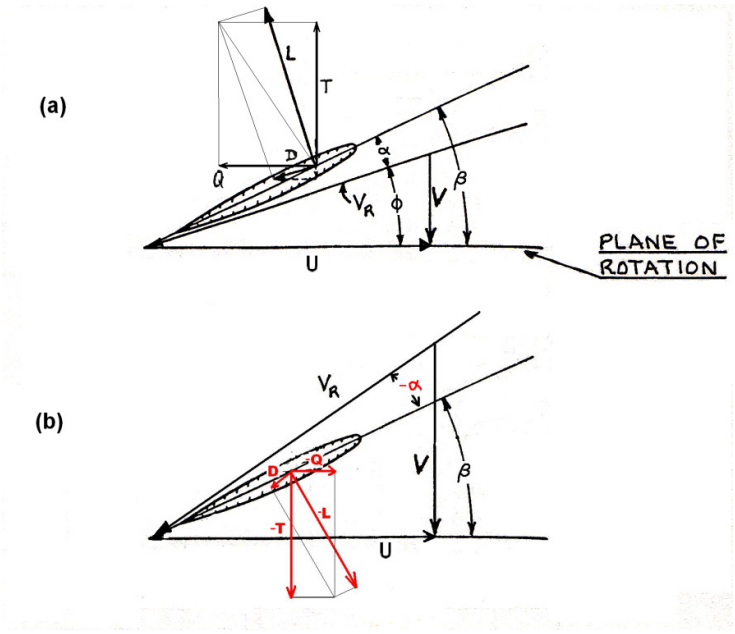

Figure 5-2 Force Diagrams for positive and negative angle of attack.

The CFD performance results for single front rotor at β_1 = -10˚ and rpm = N1 are given in *Figure 5-3*. In similar presentation to the previous results, these plots contain T_1 & Q_1 calculations from 2 different grid designs along with extrapolated values based on experimental data with the same previous assumptions. Thrust values were anticipated to be negative from the ideal force diagram of an airfoil at negative pitch setting (Figure 5-4). The diagram is primarily to show how the directions in which L and D are acting, and their resolution into T and Q. Also deduced from Figure 5-4 is that positive torque forces are expected from negative pitch settings despite resulting incidence angles and thrust values being negative. The CFD T_1 & Q_1 results in *Figure 5-3* show agreement with this statement and as Mach number (M) is increased, larger negative α values result in more reverse thrust produced and therefore more positive torque on the blades.

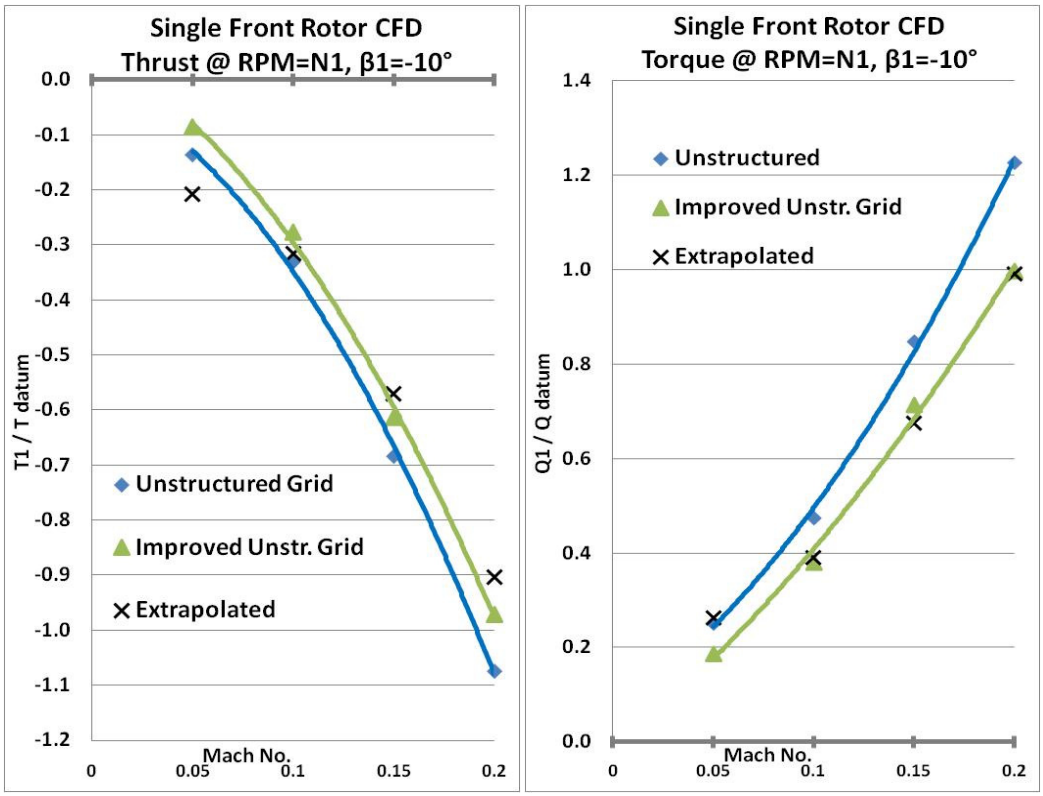

Figure 5-3 Single front rotor CFD T & Q values for β_1 = -10˚.

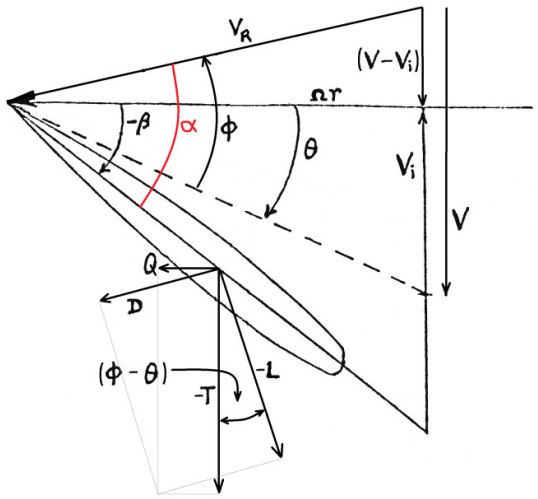

Figure 5-4 Force Diagram for negative pitch angle.

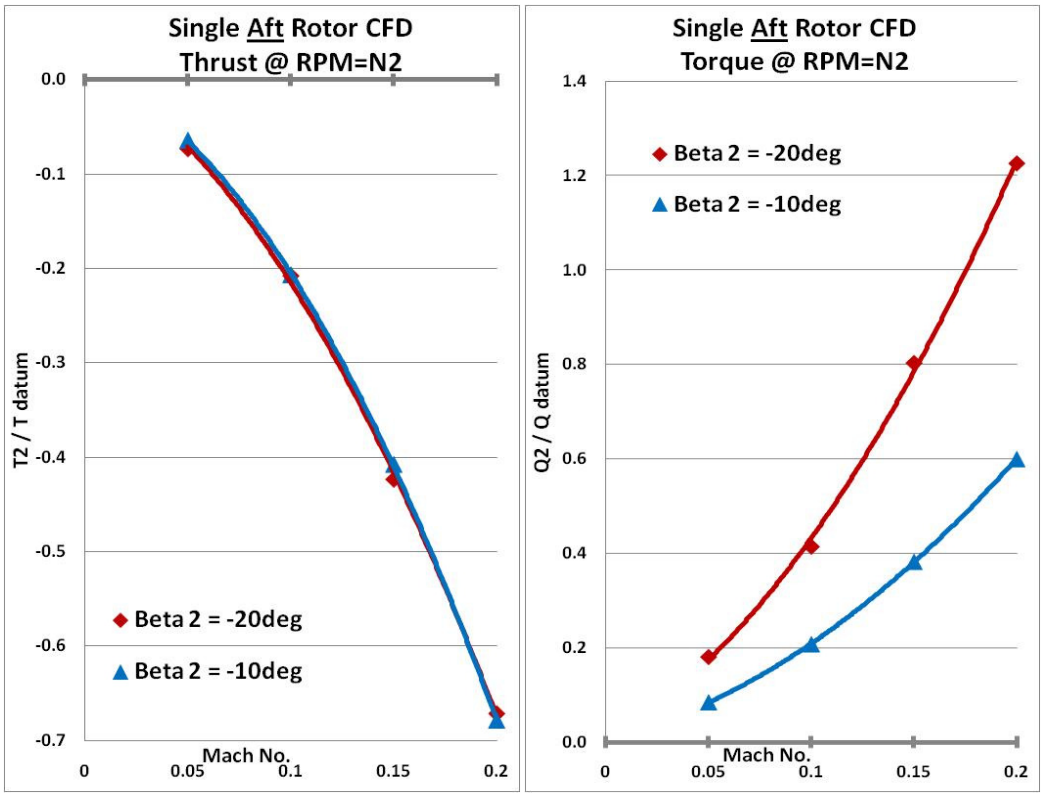

Figure 5-5 Single aft rotor CFD T & Q values for β_2 = -10˚ and β_2 = -20˚.

The CFD performance results for single aft rotor at β_2 = -10˚ and β_2 = -20˚ with rpm = N2 are given in *Figure 5-5*. These plots contain aft T_2 and Q_2 calculations from the hybrid grid for both pitch settings. The direction of these forces along with an increase in magnitude due to larger M was expected. However the thrust results show little difference for an increase in negative pitch while the torque has increased by a factor of 2. One explanation of this behaviour is that the flow is separated over the blade at β_2 = -10˚. Any further increases to negative pitch would cause little change in lift (L) but increase drag (D). *Figure 5-6* illustrates the change in L & D forces on the 2D airfoil, caused by an increase in negative pitch, and resolution of these into T and Q gives a possible reason for the behaviour of the single aft rotor CFD results.

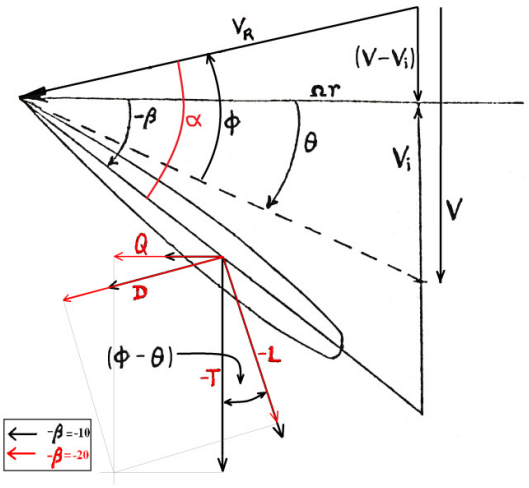

Figure 5-6 Force Diagram showing effect of increased negative pitch angle.

5.1.2 Flowfield assessment

The most dominant flow feature resulting from reverse thrust operation of the front rotor is a large area of recirculation immediately downstream of the blade row. This can be seen through the use of 3D streamlines in *Figure 5-7* which shows the resulting flowfield from $\beta_1 = -10^\circ$, rpm = N1 and M = 0.05. The region of recirculation extends axially downstream and radially outwards from the hub. The streamlines show the approaching flow is mostly deflected over the rotor where it partially enters the recirculation region. Colour contours of axial velocity normalised with freestream velocity show the magnitude of the reverse flow area reaches the same level as the freestream. They also show deceleration of the flow as it approaches the rotor and, when combined with the streamlines, depict the extent of the reverse flow near the hub downstream of the blade row. Also included in *Figure 5-7* are contour lines of pressure coefficient (C_p) that show positive and very large negative C_p regions propagating upstream and downstream of the rotor respectively. This is in line with basic expectations for the following reason. Since the blades are experiencing negative incidence this means the upper-blade surfaces have become pressure surfaces and the lower-blade surfaces have become suction surfaces.

Figure 5-8 contains streamlines and contours for the front rotor at $\beta_1 = -10^\circ$, rpm = N1 and M = 0.2 to show the effect of increased Mach number on the flowfield.

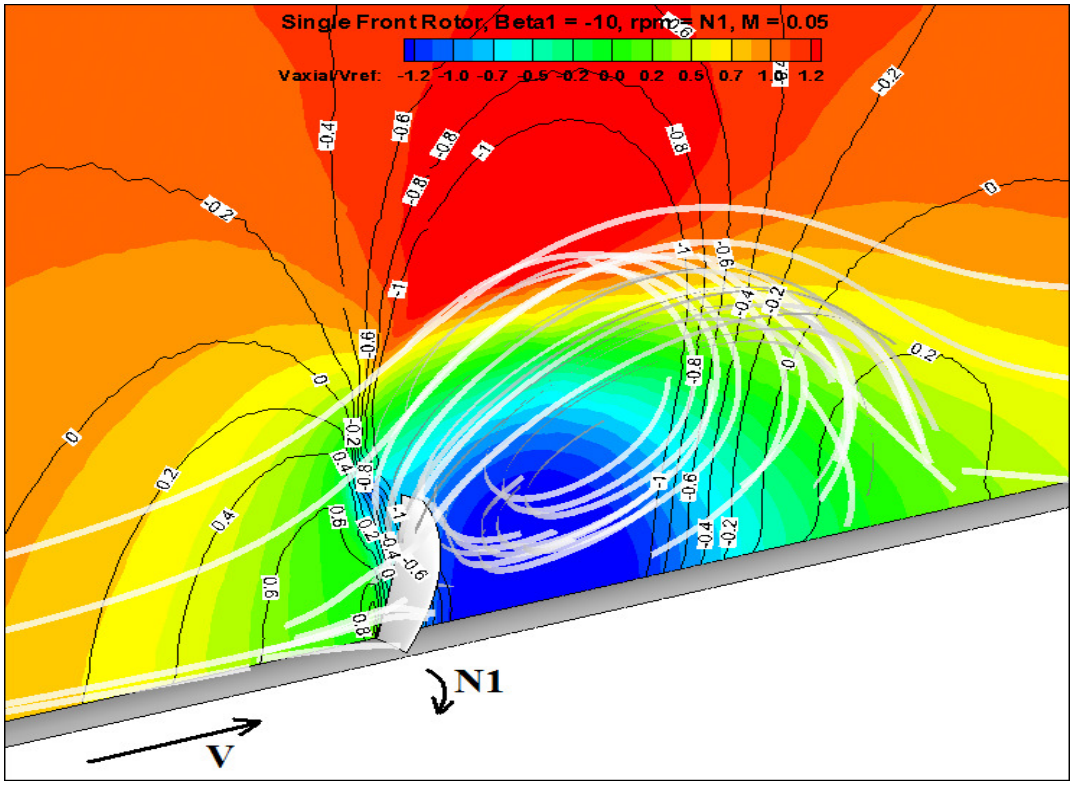

Figure 5-7 Singe front rotor contours and streamtraces for β= -10˚ and M = 0.05.

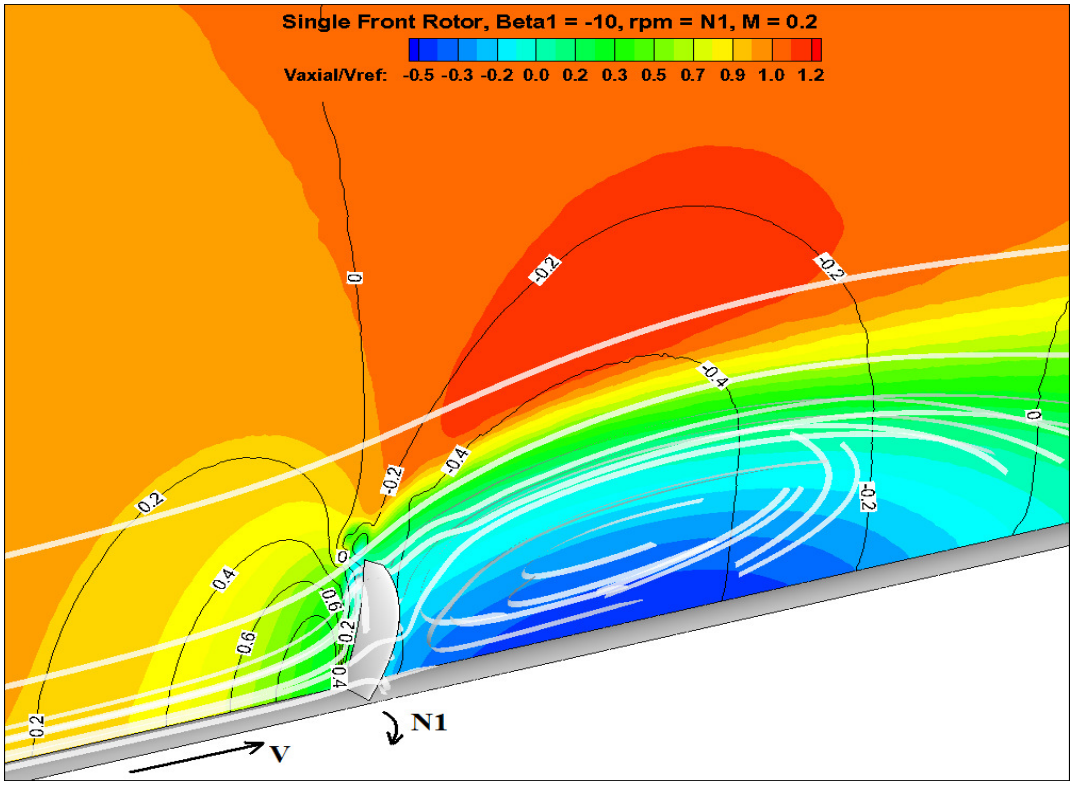

Figure 5-8 Singe front rotor contours and streamtraces for β= -10˚ and M = 0.2.

The most notable difference is illustrated *Figure 5-8* with 3D streamlines that depict the recirculation region shape. The axial downstream extent of reverse flow has been approximately doubled. The level of freestream radial deflection caused by the recirculation has been greatly reduced by the increased Mach number. The positive C_p region in front of the blade row has remained relatively the same when compared to the change in negative C_p downstream region, which has greatly reduced in magnitude and size. This may indicate that the blade rows ability to induce an opposing flow has diminished greatly when compared to M = 0.05 flowfield in *Figure 5-7*.

5.1.3 Summary of findings

- The rotor at positive pitch generates positive thrust and torque when the approaching flow creates a positive angle of incidence with the blade.

- As freestream velocity is increased and the blades experience a negative angle of incidence, the rotor at positive pitch generates negative thrust and negative torque.

- The rotor at negative pitch generates negative thrust and positive torque at all the cases investigated.

- The main flow feature observed, in all cases with either front or aft rotor at a reverse thrust setting (negative pitch), is a large recirculation region downstream of the blade row. This appears to be caused by the negative C_p region generated from the lower (suction) blade surfaces.

- The approaching flow is decelerated before entering the blade row. This is due to the adverse pressure gradient produced by the upper (pressure) blade surfaces.

- Increasing Mach number augments negative thrust production and elongates the shape of recirculation downstream. Less radial deflection of the freestream flow is observed upstream of, and entering, the blade row.

5.2 CROR frozen rotor CFD and experimental results

Experimental thrust and torque measurements for the individual rotors are presented in the following section for both contra-rotating pitch combinations of ($\beta_{1,2}$ = +30˚, -10˚) and ($\beta_{1,2}$ = -10˚, -20˚). They are plotted together with CFD calculated results which are the averages of the modelled blades multiplied by the full rotor blade number. All of the T and Q values have been normalised by datum values. The effects of varying main operating parameters are examined by observing performance and flowfield properties.

5.2.1 Initial analysis of $\beta_{1,2}$ = +30˚, -10˚

Thrust and torque performance

Individual rotor thrust and torque values for ($\beta_{1,2}$ = +30˚, -10˚) are presented in *Figure 5-9* and *Figure 5-10* respectively. Both figures each contain 4 plots relating to the 4 different rotor rpm combinations of the CFD test matrix. Focusing on the front rotor first, *Figure 5-9* (a) and (b) shows positive front rotor thrust (T_1) generated at the lowest Mach number (M). As the freestream speed is increased, T_1 is reduced to zero and begins to act in the opposite direction. Subsequent increases in M produce larger negative T_1 values. Similarly to T_1, front rotor torque (Q_1) is reduced from positive values to negative with increased M (*Figure 5-10* (a) and (b)). This behaviour was broadly expected based on a similar trend in the single rotor simulations of the front blade row (*Figure 5-1*).

The doubling of front rotor rpm (2xN1) is seen to cause a large increase in positive T_1 due to the extended local positive α experienced by the front rotor blades (*Figure 5-9* (c) and (d)). It also gives rise to larger negative T_2 values. This effect was anticipated since the front rotor exit conditions are generally taken as the inlet conditions for the aft rotor. If the flow is accelerated through the 1st blade row then the wind velocity (V) and local negative incidence angle of the 2nd blade row can be assumed to increase. With a larger T_1, the magnitude of negative T_2 was expected to increase. This is observed in plots (a) & (c) and plots (b) & (d) of *Figure 5-9*.

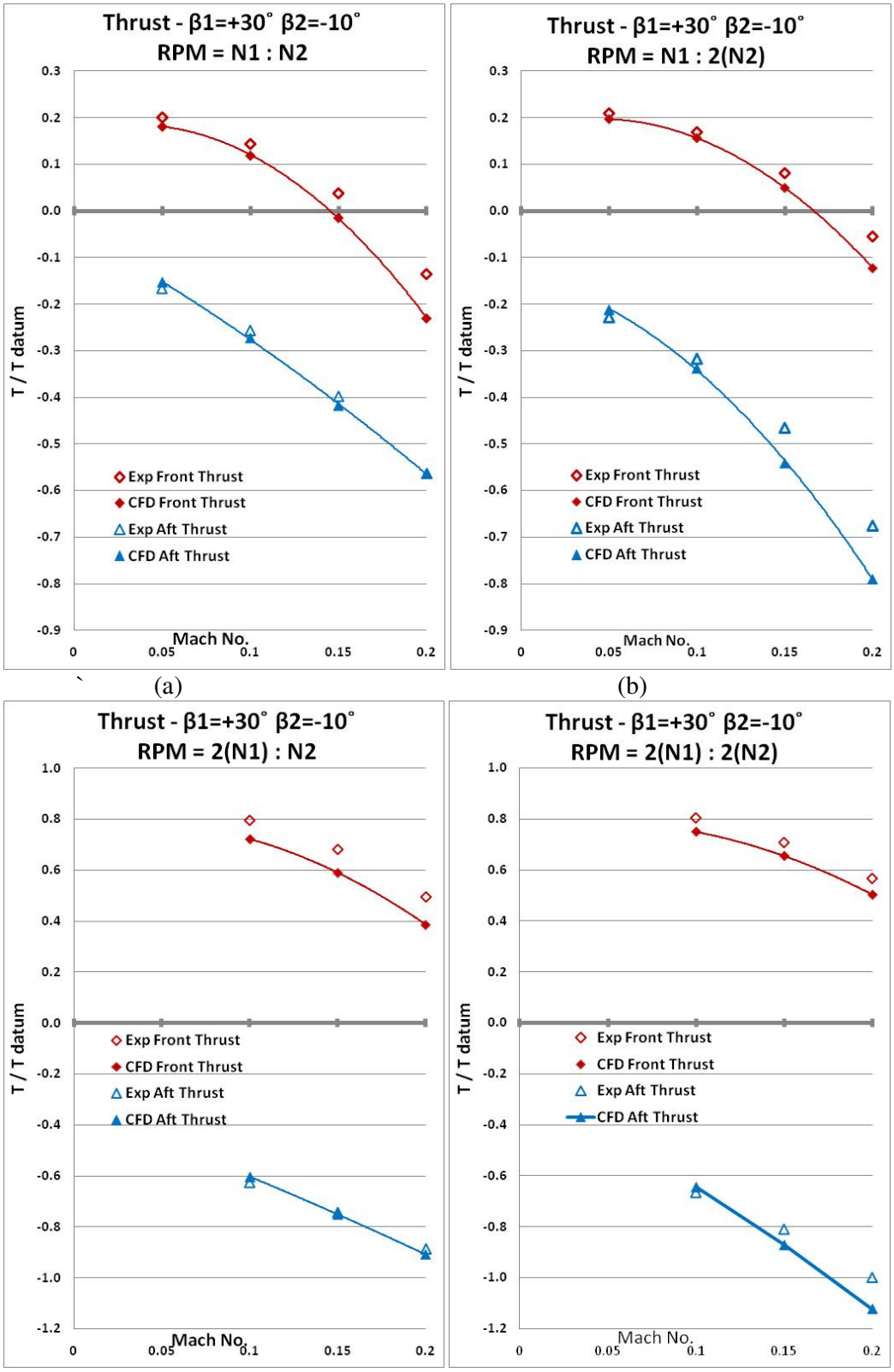

Figure 5-9 Experimental and CFD rotor thrust values for $\beta_{1,2}$ = +30˚, -10˚.

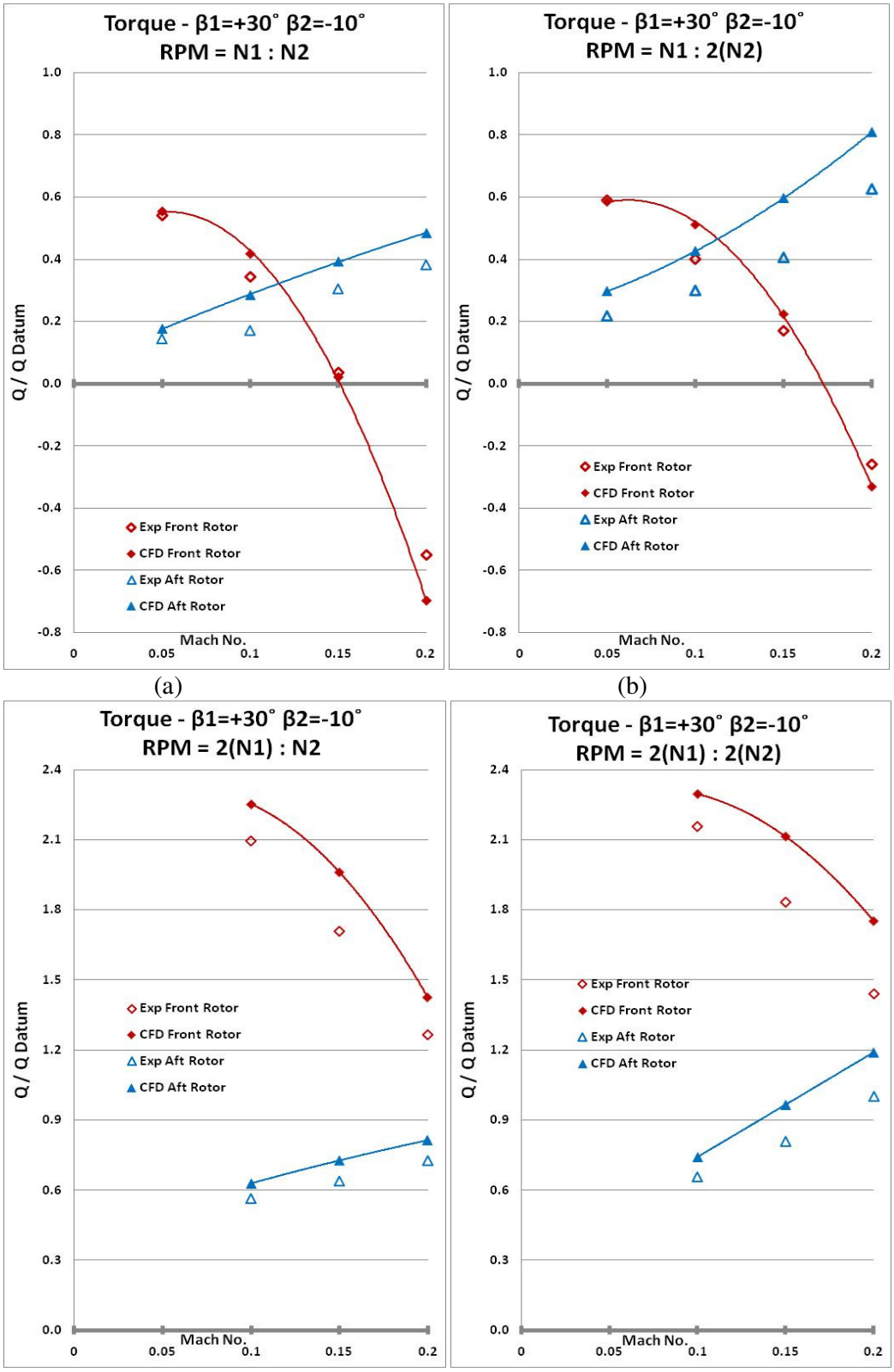

Figure 5-10 Experimental and CFD rotor torque values for $\beta_{1,2}$ = +30˚, -10˚.

Doubling the aft rpm (2xN2) was envisaged to provide a large increase in T_2 magnitude. This is surprisingly not the case upon examining *Figure 5-9* (b) and (d). At M = 0.05 there appears to be a slight increase in T_2 magnitude. This increase is augmented by higher freestream speeds.

Upon examination of the thrust trends for all the cases at this particular pitch setting ($\beta_{1,2}$ = +30˚, -10˚), the torque characteristics were broadly in line with anticipated behaviour based on earlier simplified theory.

Flowfield Assessment

To start this initial assessment of the flowfield generated by contra-rotation at $\beta_{1,2}$ = +30˚, -10˚, the datum case of M = 0.1 and rpm = N1:N2 is chosen to illustrate the main flow features (*Figure 5-11*). Through the use of 3D streamlines, *Figure 5-11* clearly depicts a very large region of recirculation downstream of the aft rotor. This is a dominant feature in all the CROR CFD test cases at this pitch setting ($\beta_{1,2}$ = +30˚, -10). It is influenced by changes in M or rotor rpm, which will be shown later in this chapter, but still remains the principle flowfield feature of this reverse thrust investigation.

Part of the flow is shown to be deflected radially outwards and over the aft rotor in *Figure 5-11*. Since the front rotor generates positive thrust at this test case (*Figure 5-9*) this indicates the flow passes through the front blade row before either passing through the aft rotor or deflecting radially outwards. Colour contours of axial velocity normalised with freestream show the recirculation region with a large area of reverse flow near the hub downstream of the aft rotor. Also shown is a deceleration of the flow as it approaches the front rotor. Lines of constant C_p are also shown in *Figure 5-11* and depict a region of high C_p and low C_p propagating upstream and downstream of the aft rotor respectively.

It appears that the main flowfield features in *Figure 5-11*, deduced from streamlines and contours, are similar to those of the single front rotor at negative pitch with same rpm of N1 (*Figure 5-7* and *Figure 5-8*).. Further sections explore the effects of rpm, Mach number and the addition of a 2nd rotor on these flowfield features.

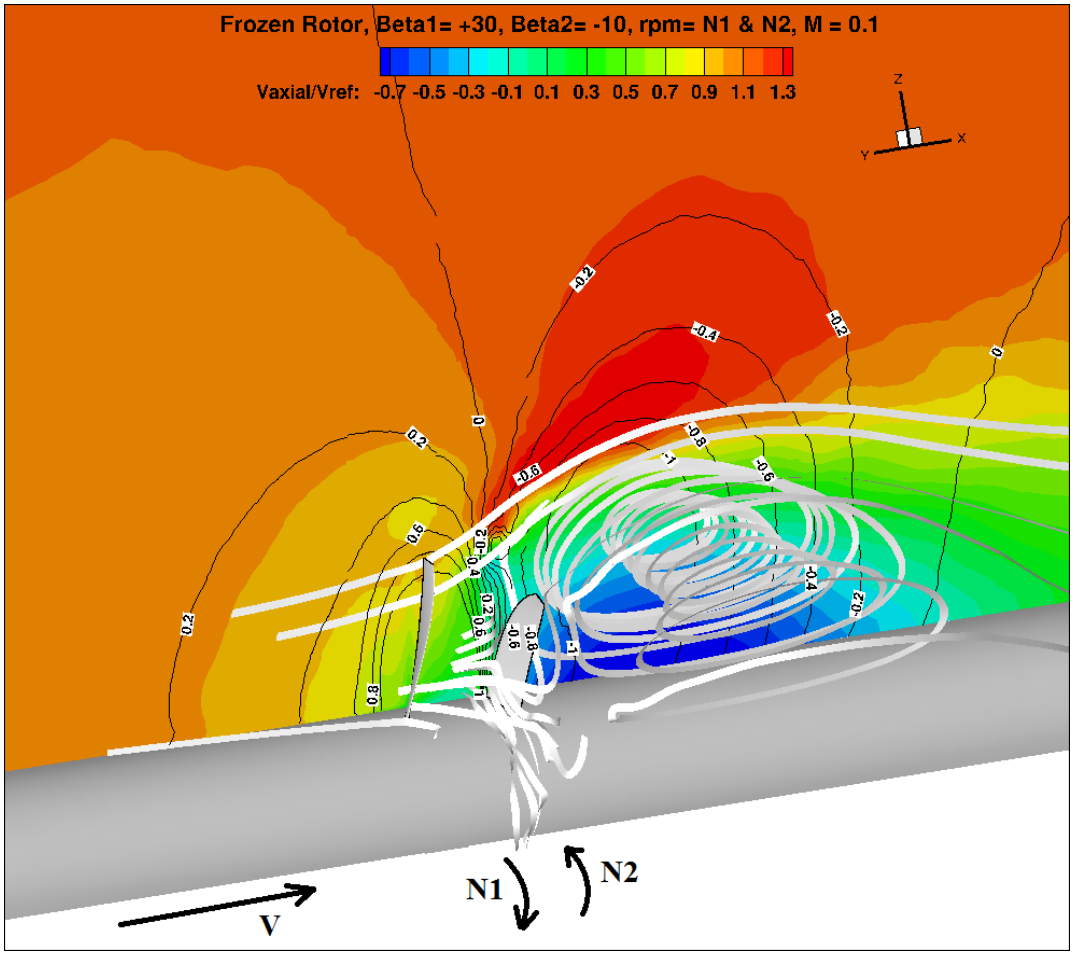

Figure 5-11 CROR contours and streamtraces for $\beta_{1,2}$ = +30˚, -10˚, rpm = N1:N2 and M = 0.1.

CFD validation

Focusing on the front rotor thrust first, it can be seen in *Figure 5-9* for each rpm combination that the effect of increasing M has been reproduced quite well with the predicted T_1 distributions in very good agreement with experimental data. All the CFD results show that T_1 reduces in positive magnitude as M is increased. There is however a general under-prediction of T_1 values when the front rotor is producing positive thrust (*Figure 5-9* (a)-(d)). The level of under-prediction grows with increased M. In *Figure 5-9* (a) and (b) this is true up to the point where T_1 changes direction and becomes negative. When producing negative thrust, the CFD over-predicts the negative magnitude of T_1. This over-prediction also grows with higher M flows.

The front rotor CFD torque results in ***Figure 5-10*** (a) to (d) correspond well to CFD T_1 trends. Any difference against experimental Q_1 values appear to tie in with the discrepancies in observed in the predicted T_1 previously identified.

Aft thrust (T_2) predictions show good agreement with the experimental data for all the test cases with the effect of M being predicted well. An element of over-prediction is shown in *Figure 5-9* (b) and (d) at higher M cases when the aft rpm (N2) is doubled to 2(N2). Aft rotor predicted torque (Q_2) results in *Figure 5-10* (a) to (d) approach the experimental Q_2 values quite well. They also conform well to the experimental trends for varying rpm and M. It is evident from the data however that the predicted Q_2 results are all lower than the experimental data. A reason for this error is not obvious since the predicted T_2 results do not show the same scope of under-prediction in the thrust plots.

5.2.2 Rotor interaction for $\beta_{1,2} = +30^{\circ}, -10^{\circ}$

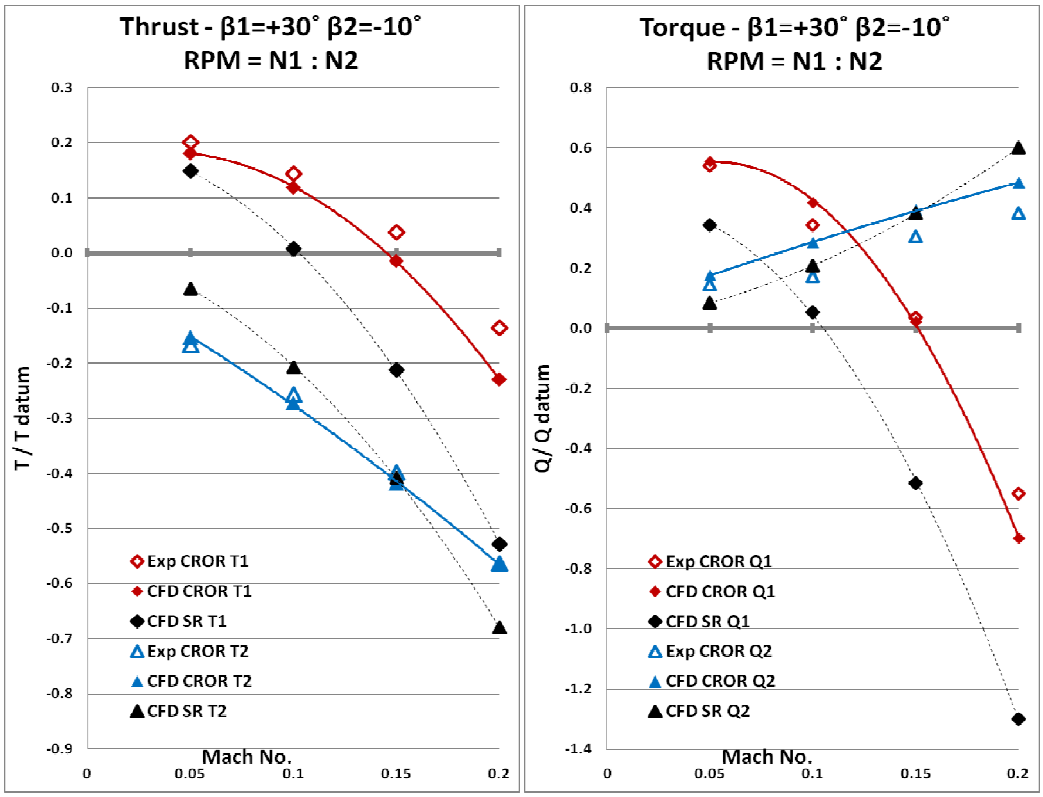

(a) (b)

Figure 5-12 Single rotor and contra-rotating T and Q results for $\beta_{1,2} = +30^{\circ}, -10^{\circ}$ and rpm N1:N2.

Single rotor CFD results can now be used with contra-rotation experimental and CFD results to identify possible interaction effects of one rotor on the others performance. To this end the contra-rotating open rotor (CROR) T and Q results, for $\beta_{1,2} = +30^{\circ}, -10^{\circ}$ and rpm = N1:N2, have been plotted with single rotor (SR) CFD results for the same operating conditions (see *Figure 5-12*). The SR front rotor results are those obtained with the hybrid grid from *Figure 5-1*.

It is observed in *Figure 5-12* that the introduction of the downstream blade row causes the front rotor to produce larger positive T_1. As a consequence the Mach number that results in a transition from positive T_1 to negative T_1 is increased, and the magnitude of negative T_1 thereafter is reduced. The cause of this aft rotor effect on the front rotor cannot be determined from thrust and torque values alone.

The M = 0.2 case from *Figure 5-12* produced the greatest difference in T and Q for SR and CROR. For this case, meridional contours of C_p in *Figure 5-13* (a) show propagation upstream of the aft rotor and though the front rotor. This is also illustrated in an unwrapped circumferential surface in *Figure 5-13* (b) of C_p contours taken at 70% front rotor blade span. These spanwise contours show the front rotor operating in the high C_p region caused by the aft rotor. To prove this point, contours of the single aft rotor at the same spanwise height, at same operating conditions, show the high C_p region before addition of the front rotor. The freestream flow approaching the front rotor is slowed by this adverse pressure gradient. This results in a smaller negative incidence angle, and hence smaller negative T_1, for the front rotor at this M = 0.2 case.

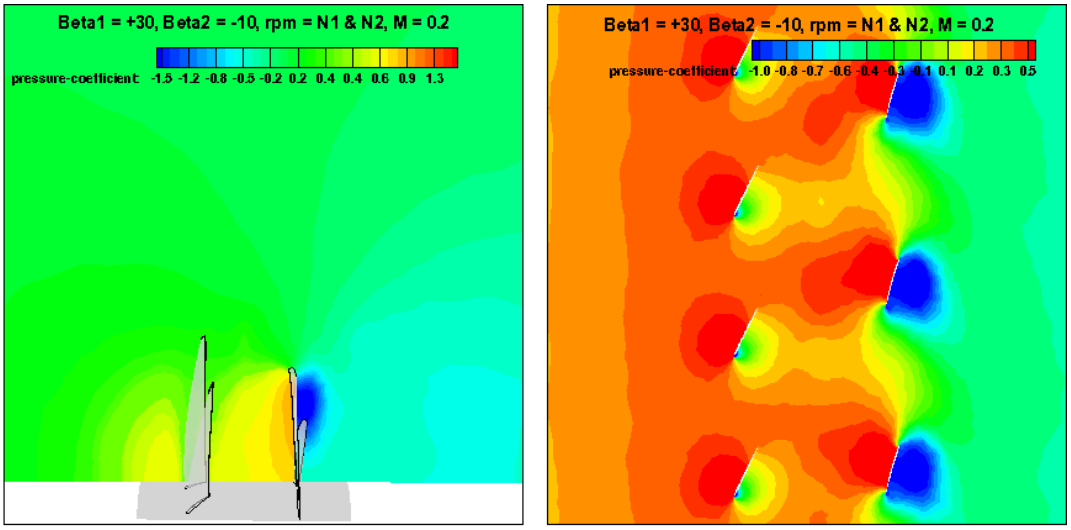

(a) Meridional contours

(b) Circumferential contours at 70% front rotor blade span.

Figure 5-13 C_P contours of CROR at $\beta_{1,2}$ = +30˚, -10˚ and rpm N1:N2.

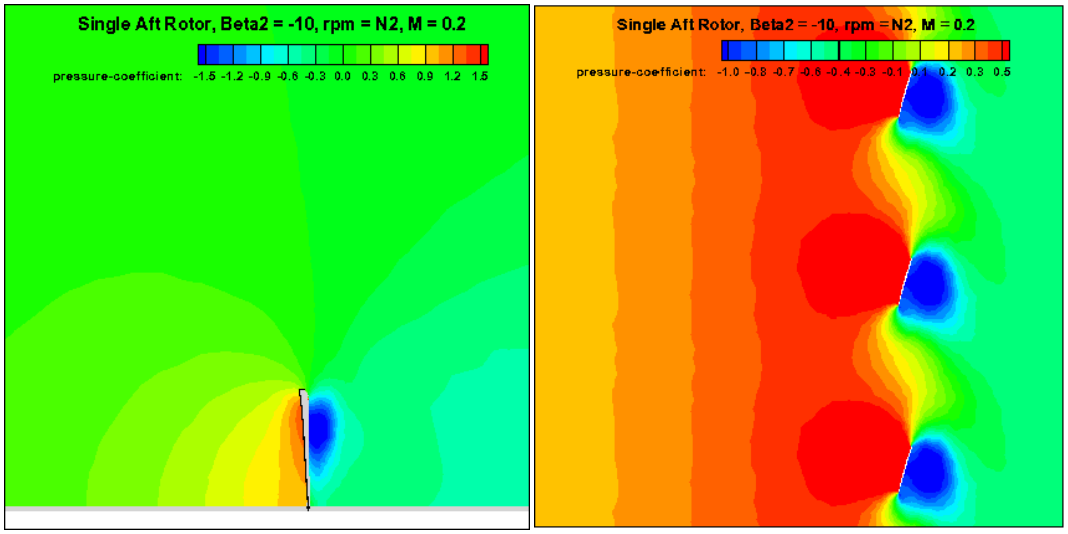

(a) Meridional contours

(b) Circumferential contours at 70% front rotor blade span.

Figure 5-14 C_P contours of SR aft rotor at β_2 = -10˚ and rpm N2.

The front rotor effect on the aft rotor, as observed from T and Q results in *Figure 5-12*, is shown to increase negative magnitude of T_2 at lower Mach numbers and decrease negative magnitude of T_2 at M=0.2. This is logical since the front rotor generates positive thrust at lower M, which increases the axial velocity of the aft rotor inlet conditions. When the front rotor is producing negative thrust, the aft inlet axial velocity is smaller than that experienced without the front rotor.

This front rotor effect on aft rotor performance is further highlighted by examining the T and Q results for M = 0.15 in *Figure 5-12*. This case shows the CROR front rotor generating nominal thrust. As a result of this, there is negligible difference between the thrust generated from SR aft rotor and CROR aft rotor.

5.2.3 Mach number variation for β1,2 = +30˚, -10˚

To examine the effect of Mach number on the flowfield of contra-rotating open rotors at $\beta_{1,2}$ =+30˚,-10˚ and rpm= N1:N2, contours of axial velocity normalised with freestream velocity are shown in *Figure 5-15* for M = 0.05 and M = 0.2 cases. At the lower Mach number *Figure 5-15* (a) shows reverse flow downstream of the aft rotor with its extent highlighted by the dashed line representing velocity of 0. The dashed line also indicates

reverse flow activity in between the rotors. The outboard portion of the front rotor is shown to accelerate the flow. This can also be seen in *Figure 5-15*(e) which shows the axial velocity at 70% front rotor bladespan. The dashed lines in *Figure 5-15*(c) show reverse flow upstream of the aft rotor at 20% front rotor bladespan. *Figure 5-15*(b) illustrates that at M=0.2 the front rotor is no longer generating positive thrust and that the flow is decelerating as it approaches the front blade row. The extent of reverse flow downstream of aft rotor is increased and there is nominal reverse flow activity in between the rotors. *Figure 5-15*(b) and (d) illustrate the flow deceleration entering the front rotor and also the diminished reverse flow capacity through the aft rotor.

Contours of C_p on the same meridional plane are given in *Figure 5-16*(a) and (b) for M = 0.05 and M = 0.2 respectively. They both show negative C_p downstream of the aft rotor. However, at M=0.05 there is a high C_p region in between the rotors which appears to be confined by both rotors contributing to it in opposing directions. For M=0.2 it is observed that both rotors are now generating an adverse pressure gradient for the freestream flow. This ties in with the polarity change in T_1 as M is increased. Looking at the circumferential contours for M = 0.05 and 0.2 in *Figure 5-16*(c)(e) and *Figure 5-16*(d)(f) respectively, the change in front rotor pressure and suction surfaces can be seen. For M=0.05 the front blade upper surface is the suction surface indicating a positive incidence angle and positive thrust. For M=0.2 *Figure 5-16*(d)(f) shows the upper surface is now the pressure surface.

This polarity change in front rotor T and Q as M is increased can be further illustrated with integrated pressure force blade distributions. *Figure 5-17* presents the T and Q average blade distributions for front and aft rotor. For front rotor blade T and Q distribution *Figure 5-17* (a) and (c) show the Mach number effect. The M=0.15 case highlights a notable finding where the front rotor blades are loaded in both axial directions. The inboard section is generating an amount of positive T_1 and Q_1, and the outboard is producing negative T_1 and Q_1. This may pose an unexpected need for further blade structural analysis at these operating conditions, given the resulting shear forces and bending moments. For the aft rotor, *Figure 5-17* (b) and (d) shows increased freestream Mach number augmented negative T_2 and positive Q_2 as expected.

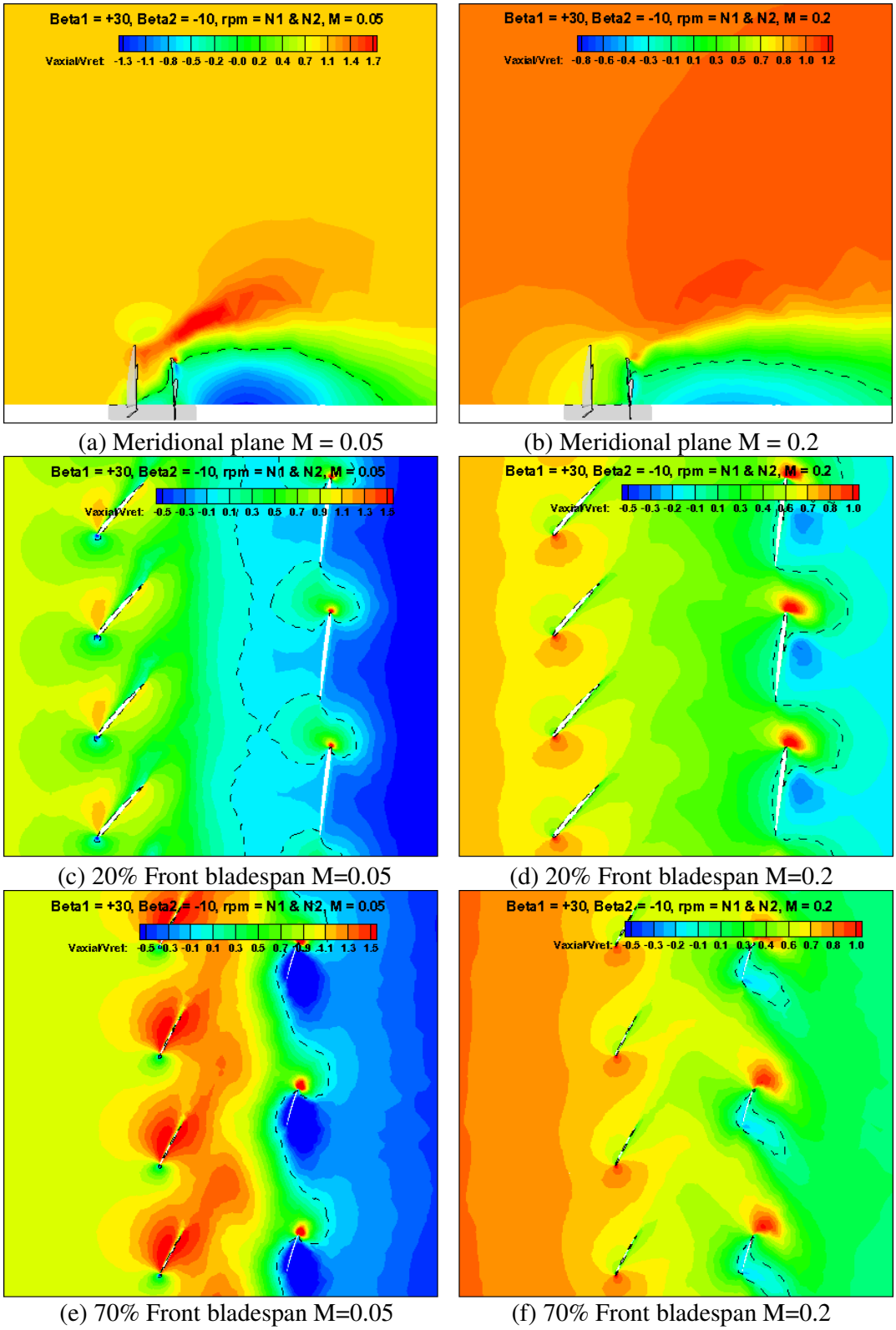

(a) Meridional plane M = 0.05

(b) Meridional plane M = 0.2

(c) 20% Front bladespan M=0.05

(d) 20% Front bladespan M=0.2

(e) 70% Front bladespan M=0.05

(f) 70% Front bladespan M=0.2

Figure 5-15 Normalised axial velocity contours for CROR at $\beta_{1,2}$ =+30˚,-10˚ and rpm= N1:N2.

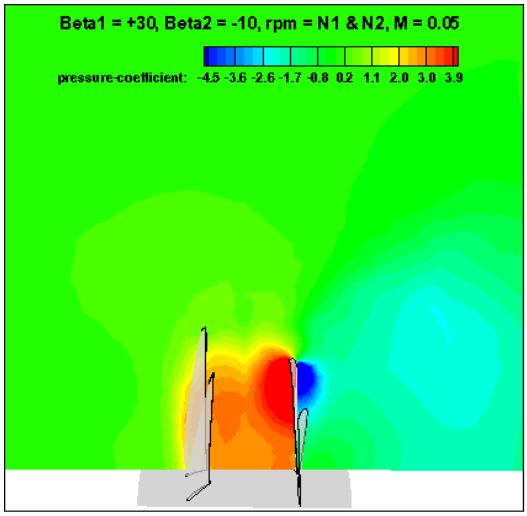

(a) Meridional plane M = 0.05

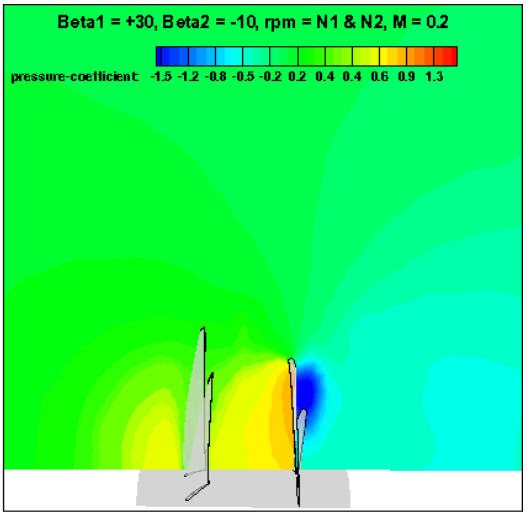

(b) Meridional plane M = 0.2

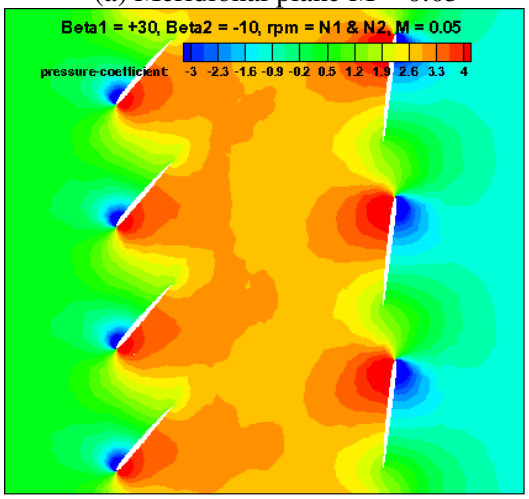

(c) 20% Front bladespan M=0.05

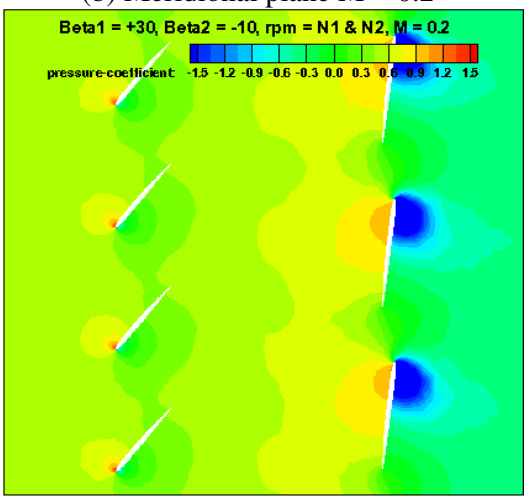

(d) 20% Front bladespan M=0.2

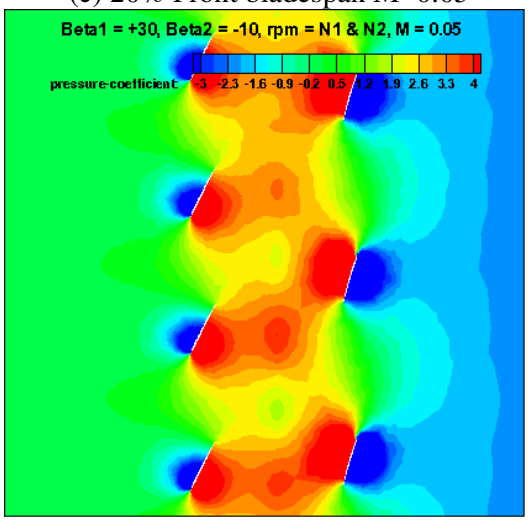

(e) 70% Front bladespan M=0.05

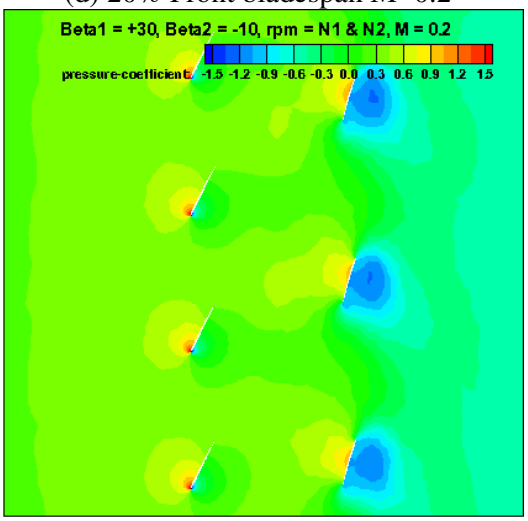

(f) 70% Front bladespan M=0.2

Figure 5-16 C_p contours for CROR at $\beta_{1,2}$ =+30˚,-10˚ and rpm= N1:N2.

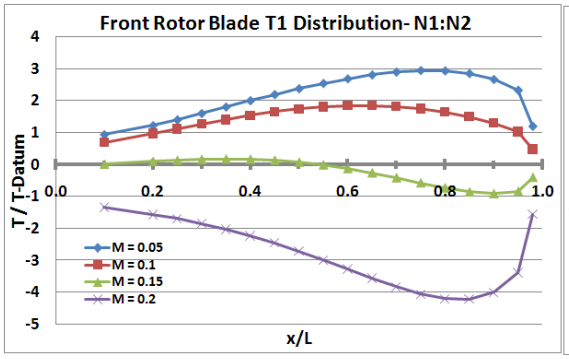

(a) front T_1 blade distribution

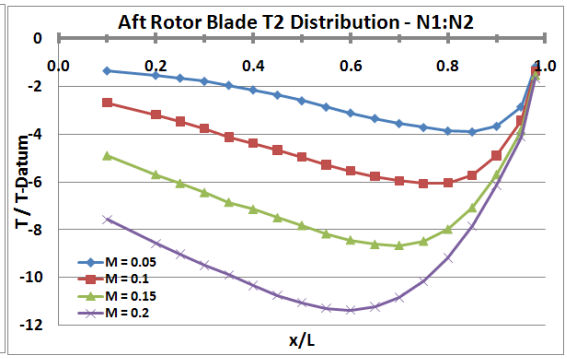

(b) aft T_2 blade distribution

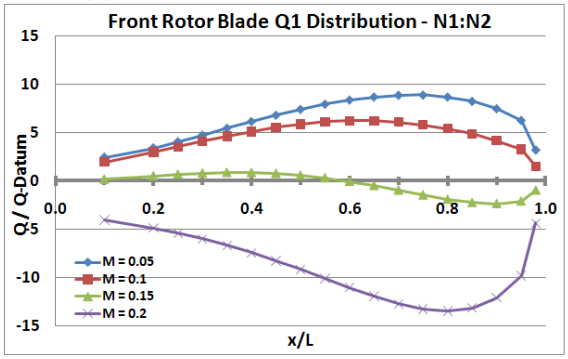

(c) front Q_1 blade distribution

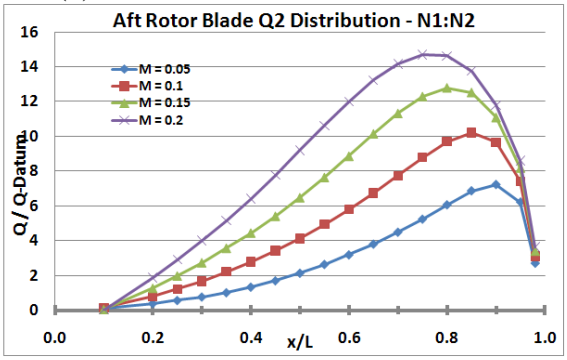

(d) aft Q_2 blade distribution

Figure 5-17 Average blade distribution from pressure forces for CROR at $\beta_{1,2}$ =+30˚,-10˚, rpm = N1:N2.

5.2.4 Front rotor rpm variation for $\beta_{1,2} = +30^{\circ}, -10^{\circ}$

The effect of front rpm on rotor performance has already been identified in the initial analysis however it is better illustrated with experimental T and Q results in *Figure 5-18* for a constant aft rotor rpm of N2. Focusing on front rotor first, *Figure 5-18* (a) shows a very large increase in positive T_1 when N1 is doubled. This is expected since increasing the front blade row speed causes an increase in positive incidence angle. As the freestream velocity is raised, the positive incidence and hence T_1 is decreased but not to a point where transition from positive to negative thrust generation occurs. The substantial jump in negative thrust production from the aft rotor (T_2) when front rpm is doubled (*Figure 5-18* (a)) was also expected. Larger positive T_1 means higher wind velocity (V) entering the aft rotor which increases the negative incidence angle for the aft blade row. The torque characteristics in *Figure 5-18* (b) are in agreement with the thrust characteristics. With CFD calculations it is now possible to examine the effect of front rpm on the CROR reverse thrust flowfield.

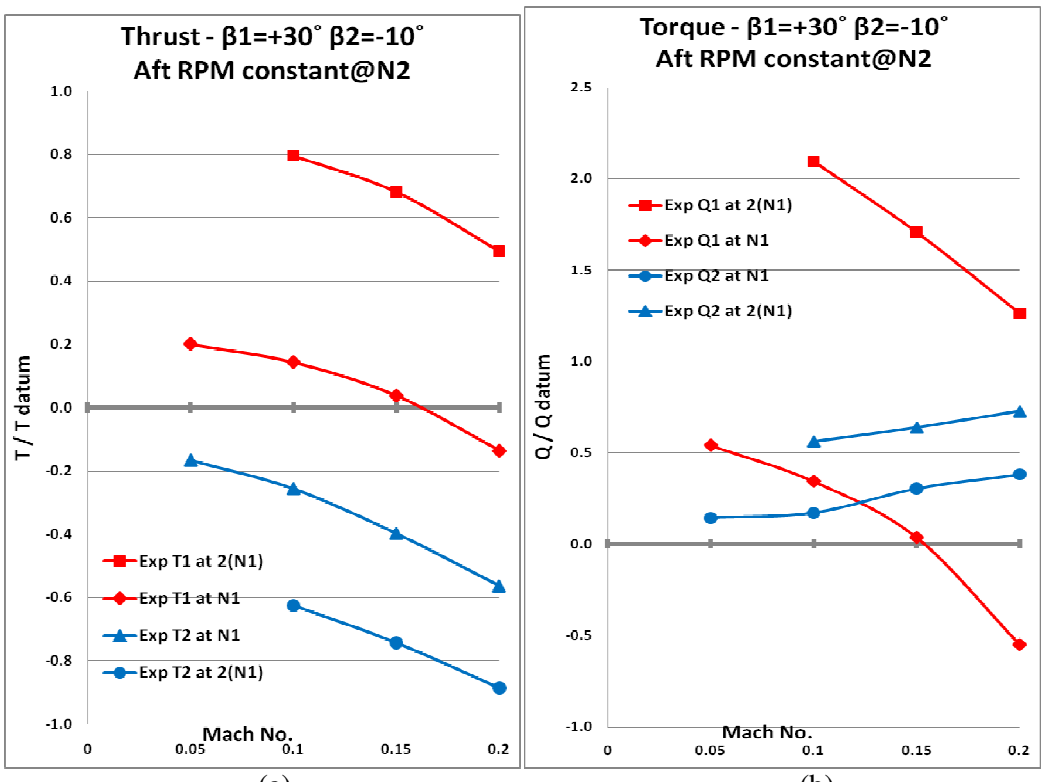

(a) (b)

Figure 5-18 Experimental rotor T and Q values for $\beta_{1,2} = +30^{\circ}, -10^{\circ}$ with constant aft rotor rpm N2.

Main flowfield features for M = 0.1, with front rpm doubled to 2(N1), are presented in *Figure 5-19*. As stated before, the recirculation region downstream of the aft rotor is the main feature present in all cases for this reverse thrust setting of $\beta_{1,2}$ = +30˚, -10˚. Streamlines in *Figure 5-19* show this recirculation, however the larger magnitude of T_1 appears to have confined it closer inboard towards the hub, when compared to *Figure 5-11* (for front rpm N1). Colour contours of axial velocity normalised with freestream velocity show the accelerated flow through the front blade row and its slight deflection over the reverse flow area (*Figure 5-19*). They also depict the strength of the reverse flow area reaching close to M = 0.1 in the opposite direction to the freestream flow. C_p lines show high pressure between the rotors along with low pressure propagating downstream of the aft rotor. However now there is very little high C_p propagation upstream of front rotor like that in *Figure 5-11* (for front rpm N1). This may explain why there is nominal deceleration of the freestream approaching the front rotor. Increased front rpm may reduce or prevent the aft rotor effect on the front rotor. This can be explored with further velocity and C_p contours at various locations in the flowfield.

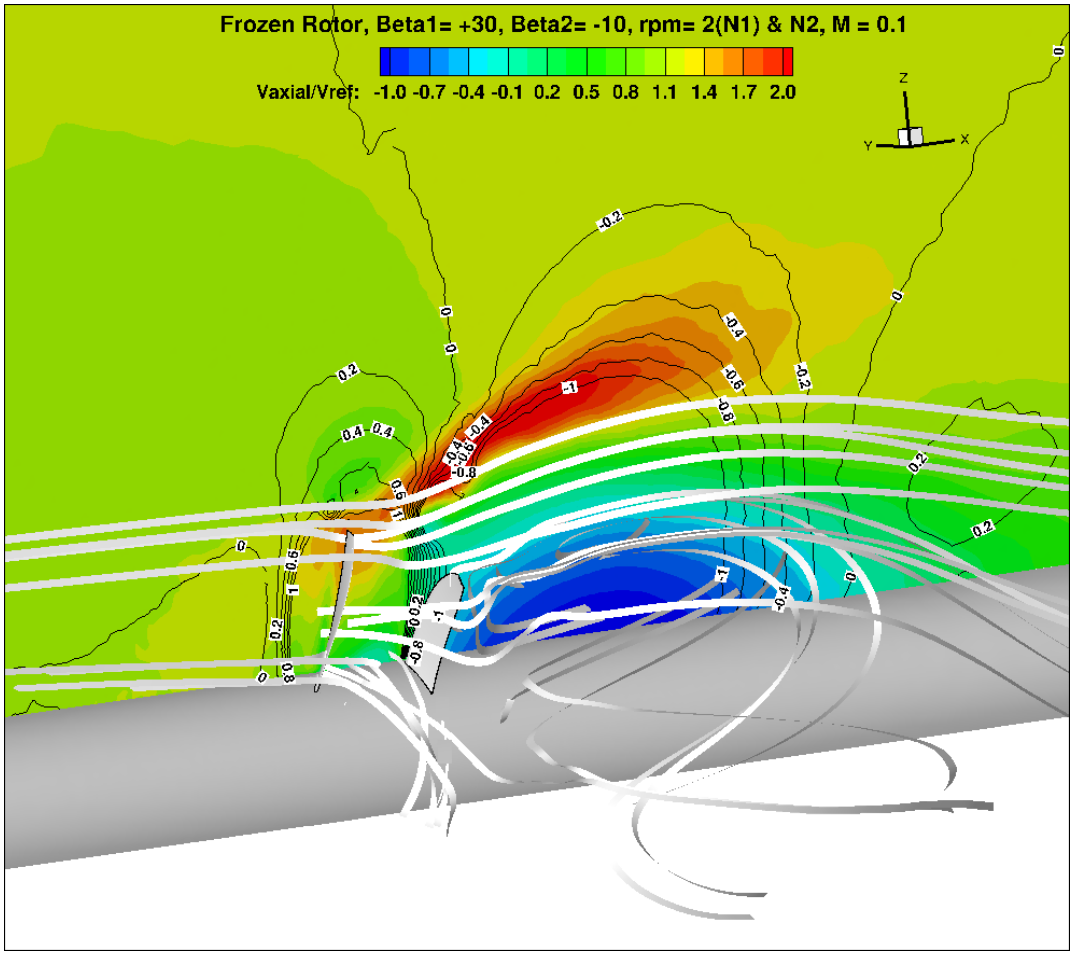

Figure 5-19 CROR contours and streamtraces for $\beta_{1,2}$ = +30˚, -10˚, rpm = 2(N1):N2 and M = 0.1.

Figure 5-20 (a) and (b) show a meridional view of normalised axial velocity contours for M= 0.1 and M= 0.2 respectively. The dashed lines represent 0 m/s velocity. They show that M = 0.1 results in minimal freestream deceleration approaching the front rotor. However, increasing M to 0.2 re-introduces the upstream deceleration. Upon examining circumferential contours at 20% and 70% front rotor bladespan in *Figure 5-20* (c) and (e) respectively, M = 0.1 freestream enters the front rotor but only the outboard parts of the front rotor blades increase the flow axial velocity. When M = 0.2 *Figure 5-20* (d) and (f) show the extent of deceleration on the flow entering the front blade row. They also show negligible axial velocity increment generated by the front rotor. This is in spite of large positive thrust production from the front rotor at these operating conditions (*Figure 5-9*).

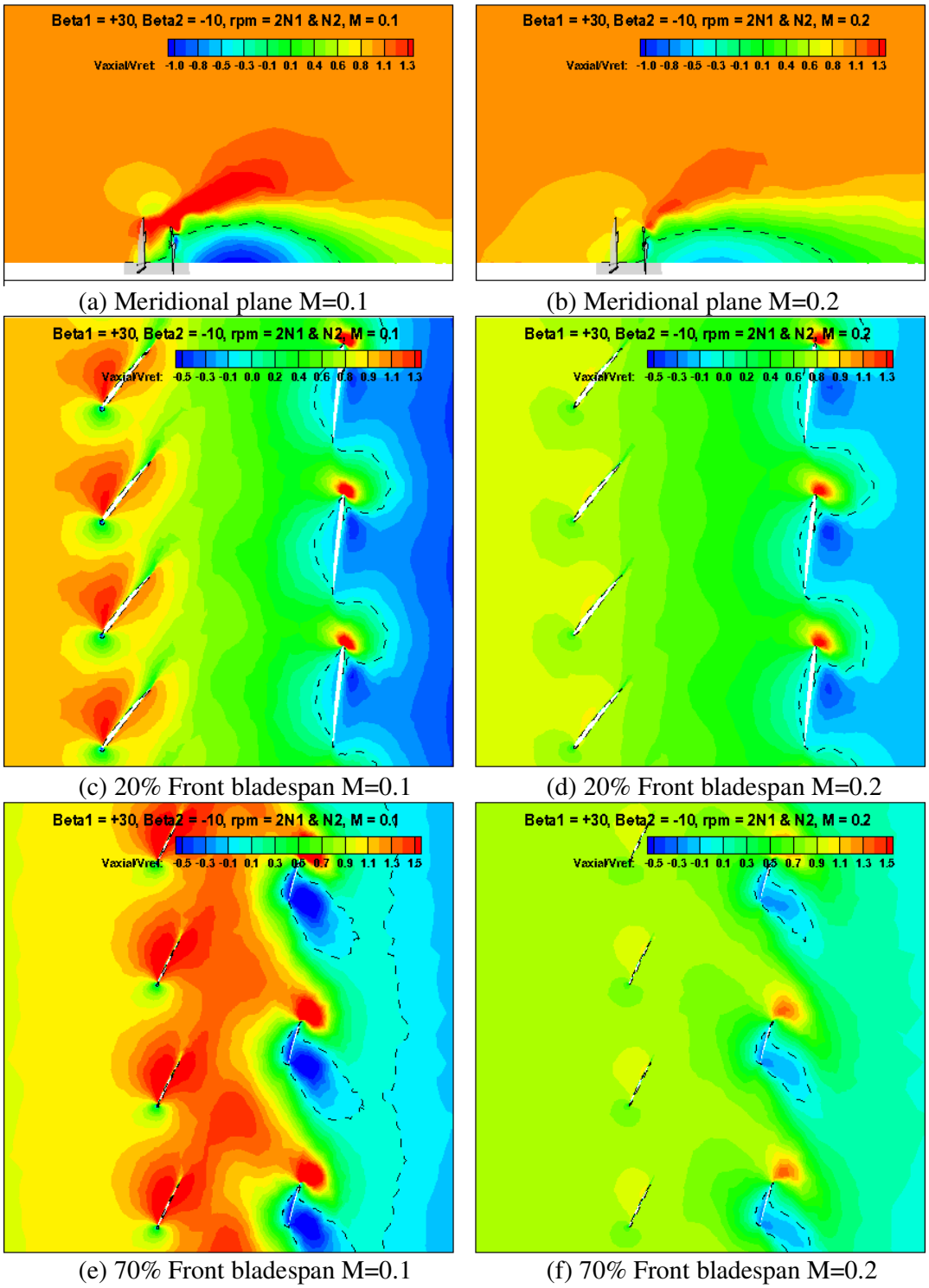

(a) Meridional plane M=0.1 (b) Meridional plane M=0.2

(c) 20% Front bladespan M=0.1 (d) 20% Front bladespan M=0.2

(e) 70% Front bladespan M=0.1 (f) 70% Front bladespan M=0.2

Figure 5-20 Normalised axial velocity contours for CROR at $\beta_{1,2}$ =+30˚,-10˚, rpm = 2(N1):N2

Figure 5-21 (a) and (b) show a meridional view of C_p contours for M = 0.1 and M = 0.2 respectively. *Figure 5-21* (c)(e) and (d)(f) are circumferential C_p contours for M = 0.1 and M = 0.2 respectively. What is evident from *Figure 5-21* (a),(c) and (e) is that no pressure increase propagates upstream of front rotor which explains why there is no axial flow deceleration approaching front blade row. Focusing on the contours around the airfoil sections of both front and aft rotors, *Figure 5-21* (c) and (e) illustrate that at M = 0.1 both rotors are contributing to the high pressure region in between the rotors. The front rpm is high enough to generate large positive thrust at β_1= +30˚. Both rotors are confining the high pressure region between the rotors because they are contributing to it from opposing directions.

Figure 5-21 (d) and (f) show that at M=0.2, the blade T and Q distribution of the front rotor is reduced, based on C_p distribution around the front blade airfoil sections. Despite the high front rpm, the front rotor contribution to the high C_p region between the rotors is greatly reduced at higher freestream velocities. As a consequence of this, *Figure 5-21* (d) and (f) show the pressure increase from the aft rotor propagate upstream through the front rotor. This exacerbates the loss in front rotor performance by causing a deceleration of the approaching freestream flow (*Figure 5-20* (b), (d) and (f)).

Figure 5-22 contains the average blade T and Q distribution of the front and aft rotors at $\beta_{1,2}$ =+30˚,-10˚ and rpm = 2(N1):N2. This plot shows the large drop in front rotor blade thrust (*Figure 5-22* (a)) and aft rotor blade thrust increase (*Figure 5-22* (b)) as M is increased. It also confirms the outboard section of the front rotor generates the majority of positive thrust at the lower Mach numbers

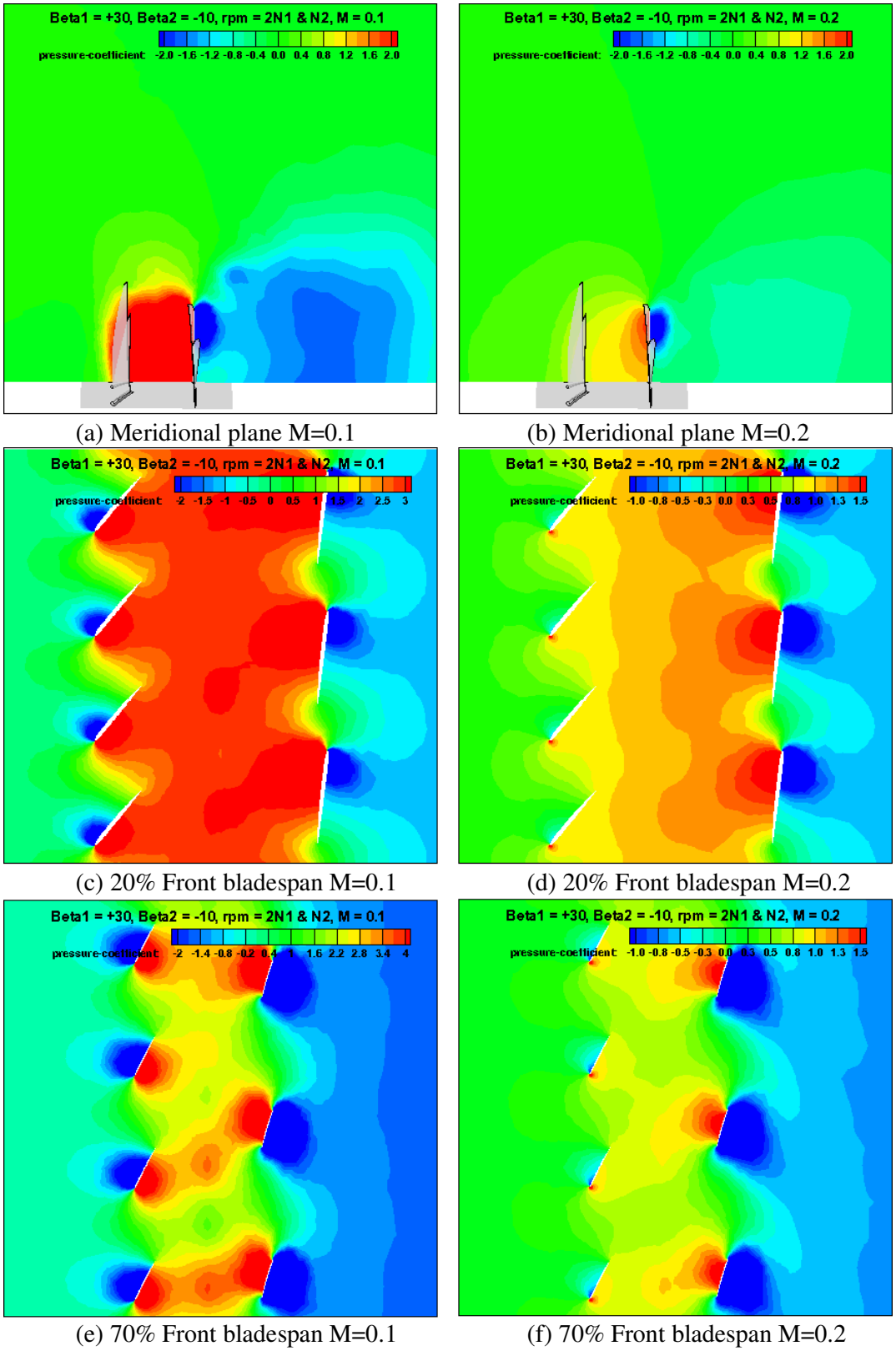

(a) Meridional plane M=0.1

(b) Meridional plane M=0.2

(c) 20% Front bladespan M=0.1

(d) 20% Front bladespan M=0.2

(e) 70% Front bladespan M=0.1

(f) 70% Front bladespan M=0.2

Figure 5-21 C_p contours for CROR at $\beta_{1,2}$ =+30˚,-10˚, rpm = 2(N1):N2.

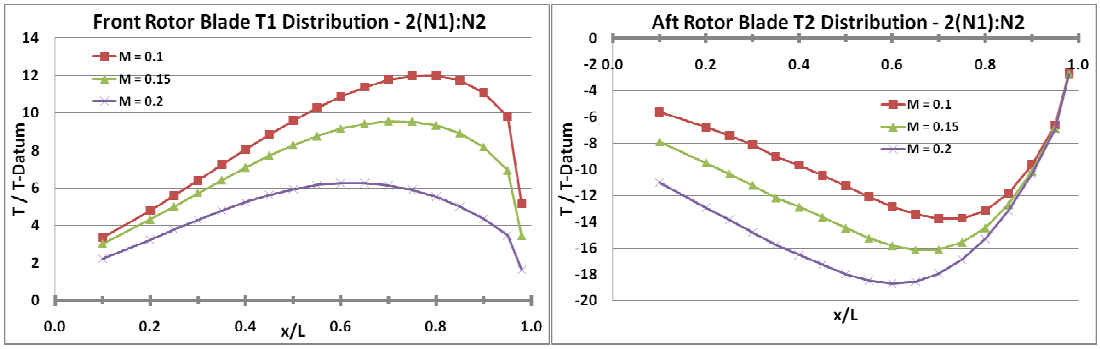

(a) front T_1 blade distribution (b) aft T_2 blade distribution

Figure 5-22 Average blade distribution from pressure forces for CROR at $\beta_{1,2}$ =+30˚,-10˚, rpm = 2(N1):N2.

5.2.5 Aft rotor rpm variation for $\beta_{1,2}$ = +30˚, -10˚

The effect of aft rpm on rotor performance has already been identified in the initial analysis however, it is better illustrated with experimental T and Q results in *Figure 5-23* for a constant front rotor rpm of N1. Focusing on front rotor first, *Figure 5-23* (a) shows that at M = 0.05 there is a slight increase in positive T_1 magnitude from doubling the aft rpm. This positive T_1 increase is augmented by higher freestream Mach numbers which delays the transition from positive to negative T_1. Subsequently at M = 0.2 the higher aft rpm of 2(N2) results in a smaller negative T_1 than that measured at N2.

A substantial increase in aft rotor negative thrust is expected from doubling of the aft rpm but looking at T_2 results in *Figure 5-23* (a) this is not the case. There is a modest increase in negative T_2 at M = 0.05, however this increase is mostly unaffected by higher freestream velocities. The aft torque results (Q_2) in *Figure 5-23* (b) do not correspond to T_2 trends as good as Q_1 follows the T_1 trends. This may indicate an area of unexpected behaviour or may just be a discrepancy in the experimental results. Numerical simulations have allowed examination of flowfield properties to further investigate the aft rotor rpm effects.

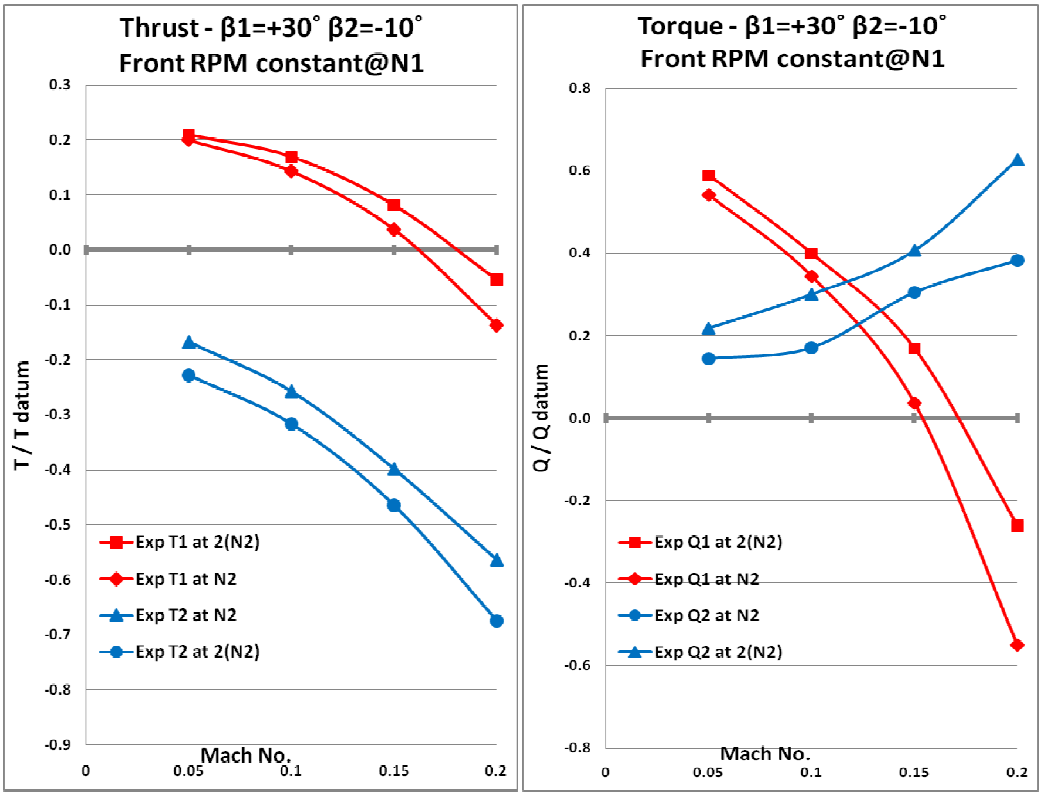

(a) *(b)*

Figure 5-23 Experimental rotor T and Q values for $\beta_{1,2}$ = +30˚, -10˚ with constant front rotor rpm N1.

The effect of aft rotor rpm on axial velocity is examined firstly on an example case of $\beta_{1,2}$ = +30˚, -10˚ and M = 0.1. *Figure 5-24* (a) and (b) are meridional views of normalised axial velocity at rpm combinations of N1:N2 and N1:2(N2) respectively with the dashed line representing 0 m/s. They show an increase in velocity of the reverse flow region. This increase in recirculation strength has led to a reduction in reverse flow extent downstream of the aft blade row. *Figure 5-24* (c)(d) and (e)(f) present circumferential axial velocity contours taken at radial distances of 20% and 70% front rotor bladespan respectively. *Figure 5-24* (d) shows that doubling aft rpm causes reverse flow to propagate upstream through the aft blade row even at a radial distance close to the hub (20% L_1). At 70% front rotor bladespan *Figure 5-24* (f) shows stronger reverse flow approaching, and propagating through, the aft rotor than contours of rpm N1:N2 in *Figure 5-24* (e). What is also evident from *Figure 5-24* (d)(f) is that higher aft rpm has resulted in further deceleration of the flow approaching the front rotor. Contours of C_p are now illustrated in *Figure 5-25* to explore the causes of these axial velocity changes.

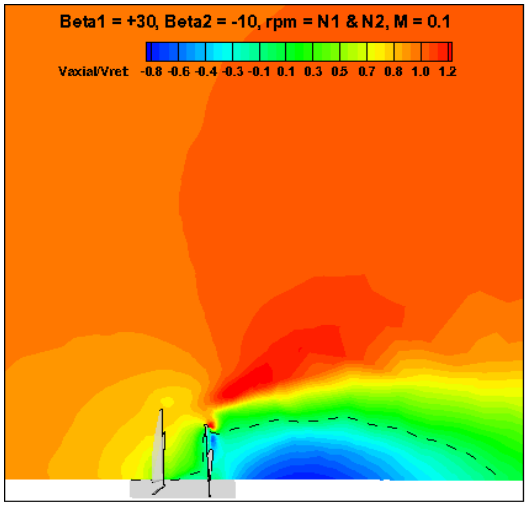

(a) Meridional plane N1:N2

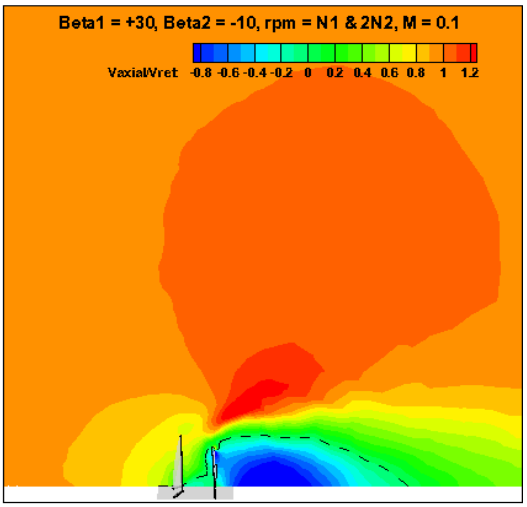

(b) Meridional plane N1:2(N2)

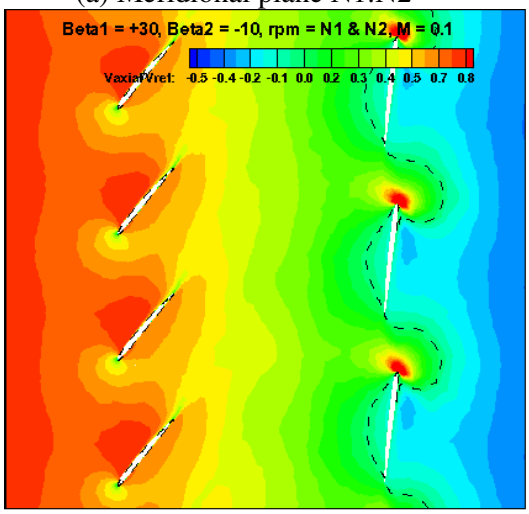

(c) 20% Front bladespan N1:N2

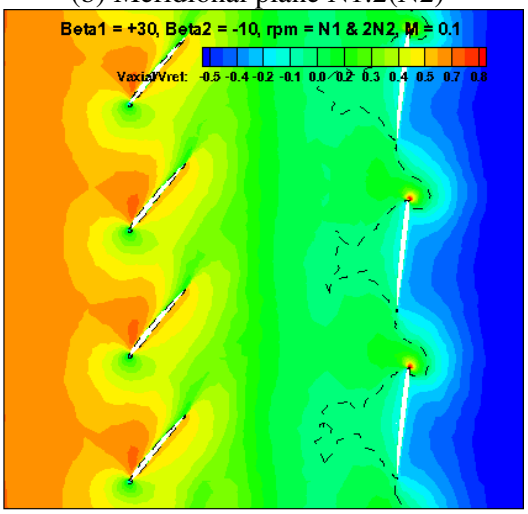

(d) 20% Front bladespan N1:2(N2)

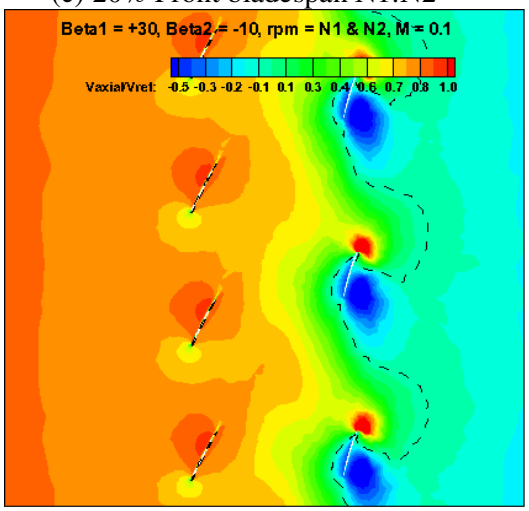

(e) 70% Front bladespan N1:N2

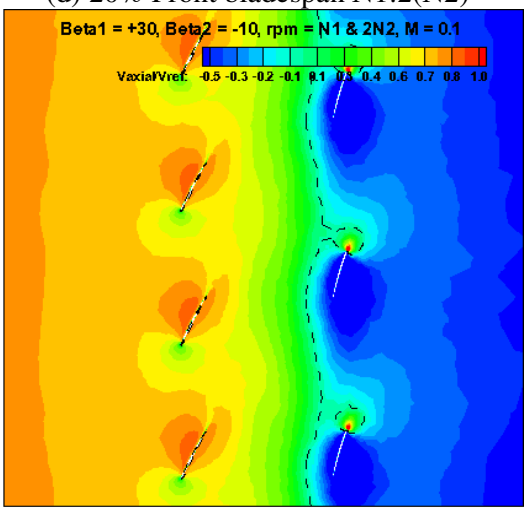

(f) 70% Front bladespan N1:2(N2)

Figure 5-24 Normalised axial velocity contours for CROR at $\beta_{1,2}$ =+30˚,-10˚, M=0.1.

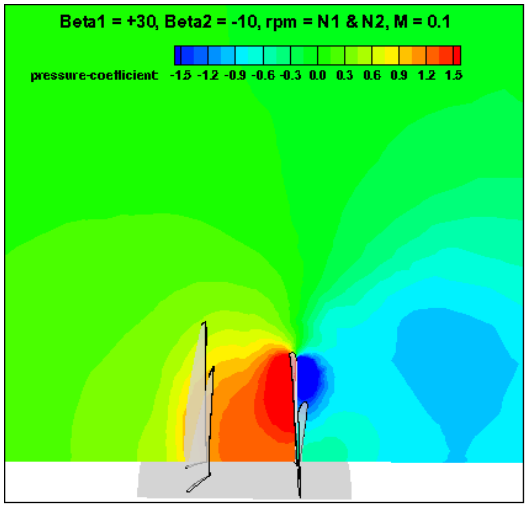

(a) Meridional plane N1:N2

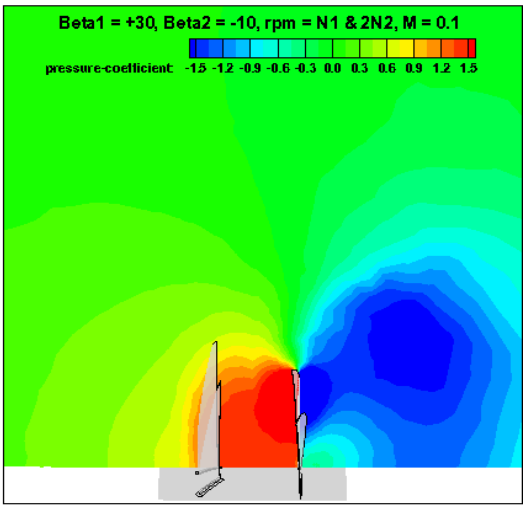

(b) Meridional plane N1:2(N2)

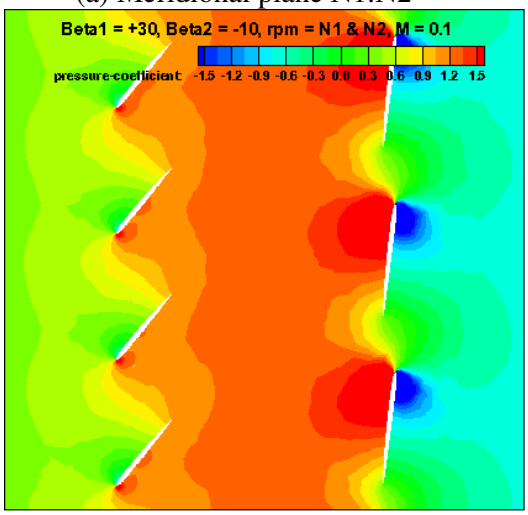

(c) 20% Front bladespan N1:N2

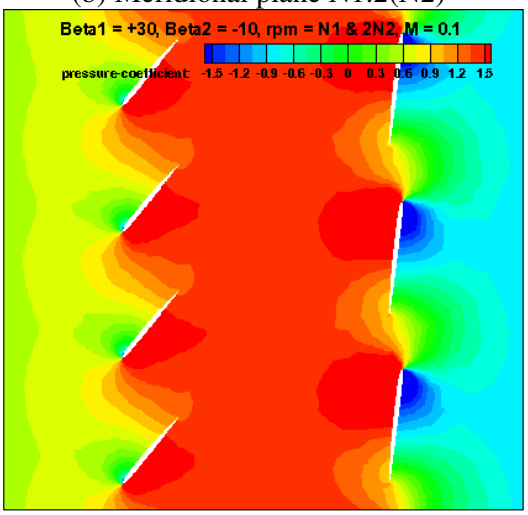

(d) 20% Front bladespan N1:2(N2)

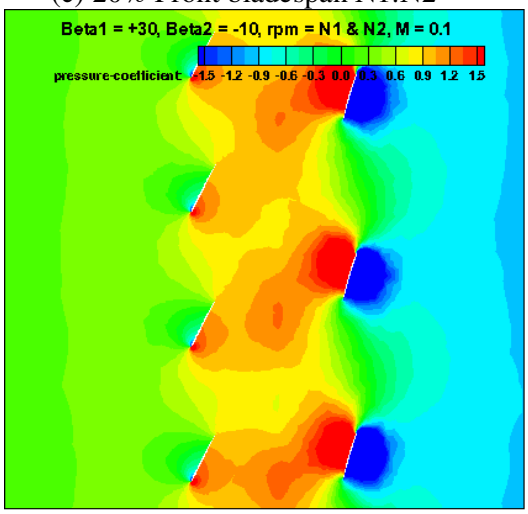

(e) 70% Front bladespan N1:N2

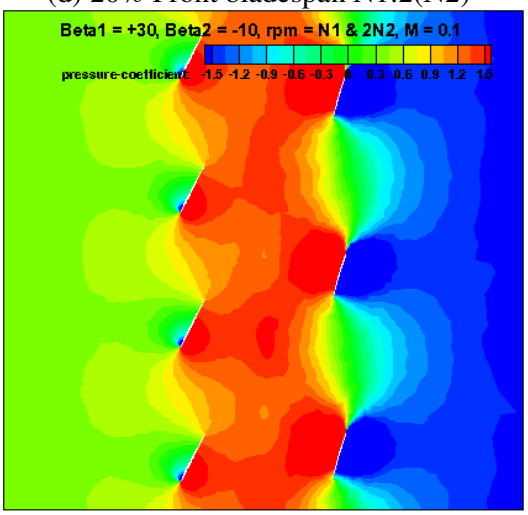

(f) 70% Front bladespan N1:2(N2)

Figure 5-25 C_p contours for CROR at $\beta_{1,2}$ =+30˚,-10˚ and M = 0.1

Upon comparing meridional C_p contours in *Figure 5-25* (a) and (b), for aft rpm N2 and 2(N2) respectively, a large increase in negative C_p downstream of the aft rotor is clearly observed. In both aft rpm cases this region of relative pressure drop appears to be generated by the outboard portion of the aft rotor blades. This is due to aft blade twist and a growing negative pitch angle along the bladespan. This results in the outboard blade sections generating higher negative thrust. Evidence of this is given in aft rotor blade distribution in *Figure 5-26* (b) and *Figure 5-27* (b) for both aft rpm levels. This increase in relative low pressure is responsible for the increased strength in recirculation

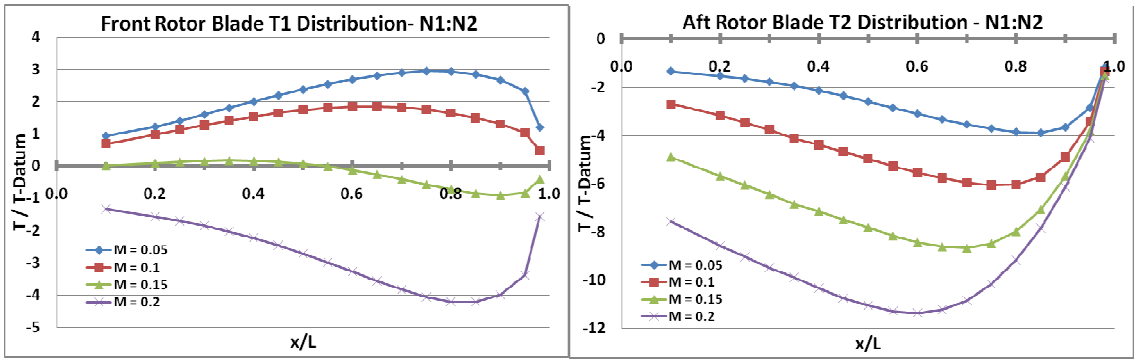

(a) front T_1 blade distribution (b) aft T_2 blade distribution

Figure 5-26 Average blade distribution from pressure forces for CROR at $\beta_{1,2}$ =+30˚,-10˚, rpm = N1:N2.

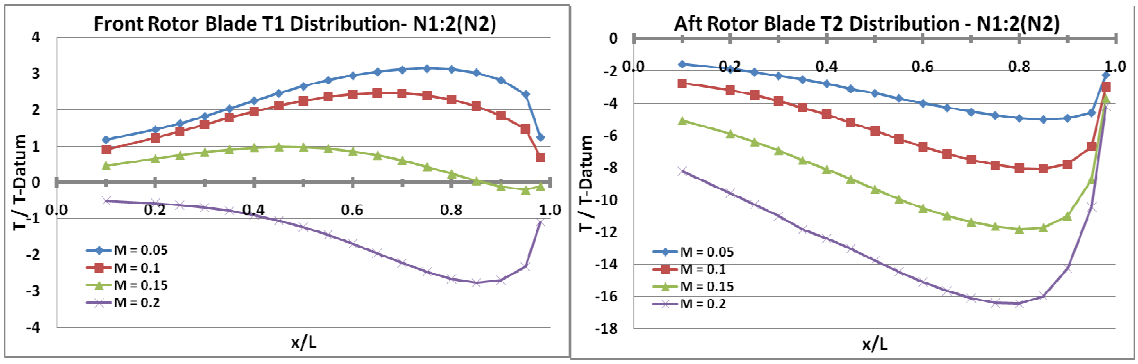

(a) front T_1 blade distribution (b) aft T_2 blade distribution

Figure 5-27 Average blade distribution from pressure forces for CROR at $\beta_{1,2}$ =+30˚,-10˚, rpm = N1:2(N2).

5.2.6 Summary of findings (CROR at $\beta_{1,2}$ =+30˚,-10˚)

- For the majority of cases the front rotor produced positive thrust and the aft rotor produced negative thrust.

- The addition of a downstream aft rotor at negative pitch appears to create an adverse pressure gradient propagating upstream of the aft rotor. This reduces the wind velocity entering the front blade row allowing it to generate higher positive T_1 (for β_1 =+30˚). This consequently increases the M value at which transition from positive to negative T_1 occurs.

- In all simulation cases for this pitch combination the main flowfield feature is a large recirculation region downstream of the aft rotor. The flow appears to pass through the front rotor and get deflected radially outwards as it continues downstream through the aft rotor.

- This recirculation was shown to be the result of a large relative pressure drop generated by the outboard suction surface of the aft rotor blades.

- Doubling front rpm causes a large increase in blade force and moment for both rotors. This is due to increased positive C_p on the lower (pressure) front blade surface augmenting the positive C_p on the upper (pressure) aft blade surface.

- Compared to front rpm, doubling aft rpm has much less impact on blade loading of both rotors. While C_p and axial velocity indicate an increase in size and strength of the downstream recirculation region, only a modest thrust and torque change is observed.

5.2.7 Initial analysis for $\beta_{1,2}$ = -10˚, -20˚

Thrust and torque performance

On examining the CROR rotor thrust values in *Figure 5-28* (a) the dual negative pitch setting causes both rotors to generate negative thrust for all Mach numbers at rpm N1:N2. It is clear from *Figure 5-28* (a) that the front rotor produces more negative thrust than the aft rotor for all cases at this rpm setting. Higher velocity freestream flows augment negative T_2 magnitude however it appears that the majority of reverse thrust is generated from the front rotor. This is based on the observation of large negative T_1 increases at higher M values in *Figure 5-28* (a) which were expected due to single front rotor CFD results in *Figure 5-3*. Doubling the aft rotor rpm was seen to cause a significant increase in negative T_2 but to the detriment of front rotor performance which has experienced a decrease in its negative thrust production (*Figure 5-28* (b)). The experimental values in *Figure 5-28* (b) also depict an unexpected result of positive thrust generated by the front rotor at M = 0.05, despite having a negative pitch setting.

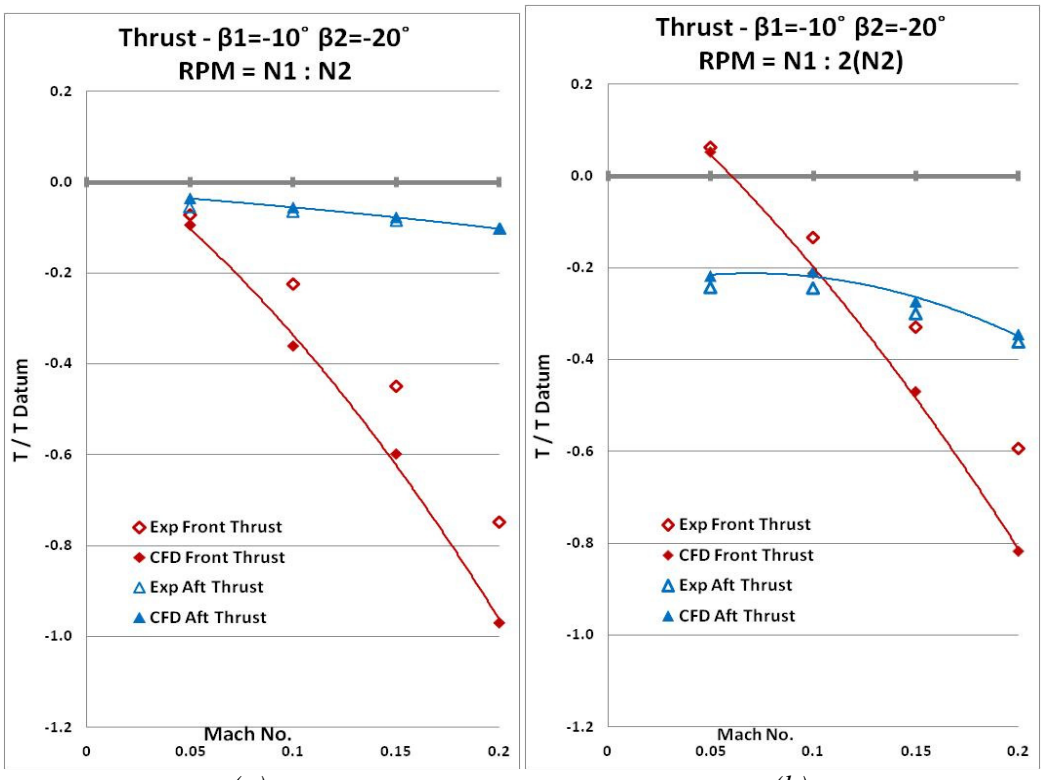

(a) *(b)*

Figure 5-28 Experimental and CFD rotor thrust values for $\beta_{1,2}$ = -10˚, -20˚.

CROR torque results are plotted in *Figure 5-29* for $\beta_{1,2}$ = -10˚, -20˚. The front torque (Q_1) trends correspond well to the measured T_1 behaviour for varying M and aft rpm in *Figure 5-28*. This is not the case for the aft torque at both rpm settings in *Figure 5-29* (a) and (b), which show a Q_2 decrease when freestream speed is increased from M = 0.05 to M = 0.1. Subsequent higher M values do result in Q_2 augmentation however this overall behaviour does not follow the thrust variation and may indicate an experimental discrepancy or an unusual change in distribution of blade forces

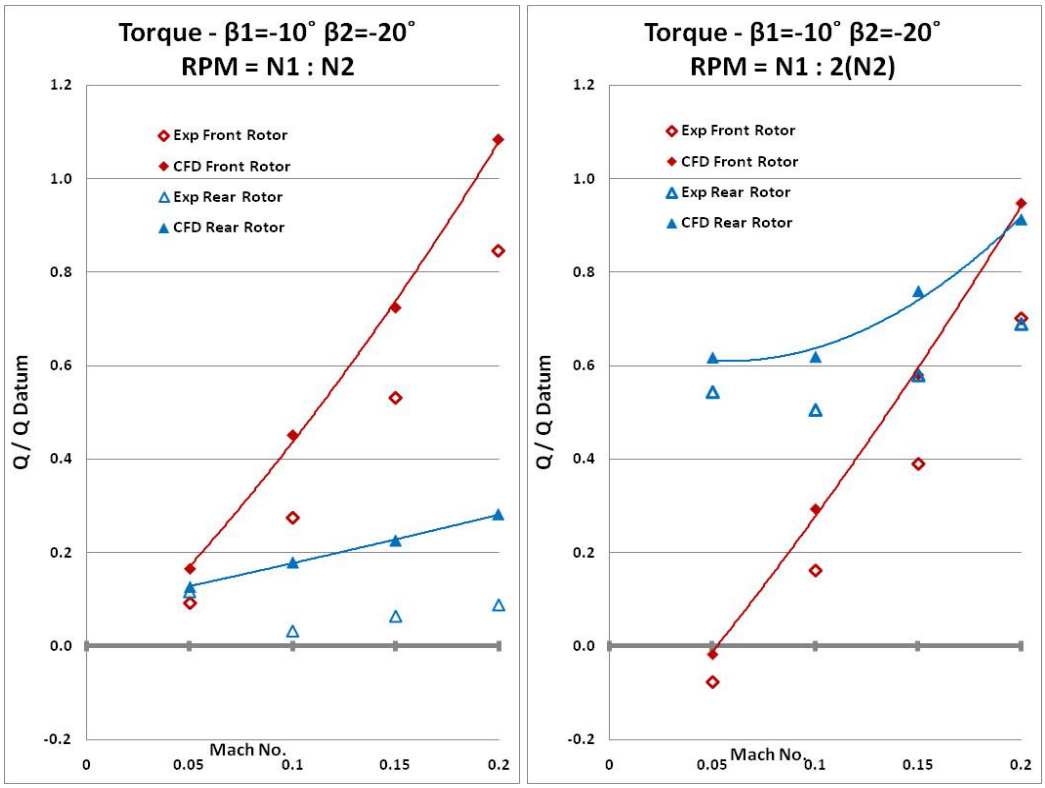

(a) *(b)*

Figure 5-29 Experimental and CFD rotor torque values for $\beta_{1,2}$ = -10˚, -20˚.

Flowfield assessment

To investigate the main flowfield features for the pitch setting of $\beta_{1,2}$ = -10˚, -20, *Figure 5-30* shows 3D streamlines and meridional contours of C_p and axial velocity for the case of M = 0.1 and rpm = N1:N2. A large area of recirculation is identified with the streamlines in *Figure 5-30*. This recirculation is shown in later sections to be affected

by rpm and Mach number however it remains the dominant flow feature present in all the CFD test cases for $\beta_{1,2}$ = -10˚, -20. This was also true for the recirculation observed in $\beta_{1,2}$ = +30˚, -10 cases. Streamlines and colour contours, of axial velocity normalised with freestream velocity, in *Figure 5-30* show that reverse flow is experienced through the front rotor, as well as the aft rotor. From this initial plot it appears that both rotors are inducing reverse flow and contributing to the recirculation. Looking at C_p lines in *Figure 5-30* a large negative region is shown downstream of the aft rotor with its location corresponding to the centre of recirculation. High C_p is shown to propagate upstream of the front rotor. This is the likely cause of deceleration in flow approaching the front rotor, shown in colour contours of axial velocity in *Figure 5-30.*

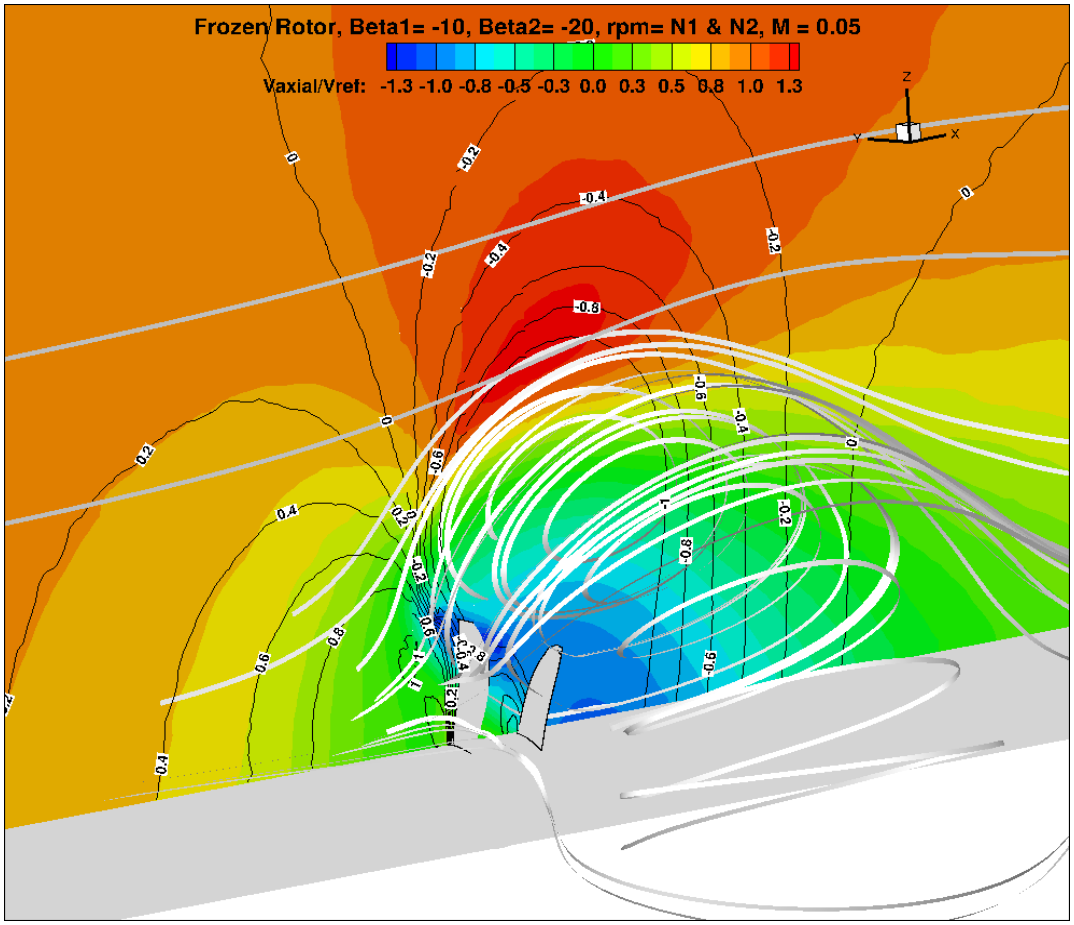

Figure 5-30 CROR contours and streamtraces for $\beta_{1,2}$ = -10˚, -20˚, rpm = N1:N2 and M = 0.05.

CFD validation

Focusing on the aft rotor thrust results first, the predictions shows excellent agreement with experimental T_2 values (*Figure 5-28* (a) and (b)). There is a slight increase in error brought on by doubling aft rpm (2xN2). All the predicted T_1 values are larger than experimental measurements. This level of T_1 over-prediction is quite small at the lowest flow speed however it grows to a notable difference (~25%) at the higher Mach number of 0.2. Nevertheless, the CFD predictions generally show the same trends as the experimental data but the agreement is not as good as that obtained for the previous pitch combination

Since the CFD calculations over-predicted work done by the front rotor for majority of cases, the torque results were anticipated to be over-predicted in the same manner. To that extent, it is observed in *Figure 5-29*(a) and (b) Q_1 values correspond well to the T_1 values. Notable differences are seen in the aft torque calculation however, with Q2 values larger than the experimental measurements. This was unexpected given the excellent agreement of T_2 quantities.

5.2.8 Mach number variation for $\beta_{1,2}$ = -10˚, -20˚

To examine the effect of Mach number on the flowfield of contra-rotating open rotors at $\beta_{1,2}$ =-10˚,-20˚ and rpm= N1:N2, contours of axial velocity normalised with freestream velocity are shown in *Figure 5-31* for M = 0.05 and M = 0.2 cases. At the lower Mach number *Figure 5-31* (a) shows reverse flow through both rotors with the outboard sections of both rotors experiencing the highest reverse axial velocities. *Figure 5-31* (b) illustrates that M = 0.2 has stopped any reverse flow upstream of the front rotor. The dashed line representing 0 m/s indicates that the recirculation has been forced closer to the hub by the higher Mach number flow in *Figure 5-31* (b). The dashed lines also indicate that a complex change of axial flow direction occurred in the area between the rotors and warrants further investigation. Contours of C_p on the same meridional plane are given in *Figure 5-32* (a) and (b) for M = 0.05 and M = 0.2 respectively. They both show the adverse pressure gradient upstream of the front rotor as well as the large

negative C_p region downstream of the aft rotor. At M = 0.05 it appears that the location of highest relative pressure drop is very close to the outboard portion of the aft rotor (*Figure 5-32* (a)). This is logical since blade twist results in the outboard blade sections having the largest negative pitch settings and therefore generating the most reverse thrust. Blade force and moment distribution for the aft rotor in *Figure 5-33* (b) confirms this. When M = 0.2 the relative pressure drop, and centre of recirculation, in *Figure 5-32* (b) is forced inboard closer to the hub.

Figure 5-31 (c)(d) and (e)(f) contain circumferential contours of axial velocity at 20% and 70% front rotor bladespan respectively. Looking at 20% span first, *Figure 5-31* (c) shows a largely decelerated flow approaching the front blade row at M = 0.05. The plot also identifies a high speed reverse flow nearing the aft rotor. When M = 0.2 in *Figure 5-31* (d), the freestream is penetrating through the front rotor at higher speed. However, the dashed lines indicate no significant change in axial direction or strength of the reverse flow through the aft rotor, when compared to *Figure 5-31* (c). At 70% bladespan and M = 0.05, *Figure 5-31* (e) shows the axial velocity increase imparted to the reverse flow by the aft blade row as well as the extent upstream that it reaches after travelling through the front rotor.

When M=0.2 the freestream penetrates through the front rotor in *Figure 5-31* (f) where it enters a complex region of flow between the rotors, evident from the dashed line showing change in axial direction. Corresponding C_p contours at 20% bladespan in *Figure 5-32* (c) and (d) illustrate how little reverse flow the aft rotor is inducing at this height for both Mach numbers. At 70% front rotor bladespan and M = 0.05, *Figure 5-32* (e) clearly shows the airfoil sections of both rotors having a pressure and suction side as they induce reverse flow. This relates well to the axial velocity in *Figure 5-31* (e).

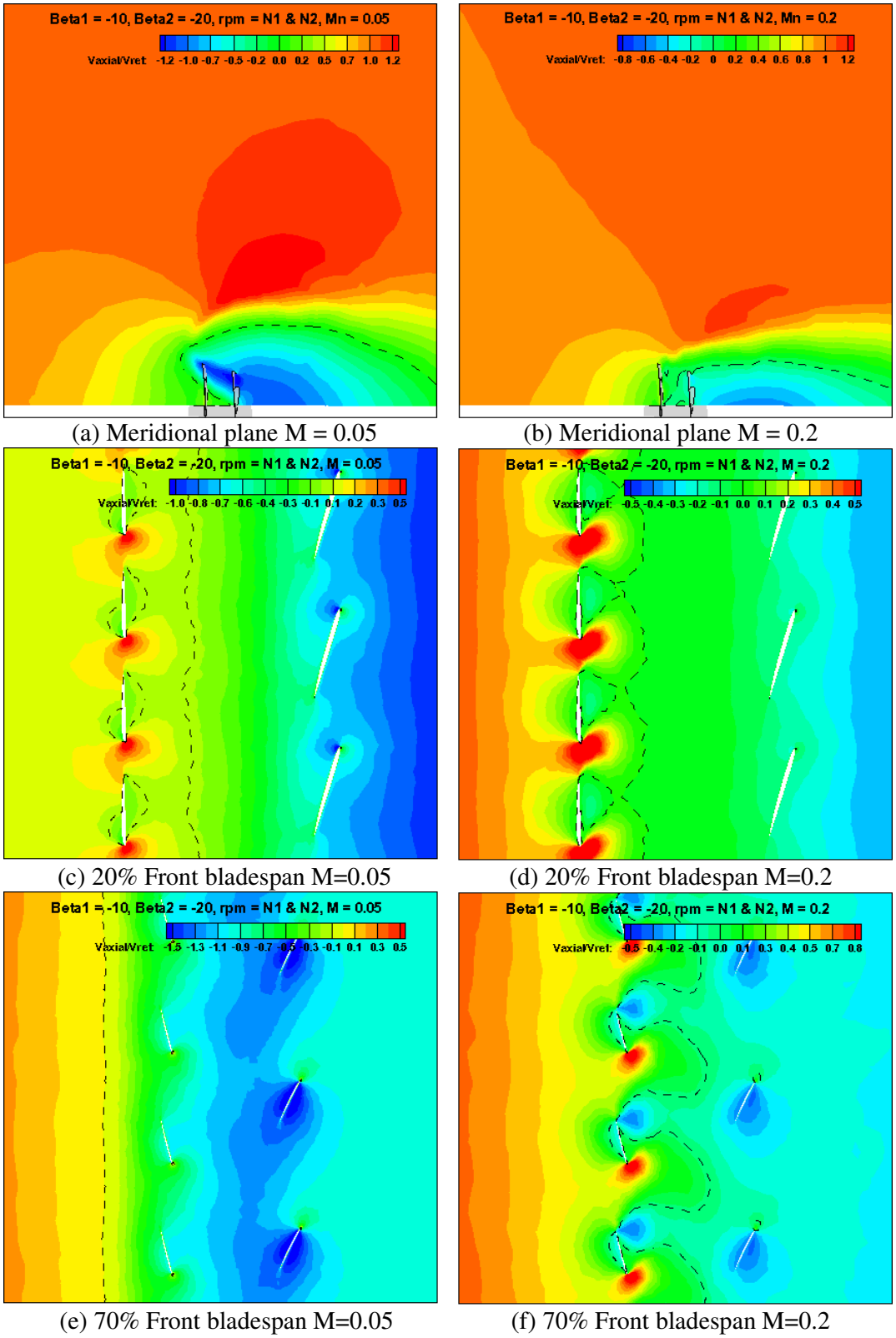

(a) Meridional plane M = 0.05

(b) Meridional plane M = 0.2

(c) 20% Front bladespan M=0.05

(d) 20% Front bladespan M=0.2

(e) 70% Front bladespan M=0.05

(f) 70% Front bladespan M=0.2

Figure 5-31 Normalised axial velocity contours for CROR at $\beta_{1,2}$ =-10˚,-20˚ and rpm= N1:N2.

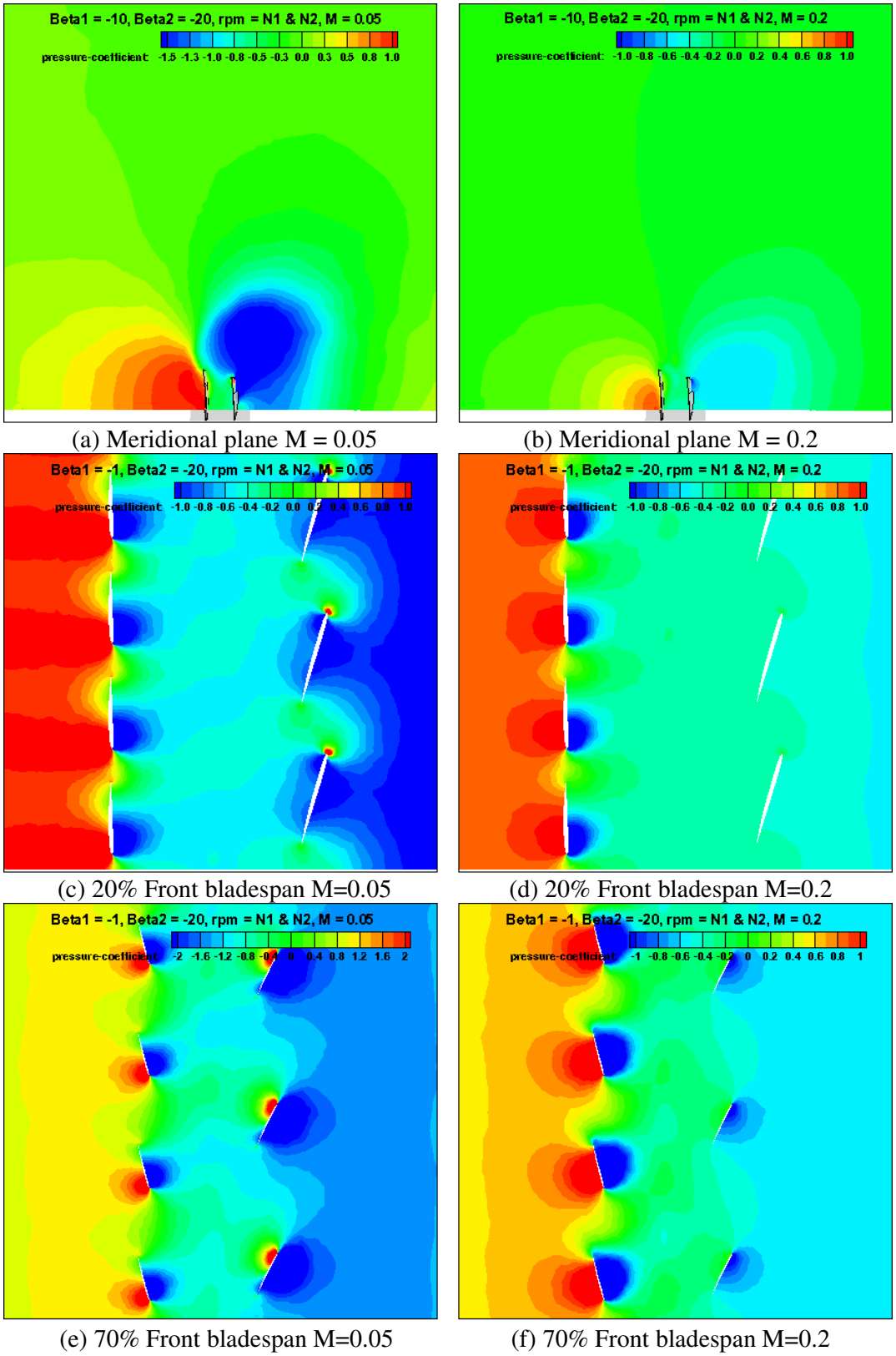

(a) Meridional plane M = 0.05

(b) Meridional plane M = 0.2

(c) 20% Front bladespan M=0.05

(d) 20% Front bladespan M=0.2

(e) 70% Front bladespan M=0.05

(f) 70% Front bladespan M=0.2

Figure 5-32 C_p contours for CROR at $\beta_{1,2}$ =-10˚,-20˚ and rpm= N1:N2.

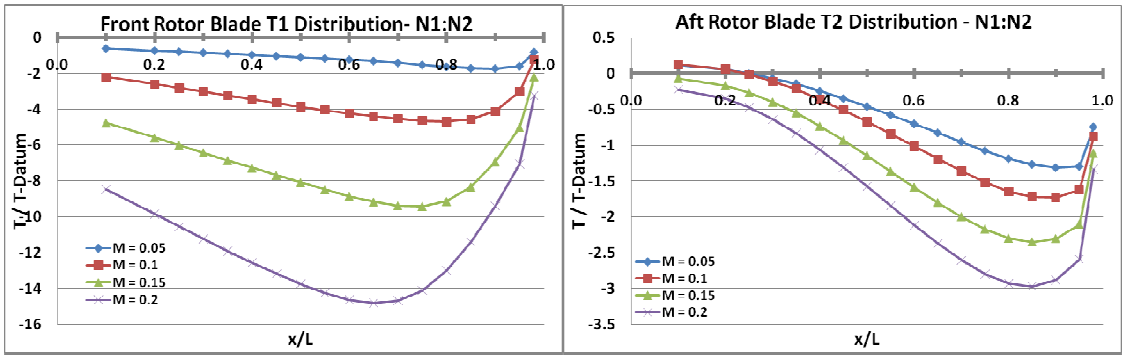

(a) front T_1 blade distribution (b) aft T_2 blade distribution

Figure 5-33 Average blade distribution from pressure forces for CROR at $\beta_{1,2}$ =-10˚,-20˚, rpm = N1:N2.

5.2.9 Rotor interaction for $\beta_{1,2}$ = -10˚, -20˚

The experimental results in *Figure 5-23* have already shown that increasing Mach number has little impact on aft performance, relative to the front rotor. This may already indicate the impact of one rotor on the others performance. *Figure 5-34* presents the CROR experimental and CFD T and Q results along with single rotor CFD results for both blade rows at $\beta_{1,2}$ =-10˚,-20˚ and rpm settings of N1 and N2. They clearly show the introduction of the front rotor substantially reduces the aft rotors ability to generate reverse thrust. Also the introduction of the aft rotor downstream of the front has little impact on front performance, based on CFD results. These two points are illustrated in circumferential C_p contours in *Figure 5-35* (a) and (b) for single front rotor and CROR respectively at M=0.1. At 70% blade span the aft rotor is seen to be operating in the negative C_p region generated by the front rotor. Contours around the front rotor blades at 70% span appear to be unaffected by introduction of the aft rotor.

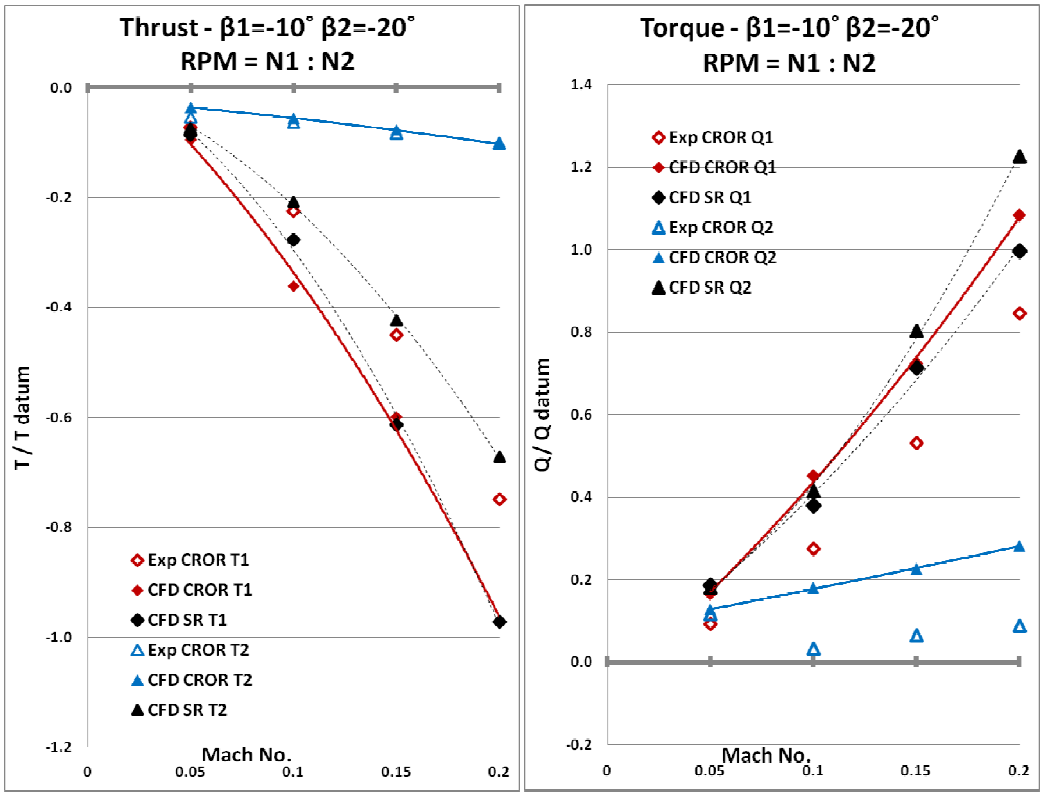

(a) (b)

Figure 5-34 Single rotor and contra-rotating T and Q results for $\beta_{1,2}$ = -10˚, -20˚ and rpm N1:N2.

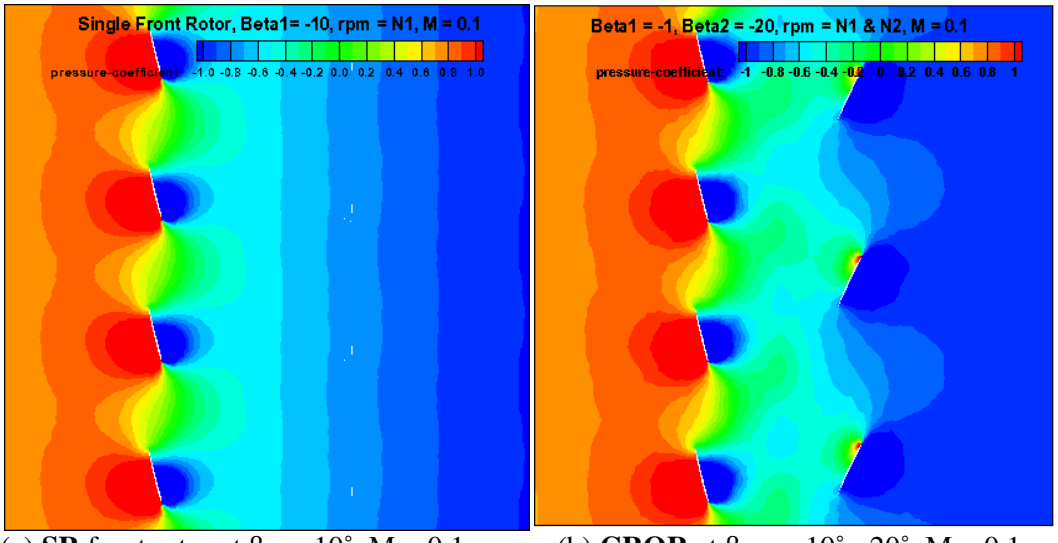

(a) **SR** front rotor at β_1 = -10˚, M = 0.1 and rpm N1.

(b) **CROR** at $\beta_{1,2}$ = -10˚, -20˚, M = 0.1 and rpm N1:N2

Figure 5-35 Circumferential C_p contours at 70% front rotor bladespan.

5.2.10 Aft rpm variation for $\beta_{1,2}$ = -10˚, -20˚

The effect of increased aft rpm on rotor performance has already been identified in the initial analysis, however by combining the experimental results for a constant front rpm of N_1 it is better illustrated in *Figure 5-36*. Thrust values in *Figure 5-36* (a) show that doubling aft rpm was seen to cause a significant increase in negative T_2 but a reduction in negative T_1. This reduction in negative T_1 has even gone to the point where at M = 0.05 and rpm=N1:2(N2), the front rotor generates a positive thrust despite having negative pitch. Looking at the front rotor torque results in *Figure 5-36* (b), Q_1 trends relate well to T_1 results. A negative Q_1 value was expected at M = 0.05 after observing a positive T_1 from the negative pitch front rotor. This is because the direction of flow has reversed through the front rotor.

Another observation from increased aft rpm results in *Figure 5-36* (a) is the minimal change in T_2 when M is increased from 0.05 to 0.1. *Figure 5-36* (b) shows Q_2 behaves unexpectedly, also when M is increased from 0.05 to 0.1, at both aft rpms. If not experimental discrepancies, these three observations may point to a considerable change lift and drag forces on each blade, and subsequently how those forces are resolved into thrust and torque.

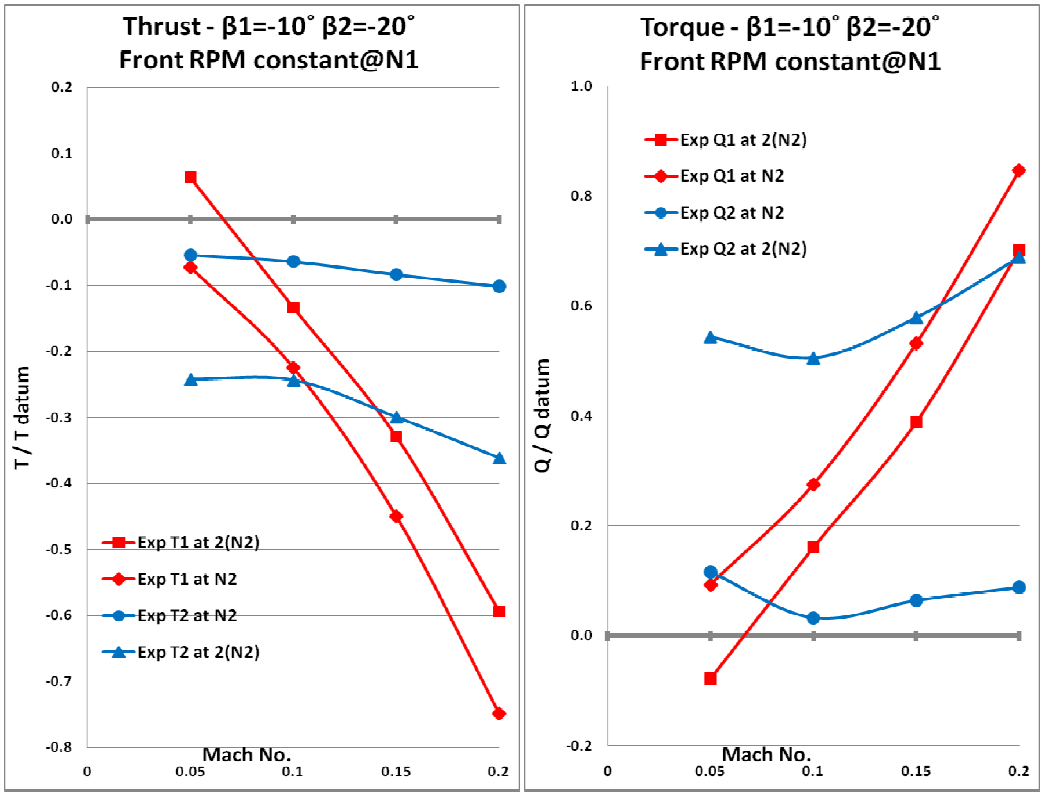

(a) *(b)*

Figure 5-36 Experimental rotor T and Q values for $\beta_{1,2}$ = -10˚, -20˚ with constant front rotor rpm N1.

To investigate the main flowfield features for the pitch setting of $\beta_{1,2}$ = -10˚, -20, *Figure 5-30* shows streamlines and meridional contours of C_p and axial velocity for the case of M = 0.1 and rpm = N1:N2. A large area of recirculation is identified with the streamlines in *Figure 5-30*. This recirculation is shown in later sections to be affected by rpm and Mach number however it remains the dominant flow feature present in all the CFD test cases for $\beta_{1,2}$ = -10˚, -20. This was also true for the recirculation observed in $\beta_{1,2}$ = +30˚, -10 cases. Streamlines and colour contours, of axial velocity normalised with freestream velocity, in *Figure 5-30* show that reverse flow is experienced through the front rotor, as well as the aft rotor. From this initial plot it appears that both rotors are inducing reverse flow and contributing to the recirculation. Looking at C_p lines in *Figure 5-30* a large negative region is shown downstream of the aft rotor with its location corresponding to the centre of recirculation.

High C_p is shown to propagate upstream of the front rotor. This is the likely cause of deceleration in flow approaching the front rotor, shown in colour contours of axial velocity in *Figure 5-30*.

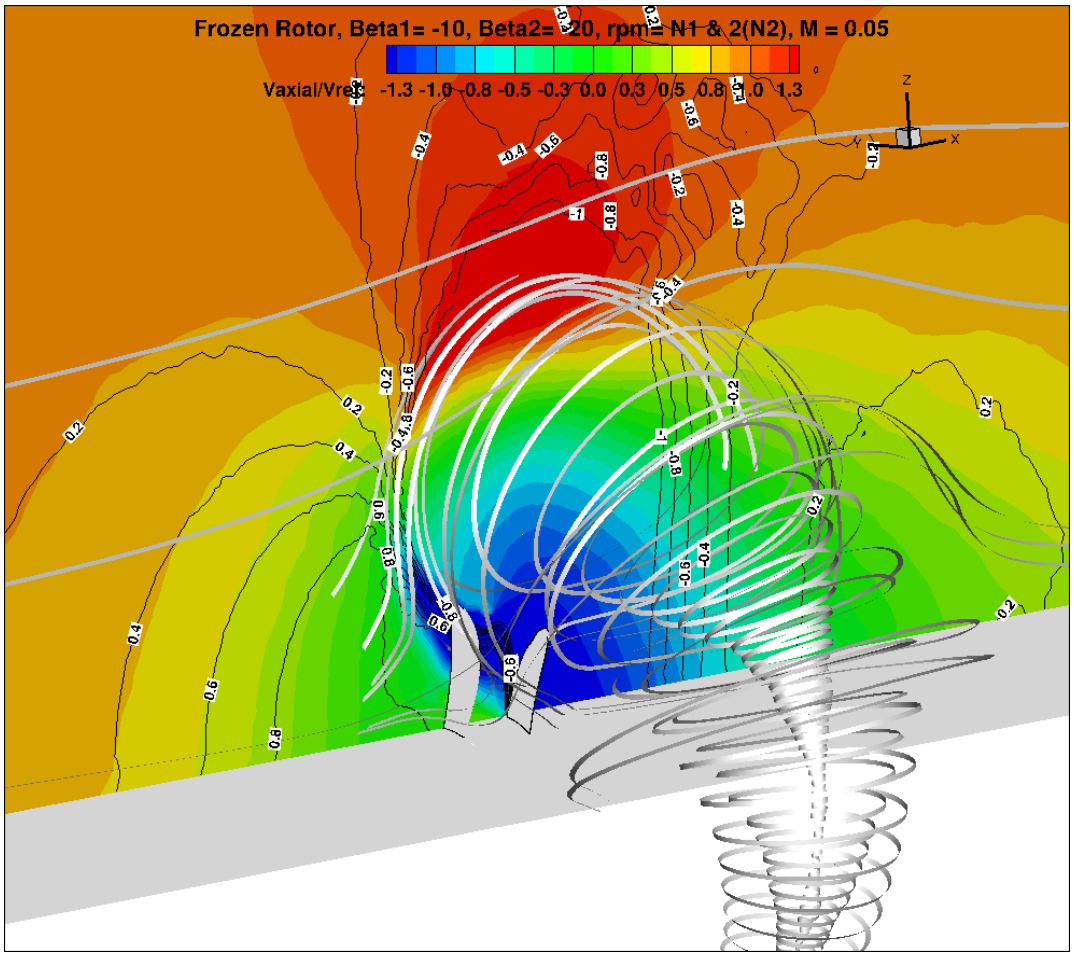

Figure 5-37 CROR contours and streamlines for $\beta_{1,2}$ = -10˚, -20˚, rpm = N1:2(N2) and M = 0.05.

Main flowfield features for $\beta_{1,2}$ = -10˚, -20˚ and M = 0.05, with aft rpm doubled to 2(N2), are presented in *Figure 5-37*. Streamlines show the recirculation extending further outwards (radially) from the hub, when compared to *Figure 5-30*. Colour contours of axial velocity show a large magnitude of reverse flow through both rotors. To compare more clearly the differences in axial velocity and C_p contours caused by aft rpm increase, the M = 0.05 case is illustrated for both rpm combinations in *Figure 5-38* and *Figure 5-39*.

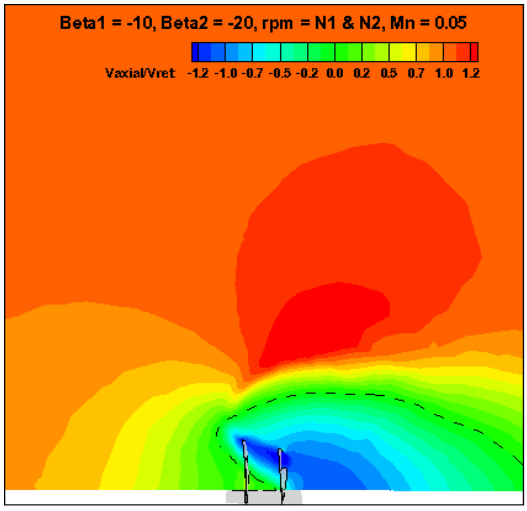

(a) Meridional plane rpm N1:N2

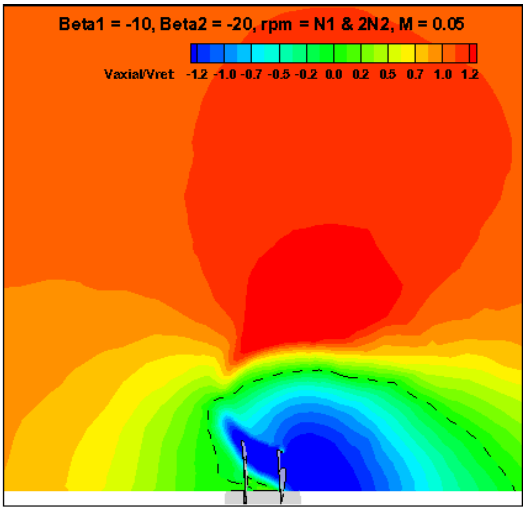

(b) Meridional plane rpm N1:2(N2)

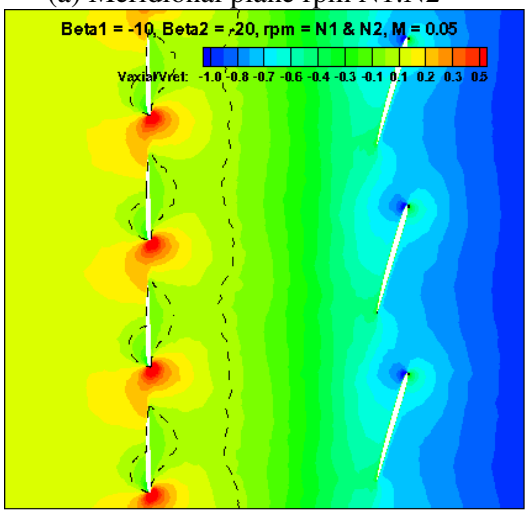

(c) 20% Front bladespan rpm N1:N2

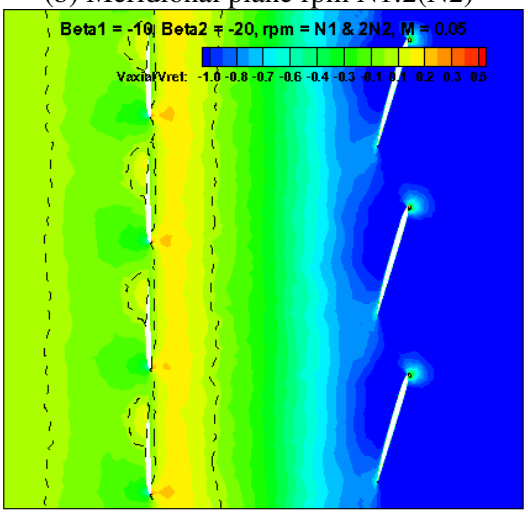

(d) 20% Front bladespan rpm N1:2(N2)

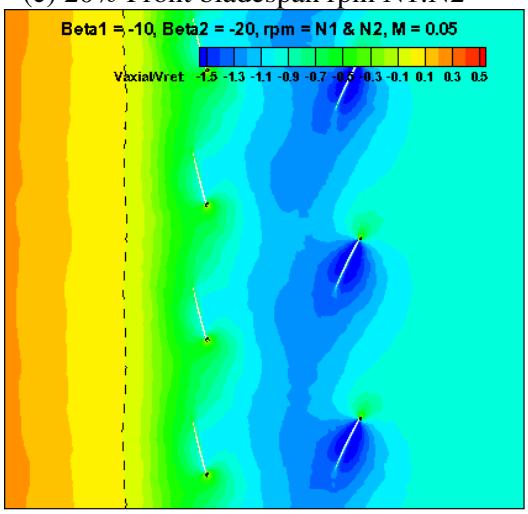

(e) 70% Front bladespan rpm N1:N2

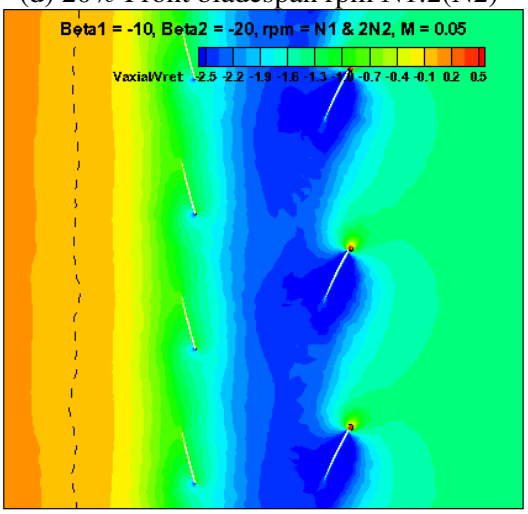

(f) 70% Front bladespan rpm N1:2(N2)

Figure 5-38 Normalised axial velocity contours for CROR at $\beta_{1,2}$ =-10˚,-20˚ M=0.05.

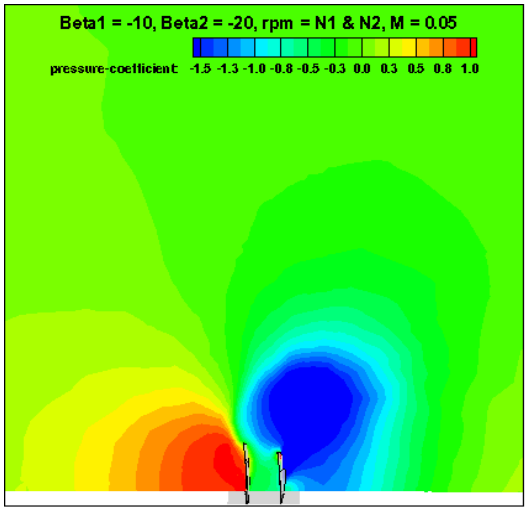

(a) Meridional plane rpm N1:N2

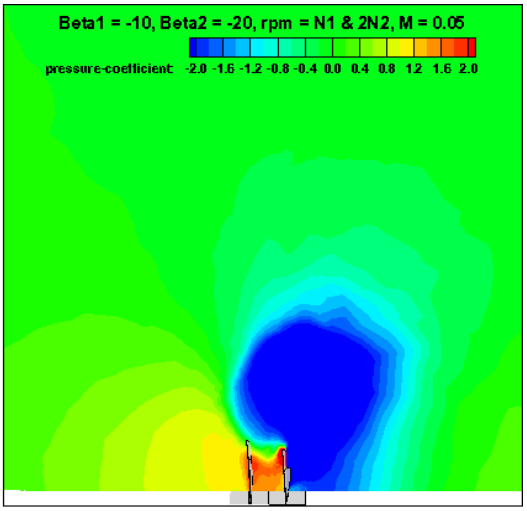

(b) Meridional plane rpm N1:2(N2)

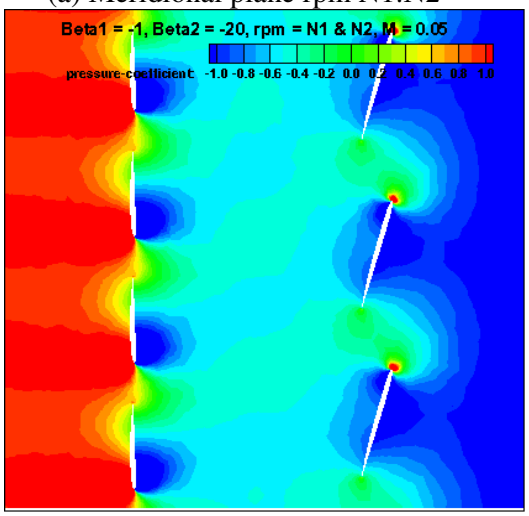

(c) 20% Front bladespan rpm N1:N2

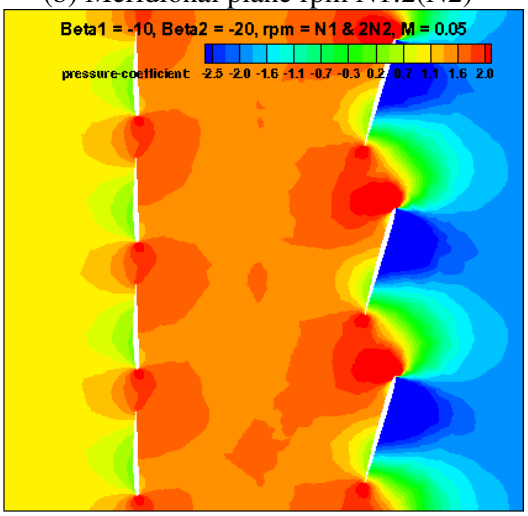

(d) 20% Front bladespan rpm N1:2(N2)

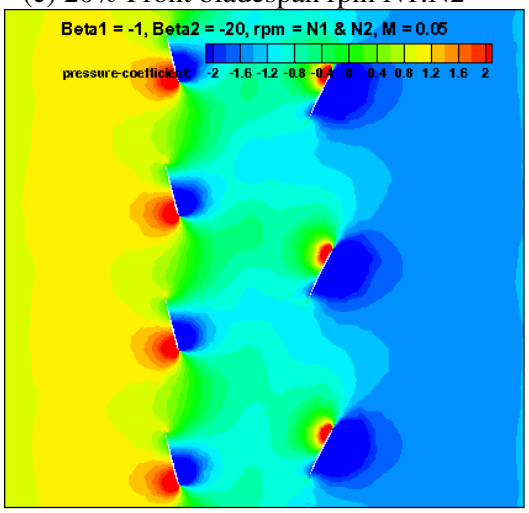

(e) 70% Front bladespan rpm N1:N2

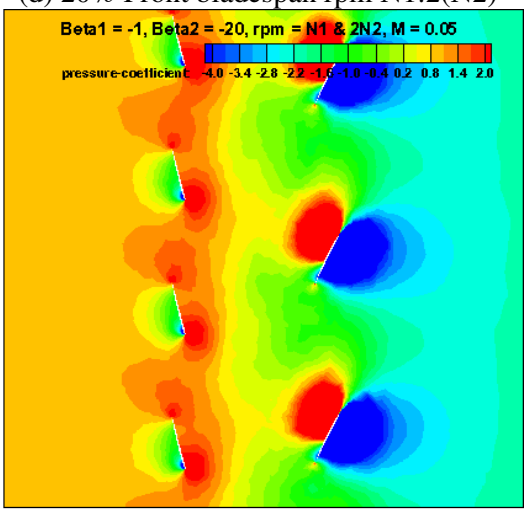

(f) 70% Front bladespan rpm N1:2(N2)

Figure 5-39 C_p contours for CROR at $\beta_{1,2}$ = -10˚,-20˚ M = 0.05.

In the meridional views in *Figure 5-38* (a) and (b), the magnitude of reverse flow is seen to increase substantially as it approaches the aft rotor, and as it is propelled through the outboard sections of both rotors. However the dashed lines indicate that reverse flow propagates through the inboard sections of the front rotor due to aft rpm increase. This is also illustrated in *Figure 5-38* (c) and (d) with circumferential contours at 20% front bladespan. The strength of reverse flow is so great that it propagates upstream from the front rotor even at this small blade height of 20%, where the local pitch angle is closer to 0˚ than -10˚ due to blade twist. *Figure 5-38* (e) and (f) demonstrate the reverse flow velocity increase from the aft blade row as well as its extension upstream.

Upon examining the meridional C_p contours in *Figure 5-39* (a) and (b), a large growth in magnitude and size is seen in the negative C_p region, explaining the radial expansion of the recirculation further into the freestream (*Figure 5-37*). There is a similar adverse pressure gradient seen ahead of the front rotor however, the aft rpm increase has resulted in a high pressure region in between the rotors. This would explain why T_1 is positive despite negative pitch. It appears that the axial magnitude of reverse flow exiting the aft blade row (Figure 5-38(f)) is so large, the front rotor is now slowing the reverse flow through it. The front pitch setting of β_1= -10˚ is too small in magnitude to impart a velocity increment to the reverse flow because the blades experience a negative relative incidence angle. Circumferential C_p contours in *Figure 5-39* (d) and (f) confirm the change in blade loading for the front rotor at 20% and 70% bladespan respectively. This is also shown with blade T distribution plots from integrated pressure forces in *Figure 5-40* (b).

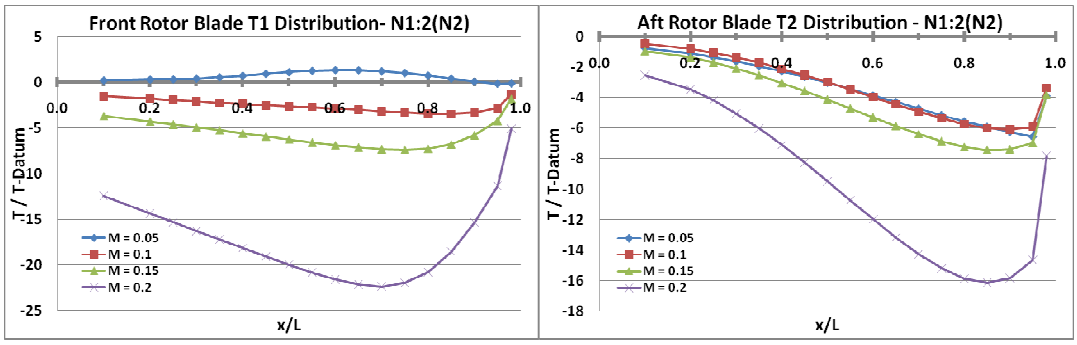

(a) front T_1 blade distribution (b) aft T_2 blade distribution

Figure 5-40 Average blade distribution from pressure forces for CROR at $\beta_{1,2}$ =-10˚,-20˚, rpm = N1:2(N2).

5.2.11 Summary of findings (CROR at $\beta_{1,2}$ =-10˚,-20˚)

- At rpm N1:N2 both rotors generate negative thrust which increases at higher Mach numbers. However, the majority of negative T is produced by the front rotor.

- As with $\beta_{1,2}$ =+30˚,-10˚, the main flow feature in all cases for this pitch combination is a large recirculation region. Due to both rotors at negative pitch, both are contributing to the negative C_p area causing the recirculation. Therefore the recirculation region is larger than those from $\beta_{1,2}$ =+30˚,-10˚ cases. The centre of negative C_p is located radially outwards, closer to the outboard sections of both rotors.

- At lower M values reverse flow is seen to propagate upstream through both rotors. This as well as the increased size and strength of recirculation has caused a much greater deflection of freestream flow away from the hub surfaces.

- Increasing aft rpm was seen to cause a significant increase in negative T_2 but to the detriment of front rotor performance which has experienced a decrease in its negative thrust production.
- Increasing aft rpm at M=0.05 resulted in positive thrust generated by the front rotor, despite having a negative pitch setting. This was found to be the result of such a high velocity reverse flow induced by the aft rotor. The front rotor decelerated the reverse flow through it because the magnitude of negative β_1 was too small to impart further negative velocity increments to the reverse flow. The resulting front rotor blade relative incidence angle was negative (see *Figure 5-2*(b)).

5.3 CROR unsteady full rotor CFD results

This sections contains CFD blade thrust and torque variation with timestep for both rotors during the single operating case investigated with unsteady sliding-mesh technique ($\beta_{1,2}$ = -10˚, -20˚, rpm = N1:N2 and M = 0.05). It also contains circumferential contour plots of C_p at differing timesteps. The main purpose of these results is to highlight any performance change with variation in rotor relative position.

5.3.1 Performance analysis

The unsteady blade thrust variation with timestep for all front and aft rotor blades are presented in *Figure 5-41* (a) and (b) respectively. Also included are the experimental blade average values and also CFD frozen rotor blade average values for comparison. The unsteady blade torque results are presented in similar comparable format in *Figure 5-42* (a) and (b) for front and aft rotor respectively. Both figures indicate that after a total of 1080 timesteps, the front and aft T and Q values appear to have reached asymptotic convergence towards constant values for the simulation. They also show that the unsteady sliding mesh calculation has not yielded very accurate results, after comparing to the experimental values included in the plots.

While this unsteady CFD case did not predict rotor performance more accurately than the equivalent steady frozen rotor calculation, its results in *Figure 5-41* and *Figure 5-42* do show one critical trend. There appears to be nominal variation of T and Q with timestep, in the latter stages of the simulation. This shows that the unsteady rotor interaction effects due to relative phase (rotational) position are small. If the performance of one blade row is proven to remain mostly independent of its position relative to the other blade row, then the main disadvantage of the frozen rotor approach is removed for CFD prediction of CROR reverse thrust operation.

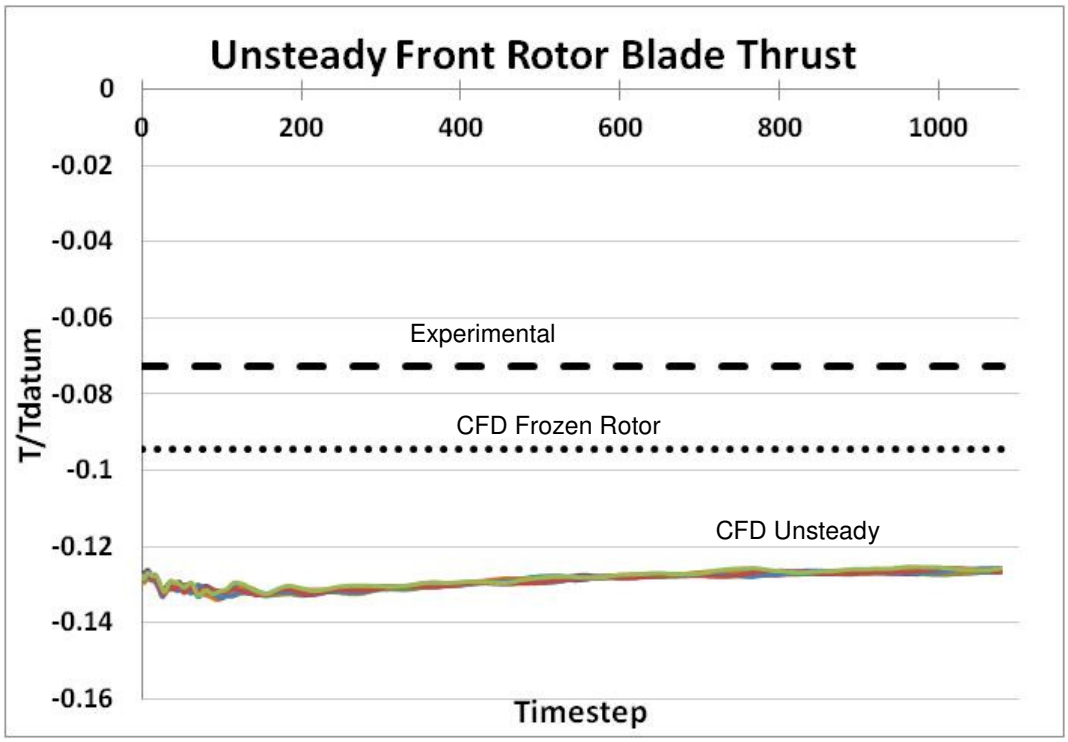

(a)

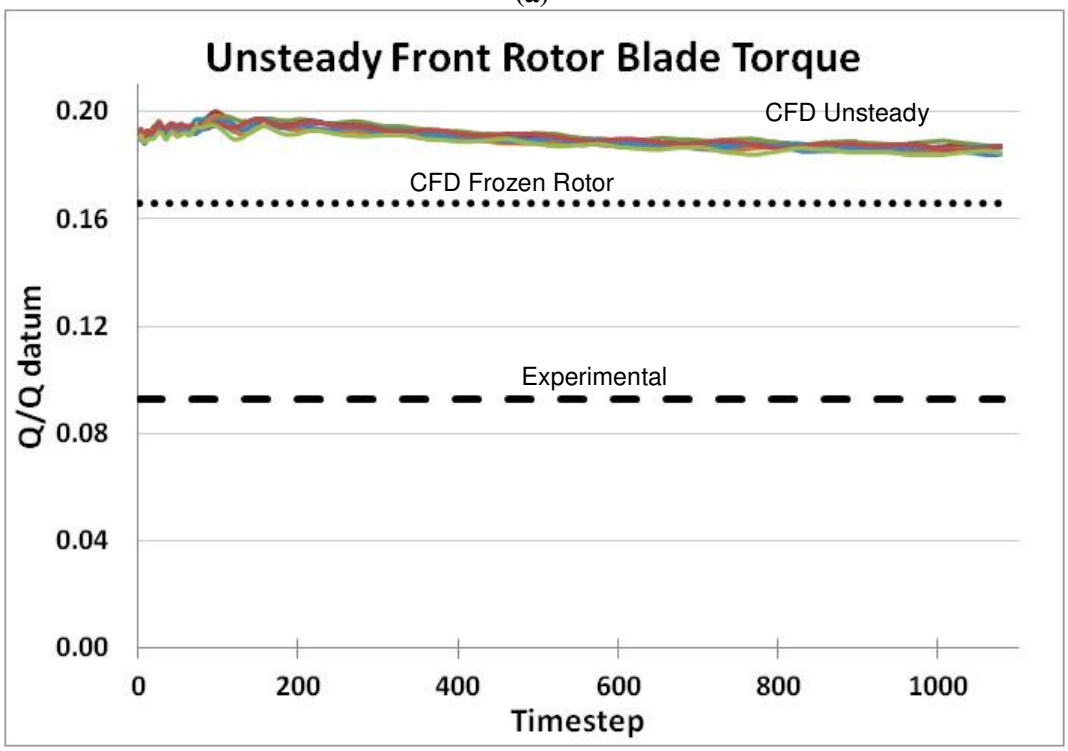

(b)

Figure 5-41 Unsteady front and aft blade thrust variation with timestep for $\beta_{1,2}$ = -10˚, -20˚, rpm = N1:N2 and M = 0.05.

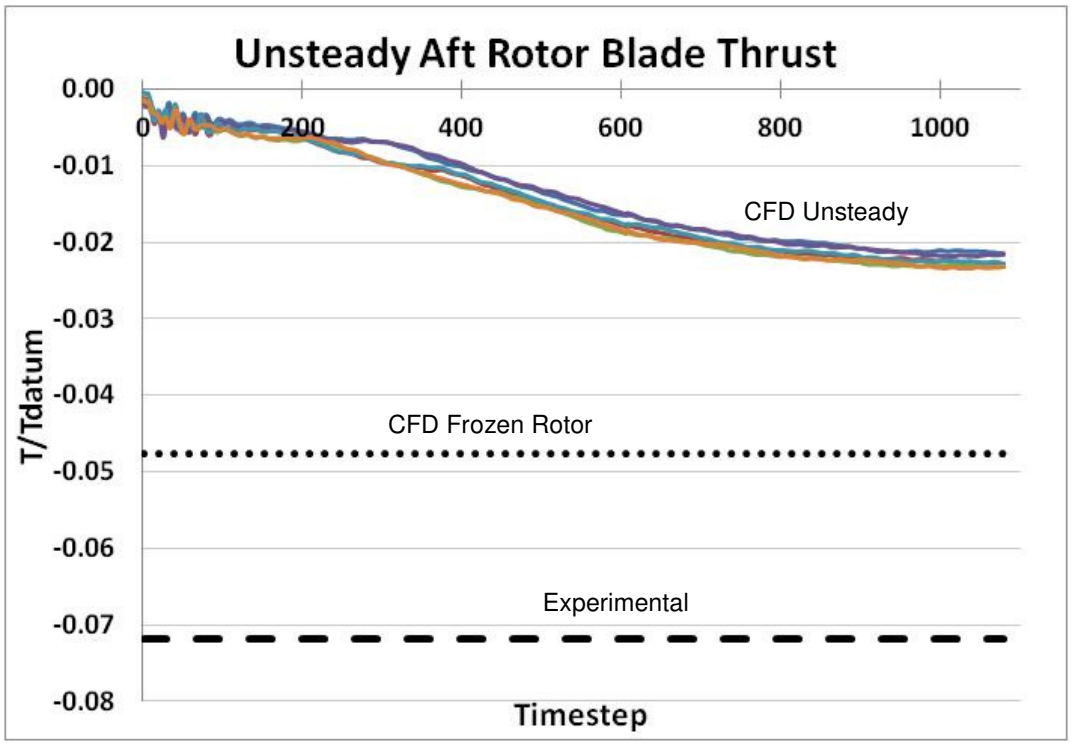

(a)

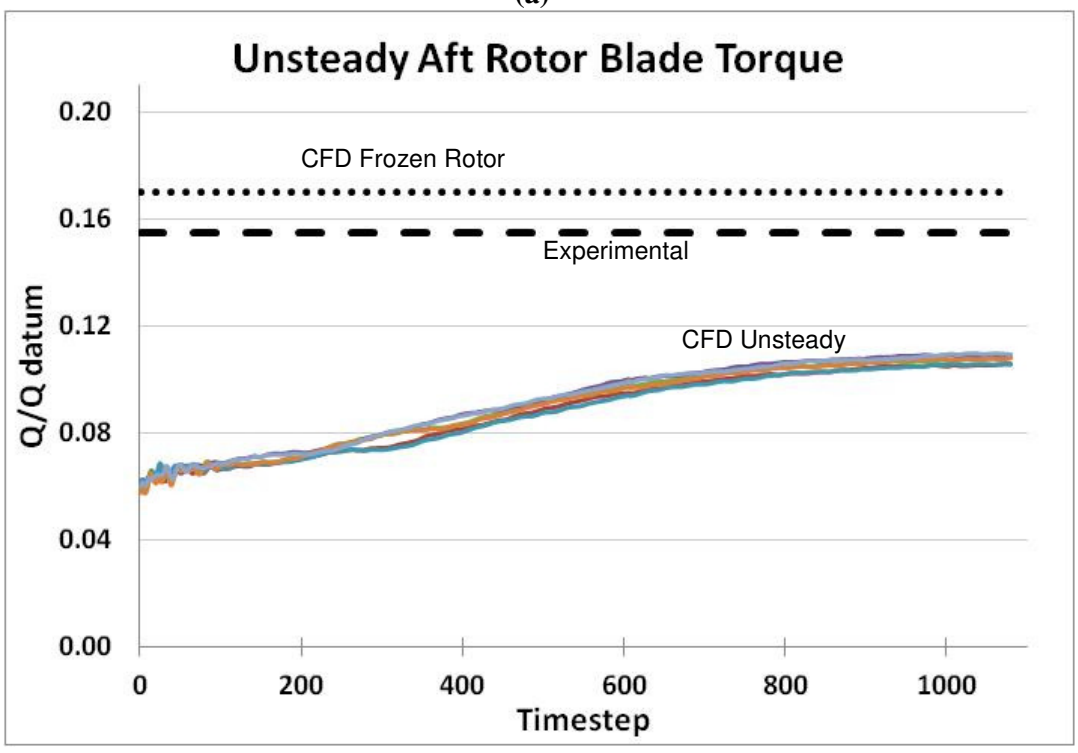

(b)

Figure 5-42 Unsteady front and aft blade torque variation with timestep for $\beta_{1,2}$ = -10˚, -20˚, rpm = N1:N2 and M = 0.05

5.3.2 Flowfield assessment

Upon examining unsteady contours of C_p in Figure 5-43, similarities can be seen with the flowfield C_p behaviour of the frozen rotor calculation of $\beta_{1,2}$ = -10˚, -20˚, rpm = N1:N2 and M = 0.05 (*Figure 5-39* (a) and (e)). Meridional contours in *Figure 5-43* (a) show high C_p region propagating upstream of the front blade row, with a large negative C_p area centred in the recirculation region, depicted by the normalised axial velocity contours in *Figure 5-44*. A notable difference between the unsteady and frozen rotor cases is the relative pressure drop in between the rotors, shown by the negative C_p region in *Figure 5-43* (a) and (b). Circumferential C_p contours at 70% front rotor bladespan show similar blade loading pattern to that in *Figure 5-39* (e) for frozen rotor calculation. However *Figure 5-43* (b) shows increased negative C_p on the suction surfaces of the front rotor blades. The negative C_p area in between the rotors has also reduced the positive C_p on the pressure surface of the aft blades. This relates to the front and aft rotor T results in *Figure 5-41* where the front rotor is over-predicting thrust and the aft rotor is under-predicting thrust.

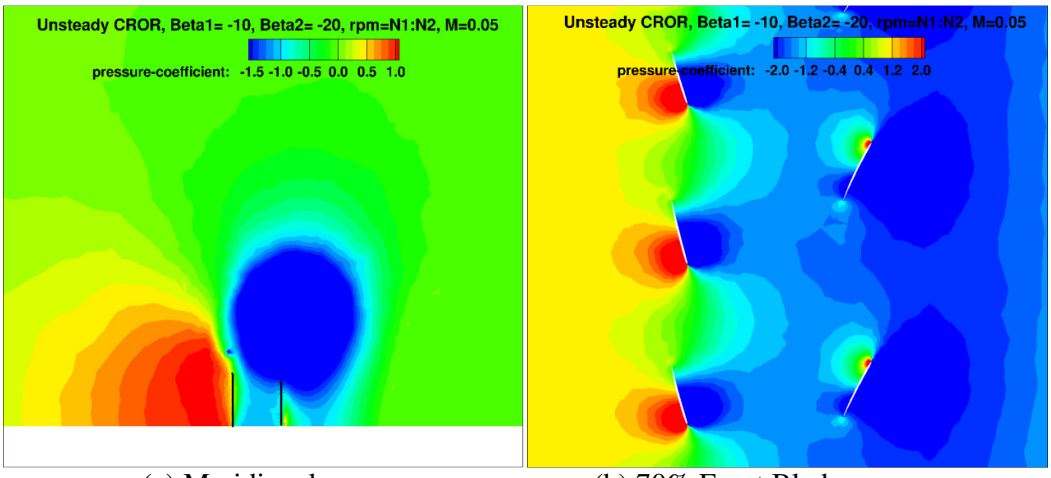

(a) Meridional (b) 70% Front Blade span

Figure 5-43 Unsteady C_p contours for $\beta_{1,2}$ = -10˚, -20˚, rpm = N1:N2 and M = 0.05.

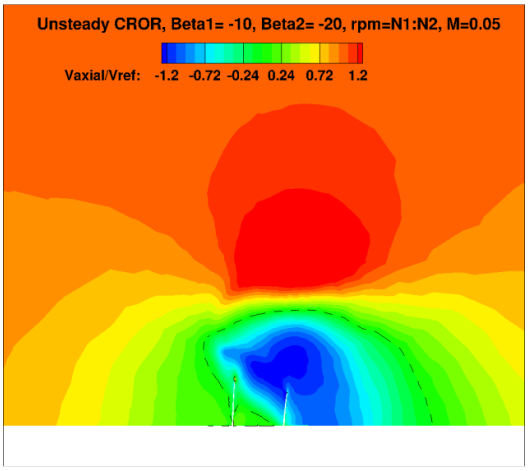

Figure 5-44 Unsteady meridional normalised axial velocity contours for $\beta_{1,2}$ = -10˚, -20˚, rpm = N1:N2 and M = 0.05.

5.3.3 Unsteady interaction effects due to rotor phase position

To investigate the level of unsteady interaction for this sliding-mesh calculation, contours of C_p are presented in *Figure 5-45* for varying phase positions. These circumferential contours are taken at 70% front rotor bladespan and at 5 different timesteps. The contour levels have been adjusted from that in *Figure 5-43* (b) to a more refined range, in order to better highlight any unsteady interaction effects. It is clear by examining *Figure 5-45* (a) to (e) that there is little change in C_p as the phase position progresses in movements of 12 timesteps. This is further evidence that the frozen rotor approach can be utilised for open rotor CFD reverse thrust investigations without major impact to fidelity of the results.

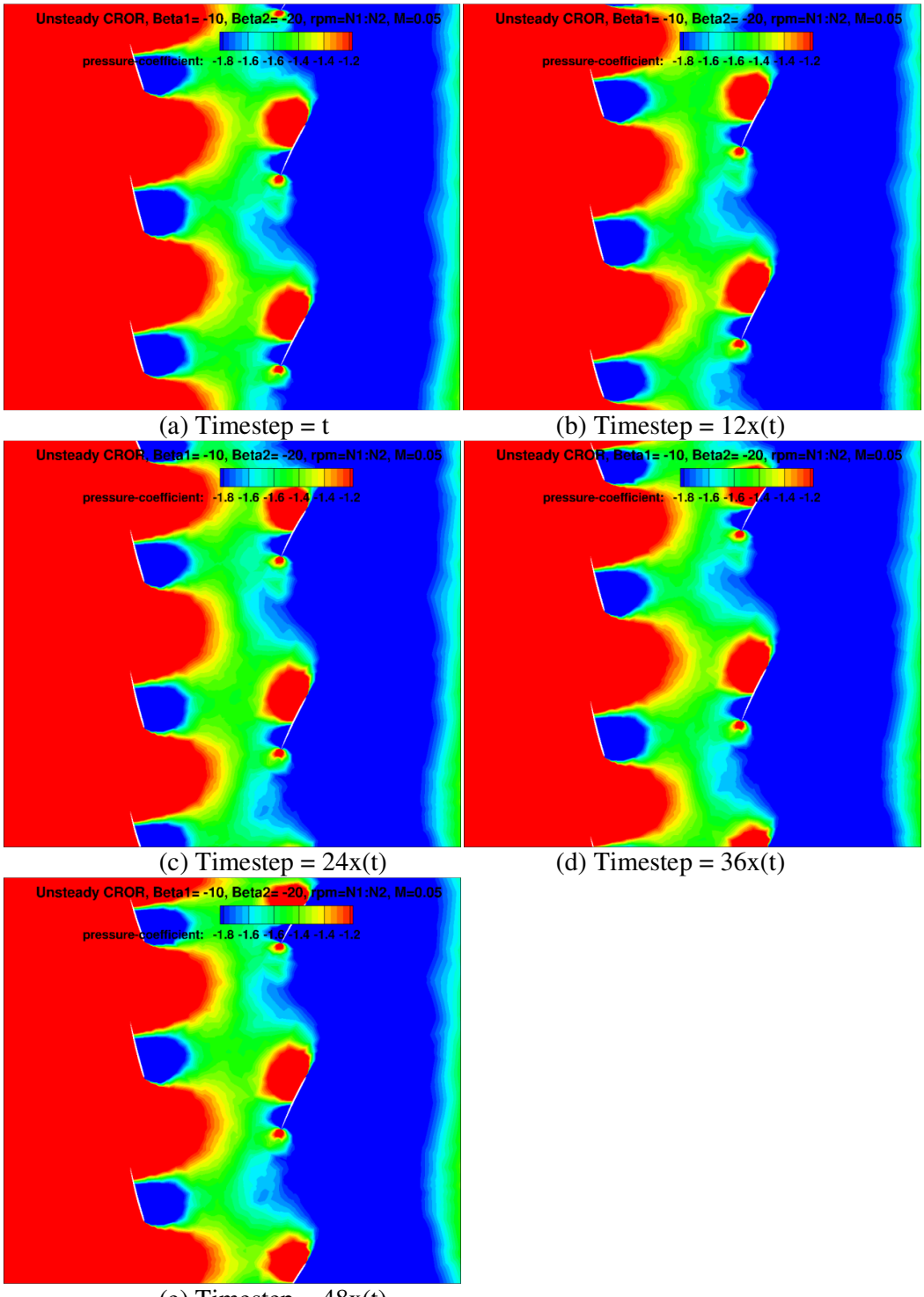

(a) Timestep = t

(b) Timestep = 12x(t)

(c) Timestep = 24x(t)

(d) Timestep = 36x(t)

(e) Timestep = 48x(t)

Figure 5-45 Circumferential contours of Cp at 70% front rotor bladespan taken at 5 varying phase positions.

5.3.4 Summary of findings

- The T and Q results showed poor agreement with experimental data despite good residual convergence and asymptotic convergence of the force and moment values towards constant values (after 1080 timesteps).

- The unsteady variation of T and Q with timestep is nominal. This has important consequences for the validity of the steady-state frozen rotor results.

- Contours of C_p and normalised axial velocity show similar features to frozen rotor contours for the same operating case. The major difference is highlighted as increased negative C_p in the region between the rotors.

- Circumferential C_p contours at varying phase positions provides further evidence that the unsteady interaction effects due to phase position are small.

Some possible reasons for the discrepancies in unsteady sliding mesh calculated T and Q values are provided below.

— The grid design used for the unsteady sliding mesh calculation was based on the hybrid grid from the frozen rotor methodology. Any poorly meshed regions in the grid design may have amplified adverse effects when the mesh sections changed phase positions.

— Apart from structured C-type mesh wraps around the front rotor blades, most of the domain was unstructured mesh. This may have had a negative impact when the interface, required for the sliding mesh technique, was created at the midpoint of the rotor spacing. Once the rotor meshes have rotated from their initial position, the entire grid becomes a non-conformal mesh (node locations on the interface surfaces are not identical). The grid design stage in the frozen rotor methodology did not account for this future requirement.

— Despite good residual and force/moment convergence, the timestep size used in this preliminary unsteady calculation may have been too large.

6 Conclusions and future work

This chapter presents some conclusions based on the analysis of the experimental results as well as the various CFD calculations. It also presents recommendations for future research activities to continue this overall investigation into thrust reverse aerodynamics of open rotors.

6.1 CFD prediction of rotor performance

By comparing the thrust and torque values from frozen rotor steady-state modelling of Contra-Rotating Open Rotors to the experimental data provided, it is shown that possible future prediction tools for reverse thrust operations could be developed from improved CFD models. Prior to this research there were no previous numerical investigations of this CROR flow regime available in the public domain. After establishing a methodology with single rotor reverse thrust modelling, which has also not been subject to CFD research campaigns, contra-rotating rotors were modelled to produce comparable results. There are discrepancies in the simulated rotor performance parameters, however given the level and complexity of separated flow in this operating condition, this work has demonstrated that CFD can generate results of beneficial accuracy. Perhaps more relevant is that the CFD observed trends in T and Q show very good agreement with those in the experimental data. The effects of variation in operating parameters (rpm, Mach number, blade pitch) have been reproduced quite well by the CFD frozen rotor approach adopted in this work. Given that this research is an initial step into reverse thrust aerodynamics modelling, the accurate prediction of trends in performance behaviour is an encouraging find.

6.2 Origin and impact of flowfield recirculation

From the CFD results in this work it appears that the main flowfield feature of CROR reverse thrust operation is a large area of recirculation downstream of the blade rows. Based on the two pitch combination settings modelled ($\beta_{1,2}$ =+30˚,-10˚ and $\beta_{1,2}$ =-10˚,-20˚) it appears that the negative pitch blade row to first experience conventional approaching flow generates this recirculation feature in the flowfield. CFD contour plots at various positions in the flowfield show that a large downstream area of relative

pressure drop is being created by the lower blade (suction) surfaces of the negative pitch rotor blades. The flow around this low relative pressure area is subject to Coriolis effect and large recirculation occurs as a result. It should be remembered at this point that the hub was modelled to continue infinitely downstream of the rotors as a simplification in the modelling. That may have affected the fidelity of this recirculating flow however, in spite of this, CFD results have still highlighted a feature requiring further attention. The extent of downstream recirculation can be measured by using axial velocity of 0 m/s as an indicator on the hub surface downstream of the blade rows. *Table 6-1* contains all the distances of reverse flow measured on the hub surface for each case simulated. The axial distances are taken from the centre point of the aft rotor to the point of V_{axial} = 0m/s on the hub surface downstream. Circumferential variation of this distance was seen to be small and assumed negligible.

Pitch Setting	**RPM**	**Mach No.**	**Downstream extent of reverse flow /L_1**
β_1=+30˚, β_2=-10˚	**N1:N2**	0.05	3.4
		0.1	3.9
		0.15	4.2
		0.2	4.3
	N1:2(N2)	0.05	3.8
		0.1	3.7
		0.15	3.9
		0.2	4.0
	2(N1):N2	0.1	3.5
		0.15	3.7
		0.2	3.9
	2(N1):2(N2)	0.1	3.6
		0.15	3.8
		0.2	4.1
β_1=-10˚, β_2=-20˚	**N1:N2**	0.05	4.8
		0.1	4.8
		0.15	5.1
		0.2	5.1
	N1:2(N2)	0.05	4.4
		0.1	4.6
		0.15	4.8
		0.2	4.9

Table 6-1 Downstream extent of reverse flow measured by Vaxial=0m/s on hub surface.

The distances are given in terms of front rotor blade length L_1, to keep consistency with CFD domain measurements. The purpose of this table is to illustrate the large probability of recirculating hot exhaust gas from the CROR core generator, since the open rotor design under investigation is a pusher layout with the blade rows located at the aft of the gas turbine engine core. This must be accounted for in future structural integrity studies of the blade and engine nacelle surfaces as well as any wing or fuselage panels (depending on engine location) that may fall into the range of the recirculation region. There is no evidence in the results that reverse flow may pose a risk to the engine core from re-ingestion, at Mach number range of 0.05 – 0.2. When both rotors are at negative pitch, reverse flow is seen to propagate upstream through the front rotor. However, further high-fidelity modelling would only be required to assess the potential risk if the engine design was puller style and the core intake was located near the front blade row.

6.3 Negative torque and overspeed

The issue of shaft overspeed is a critical factor in determining the operational settings for open rotors. Front and aft blade rows are required to generate a minimum amount of positive torque to absorb the minimum amount of engine power, and hence avoid overspeed. It is even more critical for reverse thrust operational settings since it is an off-design condition. Results in Chapter 5 show the generation of negative torque arises from a small number of cases investigated in this work. Typically this would indicate a significant change in operating parameters is required to avoid negative torque. It is possible to adjust rpm and/or blade pitch for Mach number values so that overspeed risk is eliminated. This negative torque avoidance may be a greater factor, in arriving at finalised rotor operation settings, than magnitude of negative thrust production. However, there is an inherent risk with reverse thrust operation, whereby any rotor that changes pitch from a positive to negative value, in order to generate reverse thrust, must cross through the range of pitch values that lead to negative torque and overspeed. Introduction of a gearbox into the CROR design (like that used in the PW-Allison 578DX propfan [22]) may also have an influence on the rationale of final reverse thrust settings. Differential planetary gearboxes for a 3-shaft system are most commonly used in the following way:

1-input (engine) **: 2-outputs** (2 rotors)

The impact of negative torque on this gearbox system may be different to that on a direct drive CROR design (GE36 UDF propfan). What is clear is that overspeed avoidance will be a major contributor to the reverse thrust setting decision process for rotor speed and blade pitch at a particular aircraft velocity.

6.4 CFD unsteady sliding-mesh calculation

The unsteady sliding mesh calculation showed that it is possible to develop a 3D unsteady calculation of CROR in reverse thrust operation. However, the calculation yielded thrust and torque results of poor agreement with experimental values. The possible reasons for this error have been stated in the previous chapter. There is an important observation made from the unsteady performance and flowfield results that is beneficial to this research. The unsteady rotor interaction effects due to phase position appear to be quite small. This greatly increases the validity of using the simplified frozen rotor CFD approach for CROR reverse thrust investigations, since the acknowledged weakness of this method, in typical turbomachinery multistage analysis, is the heavy dependence of performance on the relative position the blade rows are fixed in. The benefit of the frozen rotor approach when compared to the unsteady sliding mesh technique is that demand on computational resources is greatly reduced and time penalties are decreased. During this research the typical running time for a frozen rotor case was 5-7 days on 16 processors of a parallel processing system. When compared to the unsteady case which took 6 weeks to perform 1080 timesteps, the benefits are clear.

6.5 Future work

As this research has taken the first investigative step into reverse thrust aerodynamics of open rotors, the methodology developed was primarily to explore the possibility of using CFD to predict reverse thrust performance. Since that has been accomplished, the immediate next step for future work can focus on improving the fidelity of the numerical calculations in the following areas:

- Domain and meshing – with initial knowledge of the resulting flowfield an improved grid design can be developed in a more refined domain.

- Turbulence modelling – there was no turbulence model study conducted in this work. Other models may yield better accuracy in dealing with the high level of separation. This could improve the accuracy of blade drag prediction when combined with greater mesh resolution around the blade areas to reduce numerical diffusion.

- Solver settings – a pressure-based solver was used for the entirety of this CFD work. While justifications were made for using this, a density-based solver may better account for compressibility effects near the blade tips.

Once demonstrated improvements to the numerical calculations have been made it should then be possible to explore different operation settings to those in the experimental data. Different pitch angle combinations as well as variation of front and aft rotor rpm to more than two levels can be investigated.

Another unsteady sliding mesh calculation(s) should be completed to try and improve the accuracy of the rotor performance prediction. Refinements to the grid design as well as improvements to the methodology are based on similar suggestions for frozen rotor simulations. It is vital to provide further evidence that the unsteady rotor interactions effects due to phase position are small. This would justify a future CFD campaign, of much wider investigative scope, being completely based on the frozen rotor approach used here.

7 References

1. http://www.rolls-royce.com/deutschland/de/about/innovationen/ (accessed Jan-2011)

2. http://www.icao.int/icao/en/env/aee.htm (accessed Jan-2011)

3. http://www.iata.org/whatwedo/economics/fuel_monitor3/ (accessed Jan-2011)

4. Davidson, R.E., 1981, *Optimization and performance calculation of dual-rotation propellers*, NASA TP-1948.

5. Nelson, Wilbur Clifton, 1913, *Airplane propeller principles*, J. Wiley & Sons.

6. Lan, C.E., Roskam, J., 1981, *Airplane aerodynamics and performance*, Roskam Aviation and Engineering.

7. Houghton, E. L., 2003, *Aerodynamics for engineering students 5th Ed*, Butterworth-Heinemann.

8. Gray, W.H., Bierman, D, 1942, *Wind-tunnel tests of single- and dual-rotating pusher propellers having from three to eight blades*, NACA WR-L-359.

9. http://www.flightglobal.com/blogs/aircraft-pictures/2008/06/douglas-xa2d1-skyshark.html (accessed Feb-2011)

10. http://www.zonamilitar.com.ar/foros/sistemas-de-armas-aereos-en-servicio/26056-el-club-de-los-bombarderos-de-posguerra-4.html (accessed Feb-2011)

11. http://www.janes.com/articles/Janes-Aero-Engines/Kuznetsov-NK-12-Russian-Federation.html (accessed Feb-2011)

12. http://www.aerospaceweb.org/aircraft/bomber/tu95 (accessed Feb-2011)

13. Strack, W.C., Knip, G, 1981, *Technology and benefits of aircraft contra rotation propellers*, NASA TM-82983

14. Hanson, D.B., 1985, *Noise of Counter-rotation Propellers*, Journal of Aircraft, Vol. 22 No.7, pp. 609-617.

15. Whitlow, J. B., Sievers, G. K.,1984, *Fuel savings potential of the NASA Advanced Turboprop Program*, NASA-TM-83736.

16. Mikkelson, D. C., Blaha, B. J., Mitchell, G. A., Wikete, J. E., 1977, *Design and performance of energy efficient propellers for Mach 0.8 cruise*, NASA-TM-X-73612

17. Leonard, J.M., 2007, *The Allison Engine Catalog 1925-2007*, Rolls-Royce Heritage Trust.

18. Graber, E.J., 1987, *Overview of NASA PTA propfan flight test program*, 88N-15805.

19. http://grcimagenet.grc.nasa.gov/share/searchbrowse_stillImage_action.CFM?maxcnumber=2712&maxcyear=1984&date=1984&max_hits=100&dis_opts=shoicons&TXTTITLE= (accessed Feb-2011)

20. Hoff, G.E., 1990, *Experimental performance and acoustic investigation of modern, counterrotating blade concepts*, NASA CR-185158.

21. Groeneweg, J, Bober, L, 1990, *Advanced propeller research*, 92N22537

22. Anderson, N.E., Cedoz, R.W., 1987, *Advacned gearbox technology*, NASA CR-179625.

23. http://www.janes.com/articles/Janes-Aero-Engines/Ivchenko-Progress-D-27-Ukraine.html (accessed Feb-2011)

24. http://en.aerosila.ru (accessed Feb-2011)

25. http://www.scienceforums.net/topic/33224-open-rotor-aircraft/page__p__428143__hl__propfan__fromsearch__1#entry428143 (accessed Feb-2011)

26. http://www.janes.com/articles/Janes-Aero-Engines/Kuznetsov-NK-93-Russian-Federation.html (accessed Feb-2011)

27. http://www.globalsecurity.org/military/world/russia/nk-engines.htm (accessed Feb-2011)

28. http://www.flightglobal.com/pdfarchive/view/1995/1995%20-%202253.html. (accessed Feb-2011)

29. http://www.airliners.net/photo/Gromov-Flight-Research/Ilyushin-Il-76LL/1298351/L/. (accessed Feb-2011)

30. Hartman, Edwin P.,1934, *Negative thrust and torque characteristics of an adjustable-pitch metal propeller*, NACA-TR-464

31. Hartman, Edwin P., Biermann, David, 1938, *The negative thrust and torque of several full-scale propellers and their application to various flight problems*, NACA-TR-641.

32. Douglass, William M.,1944, *An experimental investigation of the thrust and torque produced by propellers used as aerodynamic brakes*, NACA-ARR-4H26.

33. Gilman, Jean, 1945, *Characteristics of several single and dual-rotating propellers in negative thrust*, NACA-MR-L5C07.

34. Reynolds, R.M., Samonds, R.I., Walker, J.H., 1957, *An investigation of single- and dual-rotation propellers at positive and negative thrust, and in combination with an NACA 1-series D-type cowling at Mach numbers up to 0.84,* NACA-TR-1336.

35. Christopher, E, Gazzaniga, J, 1988, *A Summary of low-speed wind tunnel results of several high-speed counterrotation propeller configurations*, NASA-TM-100945.

36. Roosenboom, Eric W., Schroder, Andreas, 2010, *Flowfield Investigation at Propeller Thrust Reverse*, ASME Journal of Fluids Engineering, Vol 132.

37. Thakur, S, 2003, '*CFD Predictions of Turbomachinery Flows Using Quasi-Steady and Unsteady Models'*, AIAA 2003-4133.

38. Zachariadis, A, Hall, C.A., 2011, '*Application of a Navier-Stokes Solver to the Study of Open Rotor Aerodynamics'*, ASME Journal of Turbomachinery, Vol 133.

39. Deconinck, T, Hoffer, P.A., 2010, '*Prediction of Near- and Far-field Noise Generated by Contra-Rotating Open Rotors'*, AIAA 2010-3794.

40. Stuermer, Arne, 2008, '*Unsteady CFD Simulations of Contra-Rotating Propeller Propulsion Systems',* AIAA 2008-5218.

41. Keshtiban, I.J., Belblidia, F, 2004, '*Compressible Flow Solvers for Low Mach number Flows – a review'*, CSR2-2004 Computer Science Research Report, Swansea University.

42. Tu, J, Yeoh, G.H., 2008, '*Computational Fluid Dynamics – A Practical Approach'*, Butterworth-Heinemann.

43. P.J., Roache, 1998, '*Verification and validation in computational science and engineering*', Hermosa.

44. Ouboussad, S, 2009, *'Open Rotor Tip Vortex Aerodynamics'*, MSc Thesis, Cranfield University.

45. McCormick, B., 1995, *'Aerodynamics, Aeronautics and Flight Mechanics'*, John Wiley New York.

Appendix A

A.1 Froude's Simple Momentum Theory of Propulsion

There is a simple method of considering the operation of a propeller which is based on the work of Rankine and Froude and is called the Simple Momentum Theory. The propeller is assumed to have a large number of blades so that it effectively becomes a disc. This disc or actuator disc is infinitely thin and offers no resistance to the air passing through it. The air passing through the disc receives energy in the form of a step change in pressure, which is assumed to be uniform across the entire disc. The velocity of the air through the disc is assumed to be constant over the area of the disc. It is also assumed that there is no rotation imparted to the flow as it passes through the disc and that the Mach number of the flow is so low, the fluid behaves as an incompressible fluid. Finally it is assumed that the flow passing through the disc can be defined by a stream tube, given in *Figure A - 1*, and that no energy is transferred to the air outside this stream tube.

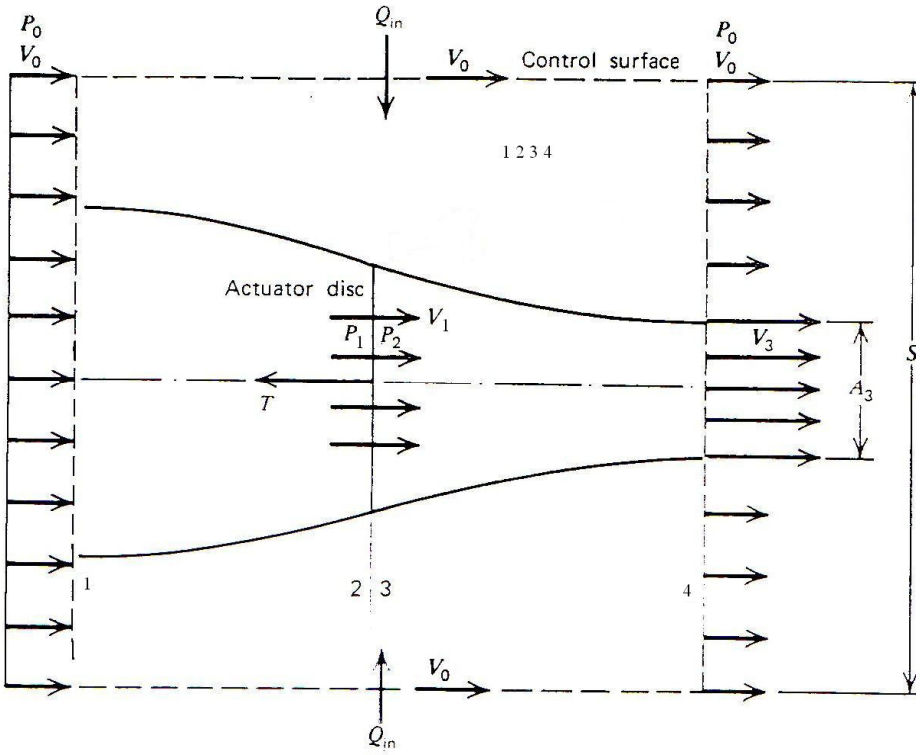

Figure A - 1 Idealised Flow for Simple Momentum Theory [45].

The air at the entry of the stream tube (station 1) is travelling at a velocity v_0 with a free stream static pressure p_0. As the air approaches the disc its velocity increases and pressure decreases right up to the disc (of cross-sectional area A) where, at this stage in the flow, it has a velocity v_1 and a pressure p_1. The disc then provides a step change in pressure, increasing it to p_2, however the velocity remains the same ($v_1 = v_2$). The air exiting the disc expands downstream and increases in velocity to v_3 where A_3 is the slipstream cross-sectional area, at which point the pressure has returned back to the free stream static pressure. The thrust felt by the disc is the increase in mass flow momentum out of the disc

$$T = \rho A_3 v_3 (v_3 - v_0) \tag{1}$$

The thrust can also be given as the pressure difference across the disc multiplied by the disc area A

$$T = A(p_2 - p_1) \tag{2}$$

p_1 and p_2 can be gotten in terms of velocity by applying Bernoulli's equations (as a result of initial assumptions made)

$$p_0 + \frac{1}{2}\rho v^2 = p_1 + \frac{1}{2}\rho v_1^2 \tag{3}$$

$$p_0 + \frac{1}{2}\rho v_3^2 = p_2 + \frac{1}{2}\rho v_2^2 \tag{4}$$

Now we can subtract p_2 from p_1 and remembering that $v_1 = v_2$ gives the following

$$p_2 - p_1 = \frac{1}{2}\rho(v_3^2 - v_0^2) \tag{5}$$

Taking continuity into account, i.e. $Av_1 = A_3 v_3$, and equating the previous thrust equations gives the well known relationship which basically states that the velocity through the disc is the average of the fully upstream and fully downstream flows.

$$v_1 = \frac{v_3 + v_0}{2} \tag{6}$$

We can introduce a term v_i representing the propeller induced velocity and write

$$v_1 = v_0 + v_i \tag{7}$$ and $$v_3 = v_0 + v_i \tag{8}$$

Then the thrust can be written as the following

$$T = 2\rho A(v_0 + v_i)v_i \tag{9}$$

The power the disc has supplied the flow with can be expressed as an increase in kinetic energy of the flow and can be written as

$$P = \frac{1}{2}\dot{m}({v_3}^2 - {v_0}^2) = 2\rho A(v_0 + v_i)^2 v_i \tag{10}$$

By combining eqn 9 and 10 we can arrive at a term describing the total power

$$P = T(v_0 + v_i) \tag{11}$$

This total power is seen as a combination of the useful power and induced power

$$P_{useful} = Tv_0 \tag{12}$$ and $$P_{induced} = Tv_i \tag{13}$$

The Ideal Efficiency (η_i) of the disc, sometimes called the Froude Efficiency, is defined as the ratio of useful work to total work and is expressed below

$$\eta_i = \frac{UsefulPower}{TotalPower} = \frac{Tv_0}{T(v_0 + v_i)} = \frac{1}{1 + v_i / v_0} \tag{14}$$

This ideal efficiency will never be reached however, due to all the assumptions made at the start of the momentum theory. It does give a useful approximation as to what can be anticipated from a propeller. The actual efficiency is estimated by various sources to be in the range of 80% - 90% of the ideal efficiency.

A.2 Blade-Element Theory (BET)

Blade-Element Theory is a simple method of predicting propeller performance. It involves splitting the propeller blade into an infinite number of sections, or elements, and investigating the forces acting on each element. A blade element can be defined as having a thickness dr, at a distance r from the axis of rotation, as seen in *Figure A - 2*

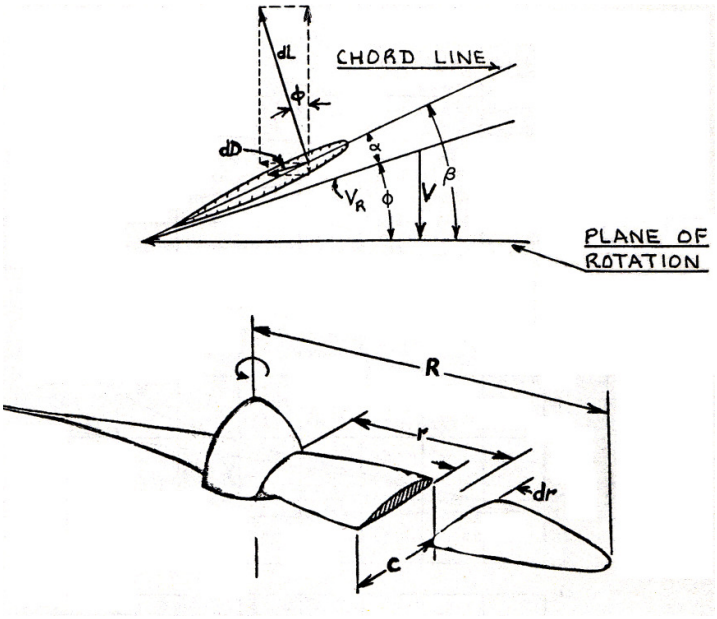

Figure A - 2 Propeller Blade Element Geometry [6].

On examining the element in ***Figure A - 2***, we can see the thrust is made up of the components of lift and drag perpendicular to the plane of rotation. If the element has a chord length c, then the elemental thrust dT can be expressed as:

$$dT = dLCos\phi - dDSin\phi$$

$$= \frac{1}{2}\rho V_R{}^2 c.dr(C_L Cos\phi - C_D Sin\phi) \tag{15}$$

Similarly the elemental torque, dQ, is made up of the components of lift and drag in the plane of rotation multiplied by their moment arm (r) to the centre of rotation

$$dQ = dLSin\phi + dDCos\phi$$

$$= \frac{1}{2}\rho V_R{}^2 cr.dr(C_L Sin\phi + C_D Cos\phi) \tag{16}$$

Remembering the propeller efficiency definition from earlier where

$$\eta_{prop} = \frac{UsefulPower}{TotalPower} = \frac{TV}{2\pi nQ} = \frac{TV}{\Omega Q} \tag{17}$$

Now this expression can be used to give the blade-element efficiency

$$\eta_{element} = \frac{VdT}{\Omega dQ} = \frac{V}{\Omega r}\frac{C_L Cos\phi - C_D Sin\phi}{C_L Sin\phi + C_D Cos\phi} \tag{18}$$

$$\eta_{element} = Tan\phi\frac{C_L Cos\phi - C_D Sin\phi}{C_L Sin\phi + C_D Cos\phi} \tag{19}$$

Now that we have the thrust and torque provided by the element, we can integrate those equations (15 and 16) over the entire length of the blade and get the total thrust and torque provided by the blade. This can only be done however, when the elemental aerodynamic characteristics are accurately known. They cannot be accurately known because the induced velocity due to lift production has been neglected. This leads us to the combined Blade-Element Momentum Theory which actually calculates the induced velocity.

A.3 Combined Blade-Element Momentum Theory

Looking back at the Momentum Theory, the thrust of the disc was expressed in terms of the induced velocity

$$T = 2\rho A(v_0 + v_i)v_i$$

Figure A - 3 now shows the induced velocity along with the components of lift and drag acting on an element. It should be noted that α is the previous angle of attack from *Figure A - 2* and α_0 represents the new angle of attack after induced velocity is included.

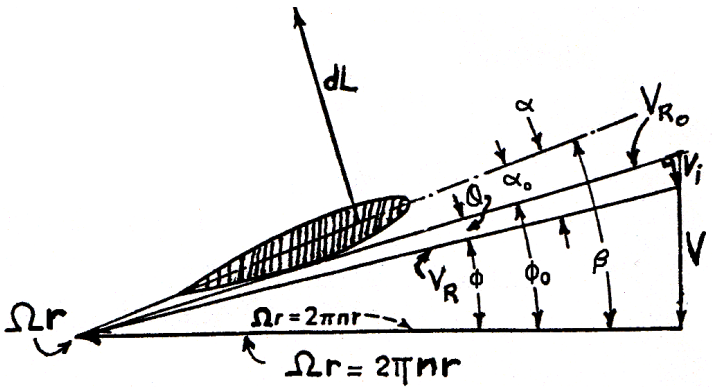

Figure A - 3 Forces on blade element including induced velocity Vi [6]

With this term we can now say that the component of V_i in the thrust direction is $V_i Cos\phi_0$. The number of blades on the propeller is given by the term B, and with this we can express the total elemental thrust, by Momentum Theory, as

$$BdT = 2\rho.2\pi r.dr(V + V_i Cos\phi_0)(V_i Cos\phi_0) \tag{20}$$

From Blade Element Theory (and assuming the D/L ratio is small that we can omit the C_D term):

$$BdT = BdLCos\phi_0 = BC_L \frac{1}{2} \rho V_{R0}{}^2 cr.dr.Cos\phi \tag{21}$$

By equating the two previous expressions we can say:

$$V_i = \frac{BC_L c V_{R0}{}^2}{8\pi r(V + V_i Cos\phi_0)} \tag{22}$$

We can simplify this by assuming that the angle θ is small according to *Figure A - 3*. Therefore

$$Sin\phi_0 = Sin(\phi + \theta) \cong Sin\phi + \theta Cos\phi \tag{23}$$

$$= \frac{V + V_i Cos\phi_0}{V_{R0}} \tag{24}$$

$$\text{Also} \quad Tan\theta = V_i / V_{R0} \cong \theta \tag{25}$$

$$\text{And} \quad C_l = a_0(\beta - \theta - \phi) \tag{26}$$

where a_0 is the lift-curve slope for the airfoil section. With the eqns 24 – 26, equation 22 can be written as :

$$\theta \cong \frac{Bc}{8\pi r} \frac{a_0(\beta - \phi - \theta)}{Sin\phi + \theta Cos\phi} \tag{27}$$

Solidity Ratio σ is defined as the ratio of total blade area to the disk area and can be expressed as the following:

$$\sigma = \frac{BcR}{\pi R^2} = \frac{Bc}{\pi R} \tag{28}$$

And the non-dimensional blade station as: $x = r / R$

Eqn 27 can now be represented as the equivalent quadratic equation in θ:

$$\theta^2 Cos\phi + (Sin\phi + \frac{a_0\sigma}{8x})\theta - \frac{a_0\sigma}{8x}(\beta - \theta) = 0$$

With the solution:

$$\theta = \frac{1}{2Cos\phi}\{-(Sin\phi + \frac{a_0\sigma}{8x}) + \sqrt{(Sin\phi + \frac{a_0\sigma}{8x})^2 + 4Cos\phi\frac{a_0\sigma}{8x}(\beta - \phi)}\} \tag{29}$$

If the following approximations are used: $Cos\phi \approx 1.0$, $Sin\theta \approx V/V_t x$ and

$V_R \approx V_t x$ where V_t is the tip speed, then the induced velocity $(V_i \cong \theta V_t x)$ can be found from eqn 29 to be

$$V_i = V_t\{-(\frac{V}{2V_t} + \frac{a_0\sigma}{16}) + \sqrt{(\frac{V}{2V_t} + \frac{a_0\sigma}{16})^2 + \frac{a_0\sigma\beta x}{8} - \frac{a_0\sigma V}{8V_t}}\ \} \tag{30}$$

According to [6] eqn 30 is used frequently to evaluate the induced velocity on helicopter rotors in vertical climbing flight. It should be noted that under low thrust conditions eqn 27 can be solved by neglecting the θ^2 term to give:

$$\theta \cong \frac{\beta - \phi}{1 + \frac{8xSin\phi}{a_0\sigma}} \tag{31}$$

If n is the rotational speed in revolutions per second, then:

$$V_{R0} = V_R Cos\theta = \frac{2\pi nr}{Cos\phi}Cos\theta \tag{32}$$

Now that we have an expression for the new relative velocity V_{R0} that includes the induced velocity terms, we can substitute this expression into the equations for elemental thrust and torque defined in the previous Blade Element Theory (BET) section which yields the following:

$$dT = B\frac{1}{2}\rho {V_{R0}}^2 c.dr(C_L Cos\phi_0 - C_D Sin\phi_0) \tag{33}$$

$$dT = B\rho(\frac{2\pi^2 n^2 r^2}{Cos^2\phi}Cos^2\theta)c.dr(C_L Cos\phi_0 - C_D Sin\phi_0) \quad (34)$$

and

$$dQ = B\frac{1}{2}\rho {V_{R0}}^2 cr.dr(C_L Sin\phi_0 + C_D Cos\phi_0) \quad (35)$$

$$dQ = B\rho(\frac{2\pi^2 n^2 r^2}{Cos^2\phi}Cos^2\theta)c.dr(C_L Sin\phi_0 + C_D Cos\phi_0) \quad (36)$$

With the propeller thrust and torque coefficients already defined in the previous section we can now advance these expressions to workable equations that will yield values for various sections of the propeller blades:

$$C_T = \frac{T}{\rho n^2 D^4} \quad (37) \quad \text{and} \quad C_Q = \frac{Q}{\rho n^2 D^5} \quad (38)$$

Equations 34 and 36 can be expressed as:

$$\frac{dC_T}{dx} = 3.88x^2\sigma\lambda_T \quad (39) \quad \text{and} \quad \frac{dC_Q}{dx} = 1.94x^3\sigma\lambda_Q \quad (40)$$

Where

$$\lambda_T = \frac{Cos^2\theta}{Cos^2\phi}(C_L Cos\phi_0 - C_D Sin\phi_0) \quad (41)$$

$$\lambda_Q = \frac{Cos^2\theta}{Cos^2\phi}(C_L Sin\phi_0 + C_D Cos\phi_0) \quad (42)$$

By integrating equations 37 and 38 over the entire length of the blade, the coefficients of thrust and torque can be estimated. In the design of a blade this is the usual first step for a conventional propeller [7].

A.4 Reverse thrust prediction

There is a method, for conventional propellers, of approximately predicting the reverse thrust using performance charts for positive thrust [6]. If we start off by applying the continuity equation to stations 3 and 4 of the idealised streamtube in *Figure A - 1*, and use eqns 1 and 2 we arrive at the term:

$$A(v + v_i) = A_3(v + 2v_i) \tag{43}$$

This term can also be expressed, using R for the propeller radius and R_3 for the radius of slipstream area:

$$\frac{R_3}{R} = \sqrt{(1 + \frac{v}{v_i}) / (2 + \frac{v}{v_i})} \tag{44}$$

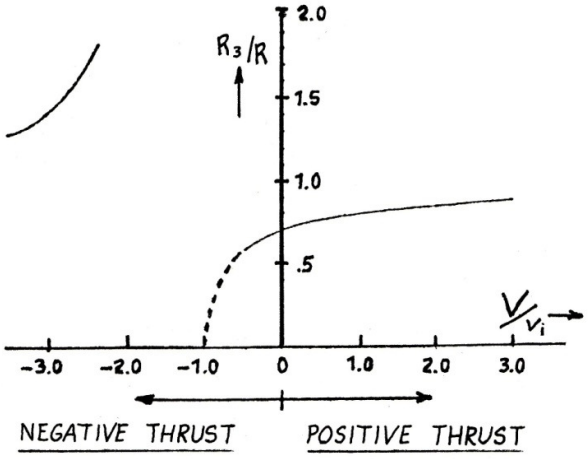

Figure A - 4 Ratio of far wake radius to propeller disk versus ratio of wind to induced velocities [6].

Figure A - 4 shows $\frac{R_3}{R}$ plotted against $\frac{V}{V_i}$. It shows that under static conditions $\frac{R_3}{R} = \sqrt{2}/2$. As $\frac{V}{V_i}$ becomes negative and approaches -1, $\frac{R_3}{R}$ decreases and approaches 0. In

this case the mass flow rate becomes 0 and the concept of simple momentum theory becomes meaningless

For $-2 < \frac{V}{V_i} < -1$, $\frac{R_3}{R}$ is imaginary.

For $-1 < \frac{V}{V_i} < 0$, the flow can be visualized by the streamlines in ***Figure A - 5***.

The thrust can be obtained from equation 45

$$-T = -\rho A(-V + V_i)V_i + \sigma A(-V + V_i)[-(-V + 2V_i)] \tag{45}$$

Which reduces to

$$T = 2\rho A(-V + V_i)V_i \tag{46}$$

An expression can be given for induced velocity

$$V_i = \frac{V}{2} + \sqrt{(\frac{V}{2})^2 + \frac{T}{2\sigma A}} \tag{47}$$

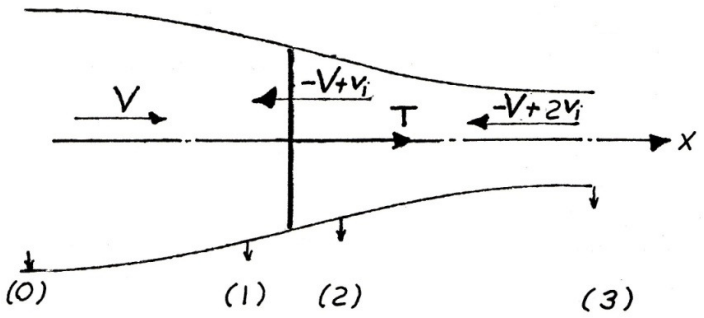

Figure A - 5 Streamtube for negative thrust at low speeds [6].

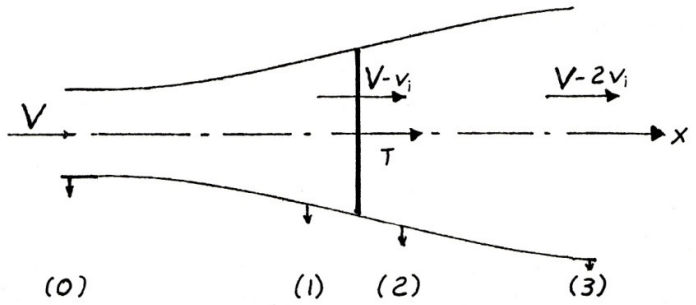

Figure A - 6 Streamtube for negative thrust at high speeds [6].

For $\frac{V}{V_i}$<-2, the flow can be visualised by the streamlines in ***Figure A - 6***. This negative thrust could be representative of a high speed dive and again can be represented by eqn 45

$$-T = -\rho A(V - V_i)V_i + \sigma A(V - V_i)(V - 2V_i)$$

or

$$T = 2\rho A(V - V_i)V_i \tag{48}$$

It follows that the induced velocity can be given by:

$$V_i = \frac{V}{2} - \sqrt{(\frac{V}{2})^2 - \frac{T}{2\sigma A}} \tag{49}$$

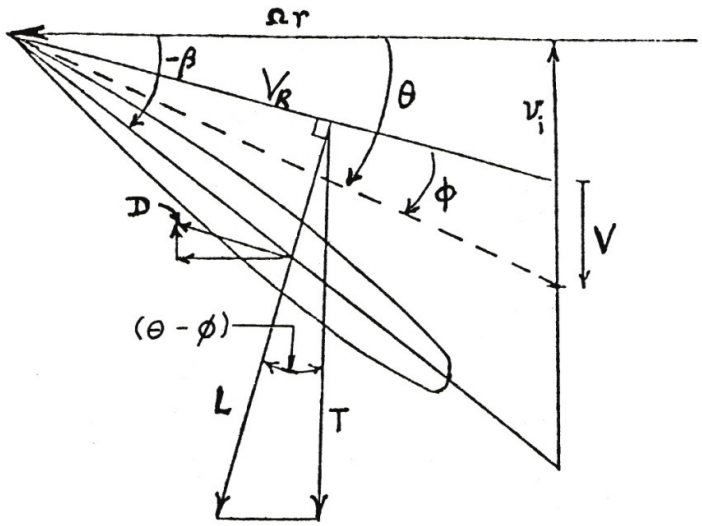

Figure A - 7 Forces on blade element at negative pitch with induced velocity larger than wind velocity [6].

Figure A - 7 shows the forces acting on a blade element producing negative thrust. From this figure and eqn 26 the angle of attack the airfoil experiences can be written as $\alpha = -\beta + \theta - \phi - \alpha_{zero-lift}$ where $\alpha_{zero-lift}$ is the zero lift angle. It follows that the sectional lift coefficient is

$$C_l = -a_0(\beta - (\theta - \phi) + \alpha_{zero-lift}) \tag{50}$$

Looking at ***Figure A - 7*** we can deduce that

$$\theta - \phi \approx Tan(\theta - \phi) = \frac{(V_i - V)}{\Omega r} = \frac{1}{\Omega r}\left[\frac{V}{2} + \sqrt{(\frac{V}{2})^2 + \frac{T}{2\sigma A}} - V\right] \tag{51}$$

Again from Simple Momentum Theory equation 45 can be expressed as a term for the positive thrust induced velocity

$$V_{i-positive} = -\frac{V}{2} + \sqrt{(\frac{V}{2})^2 + \frac{T}{2\sigma A}} \tag{52}$$

Which when substituted into eqn 51 yields

$$\theta - \phi \approx \frac{V_{i-positive}}{\Omega r} = Tan\theta_{positive} \approx \theta_{positive} \tag{53}$$

Now we can incorporate eqn 53 into eqn 50 and the result is:

$$C_l = -a_0(\beta - \theta_{positive} + \alpha_{zero-lift}) \tag{54}$$

This term can be altered to appear in the same format as eqn 26

$$C_l = -a_0((\beta + 2\alpha_{zero-lift}) - \theta_{positive} - \alpha_{zero-lift}) \tag{55}$$

Equation 28 shows that negative thrust can be calculated approximately by charts for positive thrust at an equivalent blade angle of $(\beta + 2\alpha_{zero-lift})$. For this method to be applicable for reverse thrust operation, the negative blade angle to absorb the rated engine power for braking operation must be known. If it is not known it may be assumed to be the blade angle for producing forward thrust at the same engine power.

A.5 Grid Convergence Studies

The improved design of the single front rotor grid at β = -10˚ (figure 3-1 grid (b)) was taken as the base grid for the grid convergence study of single rotor calculations. A datum case of rpm = N1 and mach number (M) = 0.1 was chosen for the study. For the contra-rotation grid convergence study, the grid for pitch-combination 1 (β_1 = +30˚, β_2 = -10˚) was chosen as the base grid with the datum case of rpm = N1 and N2 with M = 0.1. For both studies the base grid (or medium grid) was increased in cell count to produce a fine grid and also reduced in cell count to generate a coarse grid. For following equations taken from [43], terms relating to the fine, medium and coarse grids are given the underscores 1, 2 and 3 respectively. When refining or coarsening a grid for these types of studies it is desirable to do so in a systematic way to aid in accuracy of discretisation error. It ensures that all parts of the grid are refined or coarsened to the same ratio of nodal spacing (r). This is more difficult however to achieve in unstructured or hybrid grids. So instead an effective refinement ratio (r_{eff}) is defined in eqn 56 using the total number of cells (N).

$$r_{eff} = \left(\frac{N_1}{N_2} \right)^{1/D} \tag{56}$$

Where D is the dimensionality of the calculation.

Efforts were made by the author to keep the level of refinement as constant as possible throughout the entire domain by approaching target cell counts for the individual domain blocks through trial and error, and also to try and keep the same relative cell density within the areas of each block.

The observed order of convergence (p_{con}) was calculated from eqn 57. Since the accuracy of the special discretisation in the CFD solver was wet to 2nd order, a value of p_{com}=2 was used where the observed order of accuracy exceeded 2 or was negative.

$$p_{convergence} = \ln\left(\frac{f_3 - f_2}{f_2 - f_1} \right) / \ln r \tag{57}$$

Where f is the solution of interest

The solutions used for this study were thrust (T) and torque (Q) normalised with datum values. The Grid Convergence Index (GCI) for two grids is defined in eqn 58 where Fs is a factor of safety (taken as 1.25 since three grid levels were used [43]) and ε is the solution fractional difference, defined in eqn 59

$$GCI = F_s \frac{|\varepsilon|}{r^p - 1} \tag{58}$$

$$\varepsilon = \frac{f_2 - f_1}{f_1} \tag{59}$$

These GCI values were used to judge whether the grid solutions lay within the asymptotic range (AR). This is confirmed if eqn 60 is satisfied. It should be noted as this point that the values of a particular solution for each of the grids must be monotonic for the use of Grid Convergence Index theory as a means of assessing how dependent the solution is on grid size [43].

$$AR \cong \frac{GCI_{2-3}}{r^{p_{con}} GCI_{1-2}} \cong 1 \tag{60}$$

The grid cell counts and results from the single rotor grid convergence study are presented in Table A-1 and A-2 respectively. For the CROR frozen rotor convergence study, Table A-3 presents the grid cell counts, Table A-4 presents the results from the 3 grids used. Table A-5 shows the GCIs if the coarse grid results were disregarded due to error and the experimental results introduced.

Grid No.	Description	Total Cell Count
1	**Fine**	**8,036,215**
2	**Medium**	**4,048,887**
3	**Coarse**	**2,034,931**

Table A-1 Cell count of single rotor grid convergence study.

	Fine 1	Medium 2	Coarse 3	r_{eff}	p_{con}	ε_{1-2}	ε_{2-3}	GCI_{1-2}	GCI_{2-3}	AR
T/T_{datum}	-0.3759	-0.3318	-0.3889	1.257	x	0.147	-0.133	x	x	x
Q/Q_{datum}	0.4942	0.4358	0.5084	1.258	x	0.143	-0.134	x	x	x

Table A-2 Results of single rotor grid convergence study.

Grid No.	Description	Total Cell Count
1	**Fine**	**13,976,508**
2	**Medium**	**11,647,090**
3	**Coarse**	**9,705,909**

Table A-3 Cell count of CROR frozen rotor grid convergence study.

	Fine 1	Medium 2	Coarse 3	r_{eff}	p_{con}	ε_{1-2}	ε_{2-3}	GCI_{1-2}	GCI_{2-3}	AR
Front T/T_{datum}	0.1280	0.1192	0.1248	1.063	x	0.046	-0.074	x	x	x
Q/Q_{datum}	-0.4458	-0.4177	-0.4354	1.063	x	0.041	-0.067	x	x	x
Aft T/T_{datum}	-0.2764	-0.2724	-0.2779	1.063	x	0.020	-0.015	x	x	x
Q/Q_{datum}	0.2907	0.2860	0.2935	1.063	x	0.026	-0.017	x	x	x

Table A-4 Cell count of single rotor grid convergence study.

	Exp 0	Fine 1	Medium 2	r_{eff}	p_{con}	ε_{0-1}	ε_{1-2}	GCI_{0-1}	GCI_{1-2}	AR
Front T/T_{datum}	0.1434	0.1280	0.1192	1.063	2.000	-0.074	-0.120	0.719	1.162	0.548
Q/Q_{datum}	-0.3440	-0.4458	-0.4177	1.063	x	-0.067	0.228	x	x	x
Aft T/T_{datum}	-0.2569	-0.2764	-0.2724	1.063	x	-0.015	0.071	x	x	x
Q/Q_{datum}	0.1711	0.2860	0.2935	1.063	2.000	0.026	0.402	0.247	3.885	0.056

Table A-5 Cell count of single rotor grid convergence study.

A.6 Thrust and torque blade distribution

The sectional blade loading was obtained (from frozen rotor simulations) by calculating the pressure force at various spanwise sections of each rotor blade. The viscous forces were deemed negligible for these blade loading results because for the majority of cases, the magnitude of the viscous force was less than 1% of the total thrust force. Airfoil slices were taken at 18 spanwise positions, around which the C_p distribution was attained (see Figure A – 8).

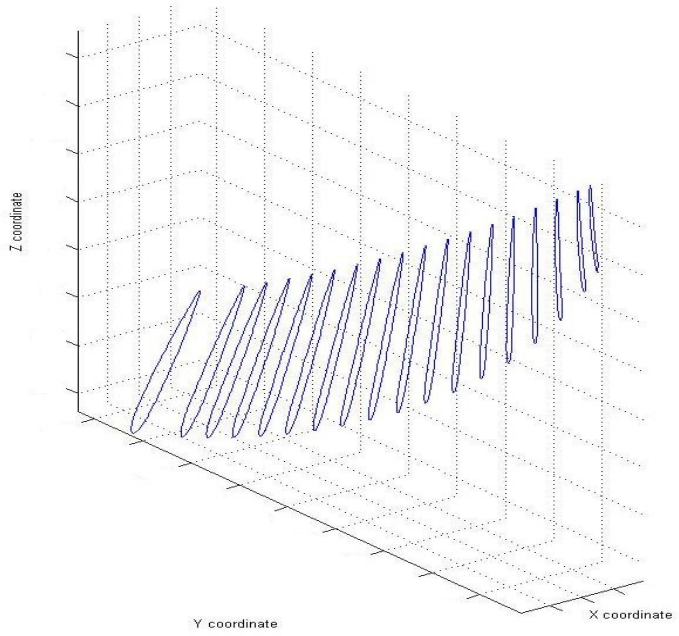

Figure A - 8 Airfoil slices taken from a blade.

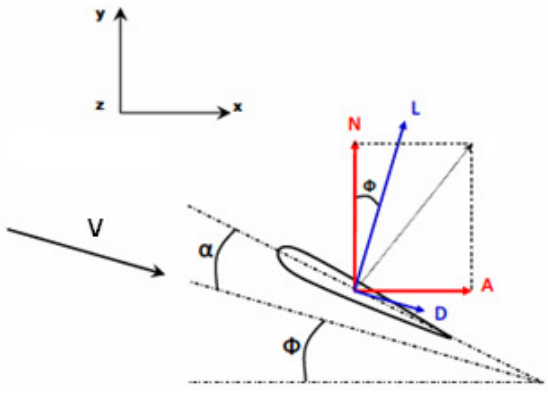

Figure A - 9 Normal and axial forces acting on a blade element [44].

For each slice, or blade element, the normal (C_N) and axial (C_A) components of pressure force coefficient are calculated per unit span of the blade element. This is done by splitting the airfoil into upper/lower and forward/backward surfaces respectively. Using the coordinate system in Figure A – 9, forward and backward surfaces are those 2 coordinate sets bound by the maximum and minimum y-coordinate values (Figure A – 10(a)). The upper and lower surfaces can defined as the 2 coordinate sets between the maximum and minimum x-coordinate values (Figure A – 1(b)).

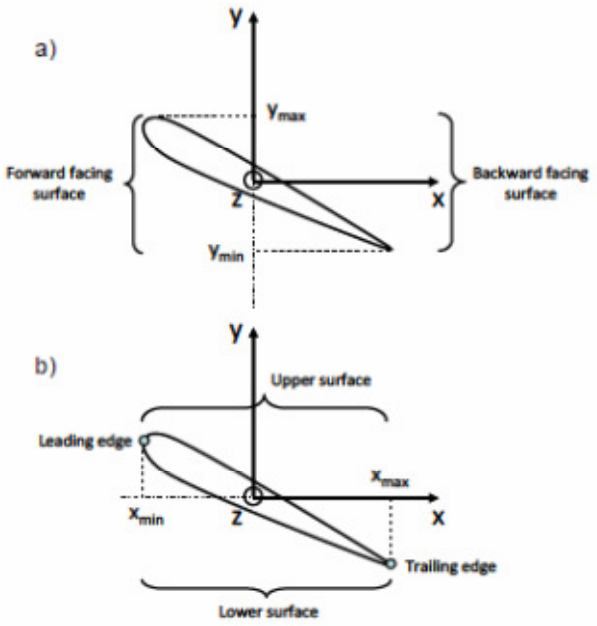

Figure A - 10 Determination of upper, lower, forward and backward facing surfaces[44].

Now integration of C_p around the upper and lower surfaces for C_N, and around the forward and backward surfaces for C_A, can be done for each airfoil using the equations from [44] defined below:

$$C_N = \frac{N}{qc} = \int_{x_{\min}}^{x_{\max}} (C_{pl} - C_{pu})dx \tag{61}$$

$$C_A = \frac{A}{qc} = \int_{y_{\min}}^{y_{\max}} (C_{pf} - C_{pb})dy \tag{62}$$

C_{pl} and C_{pu} are the pressure coefficients on the lower and upper surface respectively, with C_{pf} and C_{pb} relating to the forward and backward facing surfaces respectively, c is airfoil chord and q is the freestream dynamic pressure. Note: if an airfoil is taken as a slice of constant radial coordinate (r) then radius multiplied by angular coordinate (θ) will be used instead of x-coordinate and C_N integration equation will change accordingly.

Once the force coefficients per unit span are attained for the 18 various airfoil slices, the thrust and torque of each blade section can be calculated by respectively multiplying C_N and C_A by both the span of that section and the dynamic pressure. The result shows the distribution of forces and moments along the blade. These 18 sectional thrust and torque values can be summed to get the total blade force and moment (assuming that the pressure distribution is unchanged along the span of each blade section).